Universitat Autònoma de Barcelona

Inhibiting Myc and the Myc dependent inflammatory response as cancer therapies

Daniel Massó Vallés

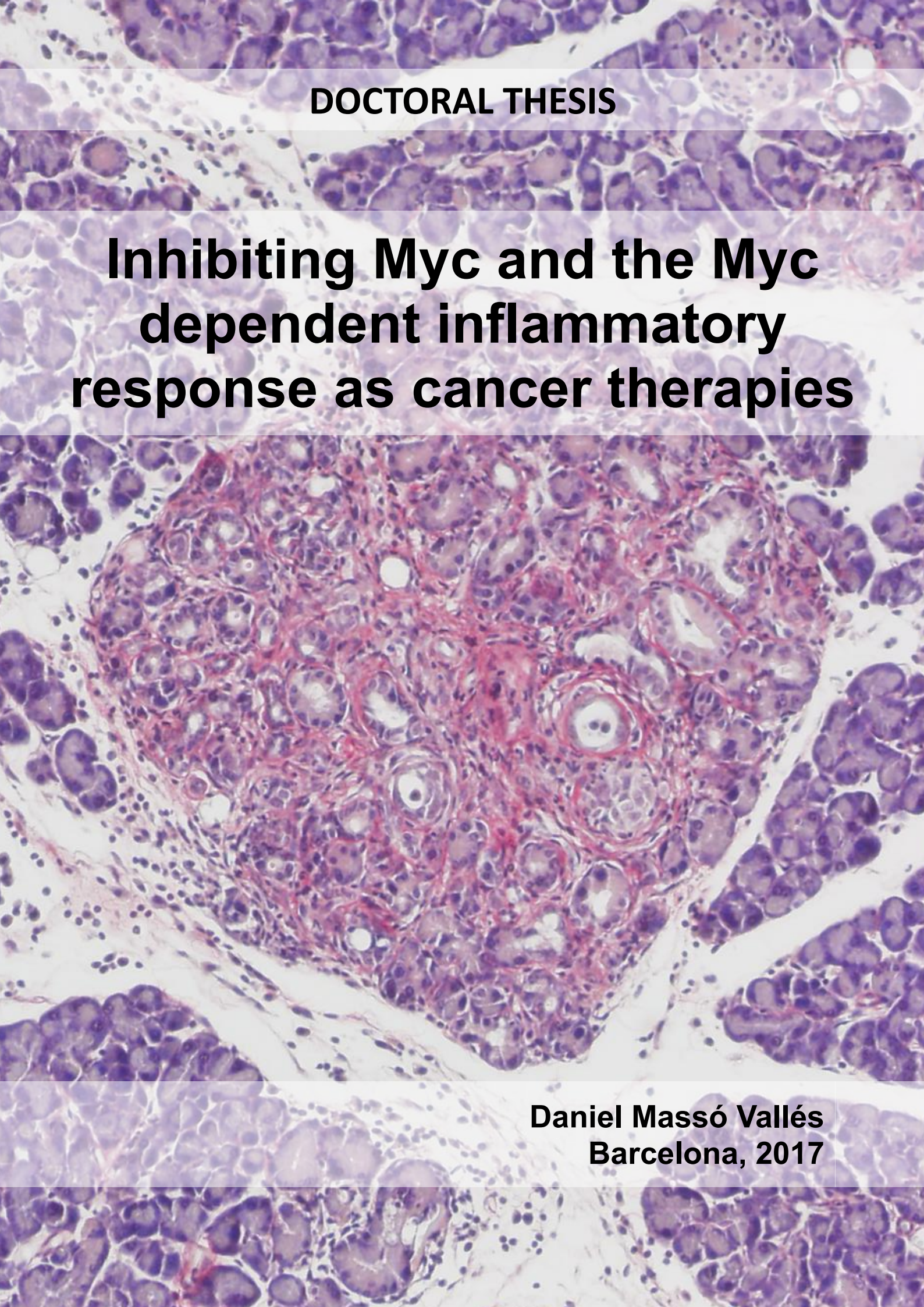

DOCTORAL THESIS

Inhibiting Myc and the Myc dependent inflammatory response as cancer therapies

Daniel Massó Vallés

Barcelona, 2017

Universitat Autònoma de Barcelona

Facultat de Medicina

Departament de Bioquímica i Biologia Molecular

Programa de Doctorat en Bioquímica, Biologia Molecular i Biomedicina

Inhibiting Myc and the Myc dependent inflammatory response as cancer therapies

Thesis presented by Daniel Massó Vallés for the degree of Doctor of Philosophy (PhD) in Biochemistry, Molecular Biology and Biomedicine by Universitat Autònoma de Barcelona

Barcelona, 2017

Director	Tutor	PhD candidate
Dr. Laura Soucek	Dr. Joaquín Arribas López	Daniel Massó Vallés

ACKNOWLEDGMENTS

I would like to start by expressing my most sincere gratitude to all the members of the Soucek group, for making this lab feel like home since the very beginning. To the old ones, for accompanying me all along this experience: **Jony**, thank you for taking the time to carefully proofread all the papers, grant applications, book chapters, and especially this thesis, giving your valuable input. **Toni**, gràcies per haver-me ensenyat tant i per aportar la dosi de qualitat científica que em falta, fent que els meus projectes hagin acabat sent també teus. **Erika**, gràcies per ser la mama del laboratori i per intentar que sigui menys caòtic. **Marie-Eve**, thank you for sharing your vast knowledge with me and with everybody else in the lab, but most importantly, thank you for never losing your signature positive attitude, towards science but also towards life. **Sandra**, gracias por estar siempre dispuesta a echar una mano y por enseñarme más de lo que te he podido enseñar at ti. To the new ones, for being so helpful and making the last part of my thesis so easy: **Mariano**, por enseñarme que se puede combinar talento y humildad; **Génesis**, por los intravenosos malditos; **Sílvia**, per tenir tanta paciència amb les meves infinites preguntes sobre el dipòsit; **Laia**, per les converses de sonats i per aquell matí a la PIP-2; i **Virgínia**, per ser la nostra *dealer* particular i aguantar estoicament els nostres canvis d'última hora. And last but not least, **Laura**, thank you for believing in me more than I believe in myself, encouraging me to start this path and supporting and guiding me throughout this long and exciting journey.

To our temporary visitors, **Lorena**, **Ana** and **Roberta**, thank you for being like a breath of fresh air, each of you in your own way, inside and outside the lab.

To everybody from VHIO that has contributed, in one way or another, not only to work but also to my physical and mental health during this period. Al **Dr. Joaquín Arribas** por haber permitido que consiguiera mi primera beca. To **Kim**, for all the surgeries on Sunday. A les 'birras de pichillas' amb el **Faiz**, l'**Oriol** i l'**Albert**. A l'**Ada**, per transmetre aquesta felicitat contagiosa. A tots els *runners*: **Anne Cé**, por despertar mi pasión por la montaña; **Isa,** per ser la millor organitzadora d'activitats d'aventura, **Irene,** per animar-me a córrer la meva segona marató; i **Josep Lluís** i **Bea**, pels migdies i tardes a Collserola.

To all **the mice** that had to die for the sake of our ultimate goal which is curing cancer.

Finally, thanks to **my family** for suffering all my ups and downs. Als meus pares, **Antoni** i **Elisa**, per l'educació i el suport que m'han donat sempre. Y a mi madre en particular, por compartir experiencias, penas y glorias en este peculiar mundo que es la investigación. Y es que madre no hay más que una. Y a ti, **abuela**, que te fuiste durante esta tesis. Por estar siempre orgullosa de tu nieto; ese que, incluso en tus últimos días, recordabas que cada mañana se iba a investigar con una italiana y un inglés.

BACKGROUND AND PROJECT(S) RATIONALE

The work of this thesis was carried out in the Mouse Models of Cancer Therapies Laboratory led by Dr. Laura Soucek in the Preclinical Research Program of the Vall d'Hebron Institute of Oncology (VHIO). Dr. Soucek's main research focus is the pleiotropic transcription factor Myc, deregulated in multiple types of cancer. She carried out most of her *in vivo* research in Dr. Gerard Evan's former laboratory at the University of California San Francisco (UCSF). A previous study from Dr. Evan's group had demonstrated that exogenous expression of the Myc oncogene in pancreatic β cells, in combination with the antiapoptotic gene *Bcl-X*$_L$, was able to induce and sustain tumorigenesis in mice (Pelengaris et al. 2002). Making use of this mouse model, Dr. Soucek showed that mast cells are necessary for the physical expansion and maintenance of these insulinomas driven by Myc, pointing to them as potential pharmacological targets (Soucek et al. 2007). This model was also used to describe how Myc instructs the tumor microenvironment by inducing tumor angiogenesis, stromal remodeling and local invasion, three common features of the metastatic process (Pelengaris et al. 2002; Soucek et al. 2007).

These two observations were the seed of two projects that are the focus of this thesis. The first project sought to validate the pharmacological inhibition of mast cells as a therapeutic strategy against pancreatic cancer, firstly in insulinoma and later in pancreatic ductal adenocarcinoma (PDAC). The second project focused on the relationship between Myc and metastasis and sought to investigate the feasibility of Myc inhibition in metastatic breast cancer.

For the first project, Dr. Soucek had previously made use of the Bruton's tyrosine kinase (BTK) inhibitor ibrutinib (Pharmacyclics Inc) to inhibit mast cells in Myc-driven insulinoma, showing that this kinase inhibitor was highly effective for the treatment of these tumors, not only preventing tumor expansion but also causing regression of established lesions (Soucek et al. 2011). Encouraged by these data, we employed ibrutinib against the most common and aggressive pancreatic tumor: PDAC. This new project constitutes the first part of this thesis and has led to the publication of a research paper and an editorial (Masso-Valles et al. 2015; Masso-Valles et al. 2016), as well as contributing to the initiation of clinical trials combining ibrutinib with chemotherapy in patients with metastatic PDAC (phase 1/2: NCT02562898 and phase 2/3: NCT02436668).

For the second project, we made use of Omomyc, a Myc dominant negative mutant which Dr. Soucek designed and validated against several tumor types for nearly 20

years, against metastatic breast cancer. We not only demonstrated that Myc inhibition is effective against metastasis, but also obtained encouraging preliminary data by making use of a new Omomyc-based drug that could be employed against triple negative breast cancer and potentially other tumor types. This project constitutes the second part of this thesis and a manuscript is in preparation.

INDEX

ACKNOWLEDGMENTS i
BACKGROUND AND PROJECT(S) RATIONALE iii
INDEX v
ABBREVIATIONS 1
INTRODUCTION 11
1 PANCREATIC CANCER 13
1.1 Mouse models of PDAC 14
1.1.1 Genetically engineered mouse models 14
1.1.2 Patient-derived xenografts 15
2 BREAST CANCER 16
2.1 Mouse models of breast cancer 18
2.1.1 Genetically engineered mouse models 18
2.1.2 Patient-derived xenografts 19
3 MYC 20
3.1 Myc in cancer 23
3.2 Modelling Myc-induced tumorigenesis *in vivo* 24
3.3 Blocking mast cell function as a therapy for Myc-driven insulinoma 26
3.3.1 Ibrutinib 26
3.4 Myc and metastasis 28
3.4.1 Myc and metastatic breast cancer 30
3.5 Myc inhibition 31
3.5.1 Omomyc 32
HYPOTHESIS & OBJECTIVES 35
1 HYPOTHESIS 1 37
2 HYPOTHESIS 2 37
MATERIALS & METHODS 39
1 PART 1 41
1.1 Cell quantification assay 41
1.2 Immunohistochemistry and staining 41
1.3 Flow cytometry 41
1.4 Animal studies 42
1.4.1 Transgenic mice 42
1.4.2 Subcutaneous patient-derived xenografts (PDXs) 43
1.4.3 Orthotopic cell implantation 44
1.5 Statistics 44

2 PART 2 46
2.1 Cell culture 46
2.1.1 Cell lines and lentiviral infections 46
2.1.2 Clonogenic assays 46
2.1.3 Western blots 47
2.1.4 Flow cytometry 48
2.1.5 Proliferation assays 49
2.1.6 Angiogenesis assay 49
2.1.7 Wound healing assay 50
2.1.8 Boyden Chamber assays 50
2.1.9 Clonal selections and bioluminescence quantification *in vitro* 53
2.1.10 Omomyc^{CPP} cell entry by confocal microscopy 53
2.1.11 IC50 calculations 53
2.2 Animal studies 54
2.2.1 Cell-line derived orthotopic model 54
2.2.2 Cell line-derived lung colonization model 55
2.2.3 Cell line-derived orthotopic model with surgical resection and metastatic spread 56
2.2.4 IVIS and μCT imaging 56
2.2.5 Transgenic mice 57
2.3 Statistics 59
RESULTS 61
1 PART 1 63
1.1 Ibrutinib prevents mast cell degranulation and reduces cell proliferation and inflammatory cell infiltration 63
1.2 Ibrutinib reduces collagen deposition 65
1.3 Ibrutinib does not have a direct effect on PDAC tumor cells *in vitro* 67
1.4 Ibrutinib reduces fibrosis in a B-cell independent manner 68
1.5 Ibrutinib's effect on the tumor stroma is mast-cell dependent 70
1.6 Ibrutinib improves the outcome of standard care in a transgenic mouse model of PDAC 72
1.7 The synergistic effect between ibrutinib and gemcitabine is dependent on the tumor stroma 74
2 PART 2 78
2.1 Omomyc is efficiently expressed in a panel of human breast cancer cell lines causing a dose-dependent reduction in colony formation capacity 78
2.2 Omomyc impairs cell proliferation and arrests cells in G0/G1 80

2.3 Omomyc impairs the capacity of MDA-MB-231 cells to induce angiogenesis *in vitro* 83

2.4 Omomyc reduces the metastatic features of breast cancer cells *in vitro* 85

2.5 Omomyc expression reduces the growth of primary mammary tumors *in vivo* in a xenograft orthotopic model 89

2.6 Omomyc expression impairs the growth of lung tumors established after tail vein injection of breast cancer cells 93

2.7 Omomyc expression causes regression of established metastases after primary tumor resection 96

2.8 Generation and characterization of a transgenic mouse model of metastatic breast cancer with inducible expression of Omomyc 100

2.9 Omomyc expression impairs primary tumor growth and metastasis formation in the *MMTV-PyMT* transgenic mouse model of breast cancer 106

2.10 The Omomyc polypeptide: a potential pharmacological approach to inhibit Myc in breast cancer 112

2.11 Treatment with the TMTP1-Omomyc peptide reduces primary tumor growth in a cell line-derived orthotopic model 116

2.12 Treatment with the TMTP1-Omomyc peptide reduces tumor growth in a lung colonization model 118

DISCUSSION 121

1 PART 1 123

2 PART 2 129

CONCLUSIONS 135

1 PART 1 137

2 PART 2 137

BIBLIOGRAPHY 139

ABBREVIATIONS

(-)LM	Negative littermate
µCT	Micro-computed tomography
4-OHT	4-hydroxitamoxifen
A488	AlexaFluor 488
A647	AlexaFluor 647
ABC	Avidin-Biotin Complex
ANOVA	Analysis of variance
APC	Allophycocyanin
Arg	Arginine
ARRIVE	Animal Research: Reporting of In Vivo Experiments
ATP	Adenosine triphosphate
BALB/c	Bagg Albino c
Bcl-2	B-cell lymphoma 2
Bcl-XL	B-cell lymphoma-extra large
BCR	B-cell receptor
BCYRN1	Brain cytoplasmic RNA 1
BET	Bromodomain and extra-terminal domain
B-HLH-LZ	Basic-helix-loop-helix leucine zipper
BLI	Bioluminescence
Blk	B lymphocyte kinase
Bmx	Bone marrow tyrosine kinase gene in chromosome X protein
bp	Base pair
Braf	V-Raf murine sarcoma viral oncogene homolog B
BRCA1	Breast cancer 1
BrdU	Bromodeoxyuridine
BSA	Bovine serum albumin
BTK	Bruton's tyrosine kinase
c#11	Clone 11
C481	Cysteine 481

C57BL/6	C57 black 6
CAF	Cancer associated fibroblast
CD4	Cluster of differentiation 4
CD11b	Cluster of differentiation molecule 11b
CD11c	Cluster of differentiation molecule 11c
CD16	Cluster of differentiation molecule 16
CD25	Cluster of differentiation molecule 25
CD32	Cluster of differentiation molecule 32
CDH1	Cadherin 1
Cdk	Cyclin dependent kinase
CDKN2A	Cyclin-dependent kinase Inhibitor 2A
CEEA	'Comitè Ètic d'Experimentació Animal', *Catalan for* Ethical Committee for the Use of Experimental Animals
CEIC	'Comitè Ètic d'Investigació Clínica', *Catalan for* Clinical Research Ethics Committee
CMFDA	5-chloromethylfluorescein diacetate
CMV	Cytomegalovirus
Cre	Causes recombination or Cyclization recombinase
CTC	Circulating tumor cell
Cy5	Cyanine 5
DAB	3,3'-Diaminobenzidine
DC	Detergent compatible
DMEM	Dulbecco's Modified Eagle's medium
DNA	Deoxyribonucleic acid
DNase	Deoxyribonuclease
dNTP	Deoxynucleoside triphosphate
dox	Doxycycline
E-box	Enhancer box
ECL	Enhanced chemiluminescence

ECM	Extracellular matrix
EDTA	Ethylenediaminetetraacetic acid
EGFR	Epidermal growth factor receptor
EMT	Epithelial-to-mesenchymal transition
ER	Estrogen receptor
Etk	Epithelial and endothelial tyrosine kinase
FBS	Fetal bovine serum
Fbw7	F-box/WD repeat-containing protein 7
FcεRI	High-affinity IgE receptor
Fgr	Feline Gardner-Rasheed sarcoma viral oncogene homolog
FITC	Fluorescein isothiocyanate
Fluc	Firefly luciferase
FSC-A	Forward scatter area
G0/G1 phase	Growth phase 0 / Growth phase 1
Gem	Gemcitabine
GEMM	Genetically engineered mouse model
GFP	Green fluorescent protein
GLI1	Glioma-associated oncogene homolog 1
GUS	β-glucuronidase
H&E	Hematoxylin and eosin
Hck	Hemopoietic cell kinase
HEK293T	Human embryonic kidney cells 293 SV40 large T antigen
HER2	Human epidermal growth factor receptor 2
HER3	Human epidermal growth factor receptor 3
HER4	Human epidermal growth factor receptor 4
HP-β-CD	Hydroxypropyl-beta-cyclodextrin
HRP	Horseradish peroxidase
HUVEC	Human umbilical vein endothelial cells

HUVH	'Hospital Universitari Vall d'Hebron', *Catalan for* University Hospital Vall d'Hebron
Hygro	Hygromicin
i.n.	Intranasal administration
i.p.	Intraperitoneal administration
IACUC	Institutional Animal Care and Use Committee
IC50	Half maximal inhibitory concentration
IF	Immunofluorescence
IgE	Immunoglobulin E
IgG (H+L)	IgG heavy and light chains
IgG	Immunoglobulin G
IHC	Immunohistochemistry
IL-1β	Interleukin 1 beta
IL-6	Interleukin 6
IL-8	Interleukin 8
IL-13	Interleukin 13
INI1	Integrase interactor 1
Ipf1	Insulin promoter factor 1
ITK	Interleukin-2-inducible T-cell kinase
IVIS	In vivo imaging system
JAK3	Janus kinase 3
KPC	Kras, p53, Cre
Kras	V-Ki-ras2 Kirsten rat sarcoma viral oncogene homolog
$Kras^{tm4Tyj}$	Kras targeted mutation 4, Tyler Jacks
Lck	Lymphocyte cell-specific protein-tyrosine kinase
LSL	Lox-STOP-lox
Ly6C	Lymphocyte antigen 6 complex, locus C
Ly6G	Lymphocyte antigen 6 complex, locus G
mAb	Monoclonal antibody

MAPK	Mitogen-activated protein kinase
Max	Myc-associated factor X
MB	Myc box
mBC	Metastatic breast cancer
MC29	Avian myelocytomatosis virus
MCP-1	Monocyte chemoattractant protein 1
MDSC	Myeloid-derived suppressor cell
MHCII	Major histocompatibility complex class II
Miz-1	Myc-interacting zinc finger protein-1
MMP2	Matrix metalloproteinase 2
MMP9	Matrix metalloproteinase 9
MMP13	Matrix metalloproteinase 13
MMTV	Mouse mammary tumor virus
MT	Middle T antigen
Mxi	Max-interacting protein
Myc	v-myc avian myelocytomatosis viral oncogene homolog
c-Myc	Cellular Myc
L-Myc	Lung carcinoma derived Myc
N-Myc	Neuroblastoma derived Myc
v-Myc	Myelocytomatosis viral oncogene
n	Number of replicates
nab-paclitaxel	Nanoparticle albumin-bound paclitaxel
NF-κB	Nuclear factor kappa-light-chain-enhancer of activated B cells
NIH	National Institutes of Health
NK cell	Natural killer cell
NLS	Nuclear localization signal
NOD/SCID	Non-obese diabetic / Severe combined immunodeficiency
NSCLC	Non-small cell lung cancer
NT	Non-treated

Omomyc^{CPP}	Omomyc cell-penetrating peptide
p value	Probability value
p53	Protein 53
PanIN	Pancreatic intraepithelial neoplasia
PBS	Phosphate buffered saline
PCR	Polymerase chain reaction
PDAC	Pancreatic ductal adenocarcinoma
PD-L1	Programmed Death-Ligand 1
PDX	Patient-derived xenograft
Pdx1	Pancreatic and duodenal homeobox 1
PE	Phycoerythrin
pH	Potential of hydrogen
PI	Propidium iodide
PI3K	Phosphatidylinositol 3-kinase
pIns	Insulin promoter
Pol III	RNA polymerase III
PP2A	Protein phosphatase A
PR	Progesterone receptor
PSC	Pancreatic stellate cell
pTEFb	Positive transcription elongation factor
PTX	Paclitaxel
PVDF	Polyvinylidene difluoride
PyMT	Polyomavirus middle T antigen
Ras	Rat sarcoma
RhoA	Ras homolog gene family, member A
RIP	Rat insulin promoter
RNA	Ribonucleic acid
miRNA	Micro RNA
mRNA	Messenger RNA

siRNA	Small interfering RNA
RNase	Ribonuclease
RPMI	Roswell Park Memorial Institute medium
rtTA	Reverse tetracycline transactivator
S phase	Synthesis phase
S62	Serine 62
SCF	Skp, Cullin, F-box containing complex
SCLC	Small cell lung cancer
SD	Standard deviation
SEM	Standard error of the mean
Skp2	S-phase kinase-associated protein 2
SMAD	*Contraction of* Sma (Small) *and* Mad (Mothers against decapentaplegic)
Snail	Zinc finger protein SNAI1
SPF	Specific pathogen free
Src	*Short for* sarcoma
c-Src	Tyrosine-protein kinase Src
suc	Sucrose
SV40	Simian virus 40
T58	Threonine 58
TAD	Transactivation domain
Tg	Transgene
Tg(Ipf1-cre)1Tuv	Transgene Ipf1-Cre insertion 1, David A Tuveson
TGL	Herpes simplex virus thymidine kinase 1, GFP, firefly luciferase
TNBC	Triple negative breast cancer
TNFα	Tumor necrosis factor alpha
T-Omomyc	TMTP1-Omomyc
TP53	Tumor protein 53
TRE	Tetracycline response element

Trp53	Transformation-related protein 53
$Trp53^{tm1Gev}$	Trp53 targeted mutation 1, Gerard I Evan
TRRAP	Transformation/transcription domain-associated protein
UAT	'Unitat d'Alta Tecnologia', *Catalan for* High Tehcnology Unit
UCSF	University of California San Francisco
VEGF	Vascular endothelial growth factor
V-Ha-Ras	Hras / Harvey rat sarcoma viral oncogene homolog
VHIO	Vall d'Hebron Institute of Oncology
VHIR	'Vall d'Hebron Institut de Recerca', *Catalan for* Vall d'Hebron Research Institute
Wnt	Wingless-related integration site
ZEB1	Zinc finger E-box binding homeobox 1
αSMA	Alpha smooth muscle actin

INTRODUCTION

1 PANCREATIC CANCER

Pancreatic cancer comprises different diseases with the common feature of arising in the same organ. Pancreatic tumors can have a neuroendocrine or exocrine origin, giving rise to two distinct diseases with different clinical outcomes. Neuroendocrine tumors include gastrinoma, insulinoma, glucagonoma and miscellaneous islet cell tumors, and represent a minority of pancreatic cancer cases (1-2%). They have generally better prognosis than exocrine tumors and can be cured by surgical resection (Oberg and Eriksson 2005; Metz and Jensen 2008). In contrast, pancreatic ductal adenocarcinoma (PDAC) is the most common exocrine pancreatic malignancy, it is characterized by poor prognoses and accounts for more than 80% of the malignant neoplasms of the pancreas (Alexakis et al. 2004). Therefore, the term pancreatic cancer is often used to refer to PDAC only. Non-ductal exocrine tumors include serous cystadenocarcinoma, mucinous cystadenocarcinoma, intraductal papillary-mucinous carcinoma, acinar cell carcinoma acinar cell cystadenocarcinoma, mixed acinar-endocrine carcinoma, pancreatoblastoma and solid-pseudopapillary carcinoma (Hamilton and Aaltonen 2000). PDAC is the fourth most common cause of cancer death in the Western world and, while cancer mortality rates have in general been recently decreasing, it has a uniquely increasing mortality trend and prognosis has remained virtually unchanged for decades (Hariharan et al. 2008; Malvezzi et al. 2017). It is usually diagnosed at advanced stages, which is often due to nonspecific or absent symptoms, a lack of sensitive and specific tumor markers and difficulties in imaging early-stage tumors (Kleeff et al. 2016). Approximately 40% of patients are diagnosed with locally advanced or metastatic disease, which severely limits the number of patients who can undergo surgical resection. According to the American Cancer Society, the overall survival rates at 1 and 5 years are only 25% and 6%, respectively. The 5-year survival for localized disease is approximately 20%, and the median survival is 10 and 6 months for advanced and metastatic disease (which affects 80% of individuals), respectively (www.cancernetwork.com). Hence, there is an urgent need for new and effective therapies.

Nowadays, patients diagnosed with unresectable PDAC are treated with chemotherapy with or without radiation. Gemcitabine has been the standard first-line treatment for pancreatic cancer since 1997, and combination with nanoparticle albumin-bound (nab)-paclitaxel has recently been shown to significantly extend survival (Von Hoff et al. 2013).

The mutational profile of PDAC is highly homogeneous, with >90% of tumors presenting activating mutations in Kras. Inactivating mutations in TP53, CDKN2A and SMAD are present in 40-80% of tumors (Kleeff et al. 2016). PDAC is characterized by dense desmoplasia, composed of extracellular matrix (ECM), endothelial cells, immune cells, fibroblasts and stellate cells that, together, compose up to 90% of the tumor volume. The immune compartment is composed of T cells (a majority being CD4+ regulatory T cells), myeloid-derived suppressor cells, macrophages and mast cells (Evans and Costello 2012). This epithelial and stromal compartment appears to enhance the aggressive nature of the disease and its resistance to therapy. Indeed, the dense stromal fibroinflammatory reaction results in decreased blood supply, poor drug delivery (Mahadevan and Von Hoff 2007) and hypoxia (Koong et al. 2000). Hence, therapies targeting the stroma may be key to improving the clinical outcomes for pancreatic cancer patients.

1.1 Mouse models of PDAC

Mouse models of pancreatic cancer, as for most cancers, include genetically engineered mouse models (GEMMs) and patient-derived xenografts (PDXs). During this thesis, we wrote a book chapter discussing such mouse models of cancer and their main advantages and disadvantages (Beaulieu et al. 2016).

1.1.1 Genetically engineered mouse models

The main advantages of GEMMs rely on the fact that the tumor develops through all stages of epithelial transformation with a native stroma, immune system and microenvironment. These models not only mimic relevant pathophysiologic features of human tumorigenesis accurately but also recapitulate the sequence of molecular events that give rise to cancer.

Given that *Kras* is mutated in the vast majority of PDAC patients, the generation of the first mouse model with tissue-specific expression of a mutated *Kras* allele in the pancreas was a crucial step forward in the study of the disease. The most common Kras-mutated mouse used in preclinical studies harbors a heterozygous *Lox-STOP-lox* $Kras^{G12D}$ transgene knocked in the endogenous *Kras* locus (Jackson et al. 2001) and a *Cre* recombinase under the control of the pancreas-specific *Pdx1* promoter (Hingorani et al. 2003). In this model, the *STOP* cassette is floxed out in pancreatic tissue by the

recombinase and the mutated copy of *Kras* is expressed. The model was further improved with the addition of a *Lox-STOP-lox* mutated *p53* knocked-in its endogenous locus, generating the mouse model known as KPC (Hingorani et al. 2005). In parallel, Dr. Gerard Evan's laboratory generated a conditionally expressed *p53* gene by fusing it with a mutant estrogen receptor ($p53^{ER}$) and inserted it in the endogenous *p53* locus (Christophorou et al. 2005). These mice can be toggled between wild-type and p53-deficient states by intraperitoneal injection of tamoxifen. Therefore, they are functionally p53 null in the absence of estrogen ligand. In Dr. Soucek's lab, KPC-like mice were generated taking advantage of the different models and crossing $LSLKras^{G12D}$*;Pdx1-Cre* with $p53^{ER/ER}$ mice. These animals rapidly develop all the precursors of PDAC (pancreatic intraepithelial neoplasias - PanIN1a/b, PanIN2 and PanIN3) that become adenocarcinomas at approximately 8 weeks of age. Importantly, these tumors recapitulate the dense desmoplastic stroma present in human PDAC. Still, KPC and KPC-like mice are not the only GEMMs used in preclinical research, and many more have been established (Herreros-Villanueva et al. 2012).

1.1.2 Patient-derived xenografts

Engraftment of tumor biopsies from patients and inoculation of commercial human cell lines into immunocompromised mice is a common strategy used for drug validation in PDAC. Direct engraftment preserves better the original tumor architecture and stromal component. The role of the protein and proteoglycan mesh structurally supporting the cells, the ECM, is increasingly recognized as being crucial in cancer progression. In fact, the biophysical interplay between tumor cells and ECM has been shown to profoundly influence tumor growth, cell migration, signaling, and even drug response (Choi et al. 2014). On the other hand, commercial cell lines constitute valuable tools, enabling monitoring of tumor growth through more direct imaging and allowing the modeling of novel potential targeted therapies through genetic engineering of the tumor cells themselves (Qiu and Su 2013). Indeed, by allowing clonal expansion and manipulation *in vitro* (infection with lentiviruses, fluorescent markers, luciferase etc.) they enable the application of one of the "3 Rs" of humane animal experimentation: replacement. Furthermore, much can be learned from these cells in culture prior to *in vivo* work. Commonly used PDAC human cell lines used for *in vivo* growth include MIA PaCa-2, AsPC-1, HPAF-2 and Capan-1, among others (Hotz et al. 2003). Tumor masses and cell lines can be inoculated either subcutaneously or orthotopically. Subcutaneous xenograft represents the easiest type of implantation, and the most

widely used. However, it does not reflect the natural tumor environment and rarely produces metastasis. Orthotopic tumor implantation allows the tumor to grow in a more natural anatomic microenvironment with regards to the pH, oxygen, nutrient and hormone conditions, and therefore often mimics more accurately the original human tumor when analyzing histology, gene expression profiles and metastatic potential compared to heterotopic transplants (Rubio-Viqueira and Hidalgo 2009). However, orthotopic xenografts of PDAC generally require more elaborate surgical protocols and technical skills to be achieved than heterotopic xenografts, especially when engrafting biopsies instead of cell suspensions.

2 BREAST CANCER

Breast cancer is the most common cancer in women and the second leading cause of cancer mortality, with 1.7 million new cases annually and 522,000 estimated deaths globally (Ferlay J 2013). It is a highly heterogeneous disease and therefore divided into histological and molecular subtypes (Weigelt and Reis-Filho 2009). Historically, patients have been classified into four intrinsic molecular subtypes by immunohistochemistry (IHC) - Luminal A, luminal B, HER2-enriched and triple negative - based on the expression levels of estrogen receptor (ER), progesterone receptor (PR), amplification of human epidermal growth factor receptor 2 (HER2) and proliferation rate (Ki67 positivity). These molecular subtypes differ in incidence, prognosis and treatment options (Ooe et al. 2012; Park et al. 2012; Goldhirsch et al. 2013) (table 1 and figure 1).

Molecular subtype	Percentage of patients	Hormone receptors, HER2 and Ki67 status	Treatment
Luminal A	40-60%	ER+ and/or PR+, Ki67low, HER2-	Endocrine therapy
Luminal B	10-20%	ER+ and/or PR+, Ki67high, HER2-	Endocrine therapy ± chemotherapy
		ER+ and/or PR+, HER2+	Endocrine therapy + anti-HER2 therapy + chemotherapy
HER2-enriched	10-20%	ER-, PR-, HER2+	Anti-HER2 therapy + chemotherapy
Triple negative	15-20%	ER-, PR-, HER2-	Chemotherapy

Table 1. Intrinsic molecular subtypes of breast cancer with consensus recommendations of systemic treatment. ER: estrogen receptor. PR: progesterone receptor. HER2: human epidermal growth factor receptor 2. Adapted from (Prat et al. 2011)

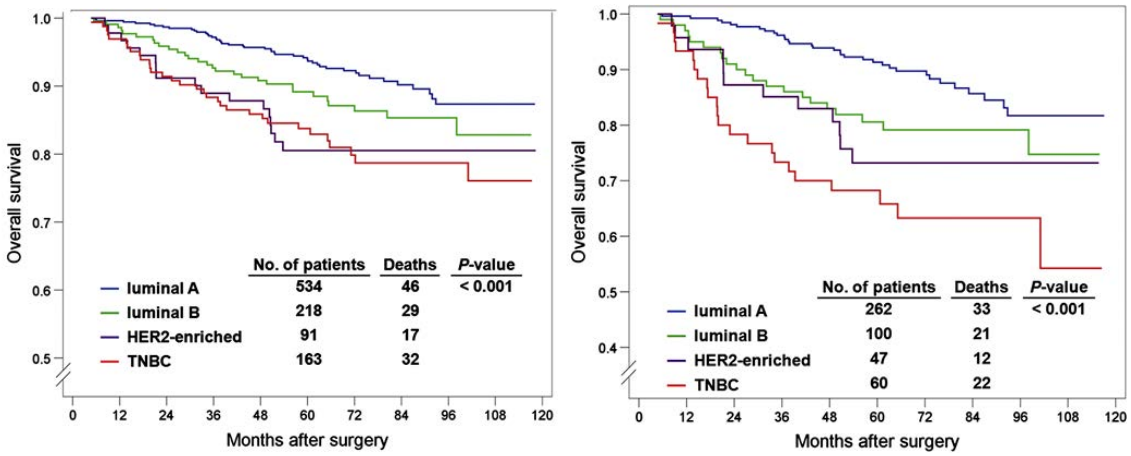

Figure 1 (Park et al. 2012). Overall survival in a cohort of breast cancer patients with lymph node-negative (left panel) or lymph node-positive (right panel) tumors according to molecular subtypes. HER2: human epidermal growth factor receptor 2. TNBC: triple negative breast cancer.

Luminal tumors are hormone dependent and are usually treated with endocrine therapy (mainly tamoxifen), alone or in combination with chemotherapy. HER2-enriched patients are treated with a combination of chemotherapy and anti-HER2 targeted therapies (trastuzumab, pertuzumab, lapatinib), whose introduction in the clinic led to a clear increase in overall survival (Goldhirsch et al. 2011). However, none of the recent advances in personalized medicine are applicable to triple negative breast cancer (TNBC) and surgery, radio- and cytotoxic chemotherapy still remain the norm to delay cancer progression and prolong life. TNBCs are a heterogeneous group of tumors with one common feature: a distinctly aggressive nature with higher rates of relapse and shorter overall survival in the metastatic setting compared with other subtypes of breast cancer (Abramson et al. 2015). Hence, their prognosis remains dire, with an average 18-24 months median survival for metastatic disease.

The appearance of global gene expression analyses using high-throughput technologies has improved our understanding of the heterogeneity in breast cancer. Today, genomic studies have established five breast cancer intrinsic subtypes (Luminal A, Luminal B, HER2-enriched, Claudin-low, Basal-like) and a Normal Breast-like group (Prat and Perou 2011). However, tests to identify them are not widely used in the clinical practice yet (Goldhirsch et al. 2013).

Despite major improvements in prevention, diagnosis and treatment, many patients still develop metastatic breast cancer (mBC). Due to the selective pressure imposed on the

primary tumors, metastases evolve and differentiate, sometimes acquiring characteristics of more aggressive subtypes (Cejalvo et al. 2017). Therefore, most metastatic patients become resistant to primary therapy and eventually die from their disease. Regardless of the molecular subtype, mBC is essentially incurable, with only 1% to 3% of patients with chemotherapy-naïve mBC remaining long-term disease-free after systemic therapy (Lu et al. 2009).

2.1 Mouse models of breast cancer

As in the case of pancreatic cancer, mouse models of breast cancer include genetically engineered mouse models (GEMMs) and patient-derived xenografts (PDXs).

2.1.1 Genetically engineered mouse models

The most common strategy to generate GEMMs of breast cancer consists in transgenic expression of an oncogene specifically within the mouse mammary epithelium under the control of a strong mammary epithelial promoter. This is a clinically relevant model of tumor initiation and progression, recapitulating the stepwise procession that cells undergo from hyperplasia to ductal carcinoma in situ and then to invasive ductal carcinoma. Importantly, this process occurs within the context of the native stromal matrix (requiring stromal remodeling and angiogenesis, two essential drivers of metastasis) and in the presence of the native immune system.

The *MMTV-PyMT* mouse model is one of the most used. It was generated by conditional expression of the Polyomavirus middle T antigen (PyMT) to the mammary epithelium by fusing it with the steroid-regulated mouse mammary tumor virus (MMTV) long terminal repeat (Guy et al. 1992). PyMT is a very potent oncogene that localizes in the cell membrane and, despite lacking intrinsic tyrosine kinase activity, has the capacity to recruit tyrosine kinases of the Src family (Courtneidge and Smith 1983). It activates several signaling pathways that lead to tumorigenesis, namely the mitogen-activated protein kinase (MAPK) and phosphatidylinositol 3-kinase (PI3K) cascades (Dilworth 2002) (figure 2).

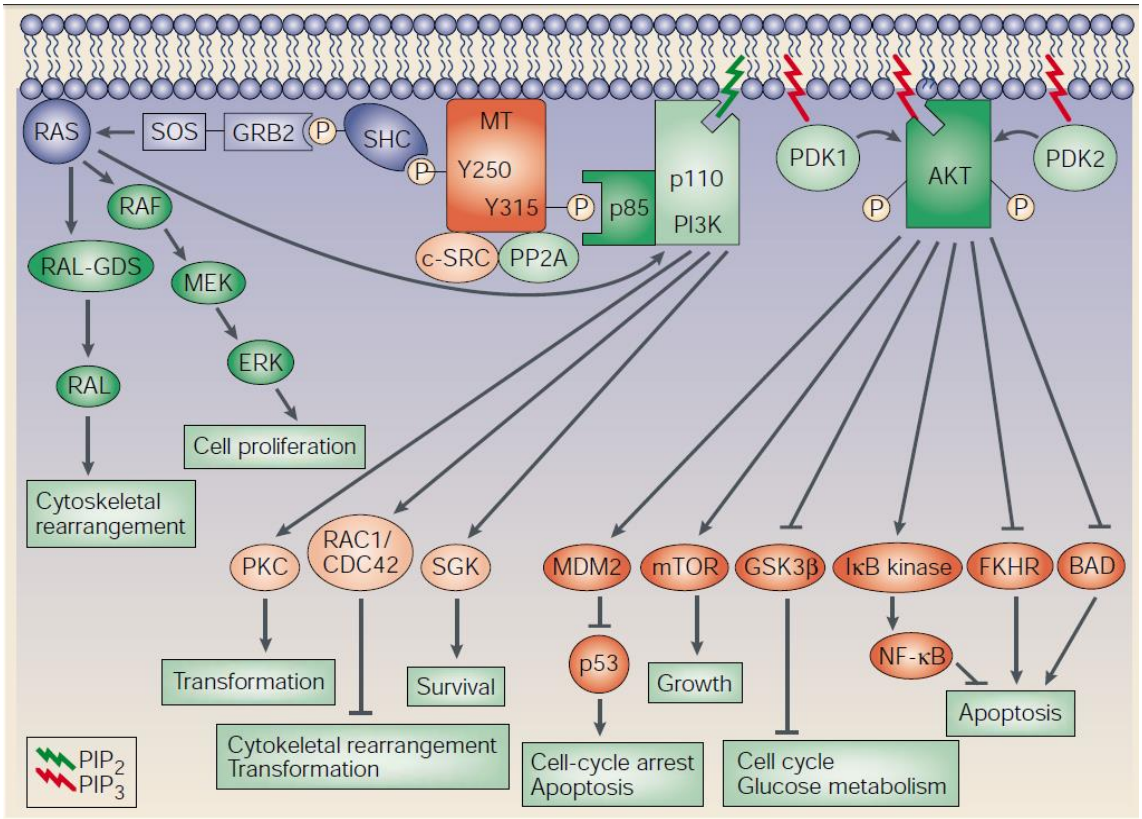

Figure 2 (Dilworth 2002). Middle T antigen (MT) stimulated signaling pathways. Membrane-bound MT binds to protein phosphatase A (PP2A) and c-SRC, which results in the phosphorylation of several tyrosine residues in the carboxy-terminal end of MT. The Ras and phosphatidylinositol 3-kinase (PI3K) cascades become activated, leading to cell proliferation, inhibition of apoptosis and potentiation of other oncogenic processes.

As a consequence, female carriers of *MMTV-PyMT* develop palpable mammary tumors as early as 5 weeks of age. The primary tumors are multifocal, highly fibrotic adenocarcinomas that involve the entire mammary fat pad. Importantly, between 85 and 100% of tumor-bearing females develop pulmonary metastases (Kim and Baek 2010), making it one of the few breast cancer mouse models with a high penetrance of metastasis, allowing for prevention and intervention studies alike. Other breast cancer GEMMs have been generated by fusing the *MMTV* promoter with multiple oncogenes, including *Myc* and *HER2*, among others (Hutchinson and Muller 2000).

2.1.2 Patient-derived xenografts

Establishment of breast cancer PDXs from tumor biopsies has been historically challenging, with low rates engraftment when compared to other tumor types, plus the need for estrogen supplementation in hormone-dependent tumors (Tentler et al. 2012). However, the correlation between the rate of engraftment and patient survival indicates

that PDXs recapitulate the aggressiveness of the tumor and reflect human disease to a great extent.

On the other hand, xenografts from human immortalized cell lines have been widely used in the literature and allow the establishment of mouse models from all intrinsic molecular subtypes. They present several limitations, mainly the absence of the tumor stroma and microenvironment, lack of heterogeneity and artificial selection in plastic. However, the high degree of characterization of many cell lines, combined with the simplicity of the procedures and the lack of variability, allows the performance of tightly controlled experiments. Furthermore, due to the location of the mammary fat pads, cells can be easily inoculated orthotopically to generate primary mammary tumors.

In addition, tail vein or intracardiac injection of breast cancer cells is widely used as an artificial way to model metastasis. In this regard, the triple negative and metastatic MDA-MB-231 cell line has become a staple in metastatic breast cancer research (Kim and Baek 2010; Iorns et al. 2012; Yang et al. 2012). By generating variants of MDA-MB-231 with tropism to different target tissues, researchers at Dr. Joan Massagué's laboratory identified a panel of genes that mediated organ-specific metastasis to the bones, lungs and brain (Kang et al. 2003; Minn et al. 2005; Bos et al. 2009).

3 MYC

The Myc family of proteins comprises a group of three broadly isofunctional basic-helix-loop-helix leucine zipper (B-HLH-LZ) transcription factors (c-Myc, N-Myc and L-Myc) that coordinate expression of the diverse intracellular and extracellular programs that together are necessary for growth and expansion of somatic cells. Its expression is tightly regulated at the DNA, RNA and protein levels and it is not transcribed in quiescent cells but rapidly induced in response to growth factor stimuli (Tansey 2014).

Myc is a global transcriptional regulator that controls the expression of up to one third of human genes. It can bind to approximately 15% of the genome and regulates genes encoding proteins or non-coding RNA products (Patel et al. 2004; Dang et al. 2006) that together control growth, proliferation, differentiation, cell adhesion, migration, angiogenesis, differentiation, transformation, apoptosis, senescence and immunity (Meyer and Penn 2008; Hanahan and Weinberg 2011; Gnanaprakasam and Wang 2017).

The Myc protein consists of 3 differentiated regions: a transactivation domain (TAD) on the N-terminal, a central region, and a B-HLH-LZ on the C-terminal for DNA binding and dimerization (Figure 3).

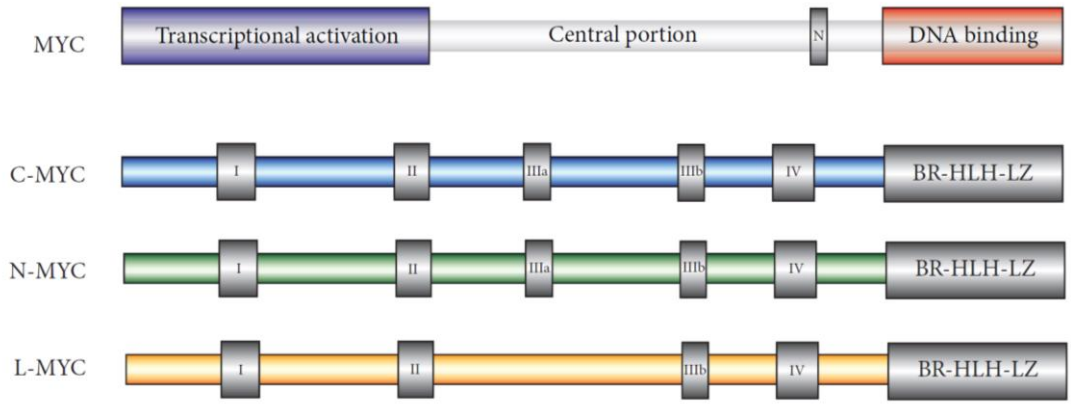

Figure 3 (Tansey 2014). Generic representation of a mammalian Myc protein, indicating the transcriptional activation domain, the central portion, one canonical nuclear localization signal (N), and the region involved in DNA binding via interaction with Max. Below, representation of conserved sequences present in c-, N- and L-Myc family members, indicating Myc boxes I, II, III and IV.

Localized along its sequence, Myc contains four conserved regions known as Myc boxes (MB). The TAD controls transcription of Myc target genes. It contains MBI, which contributes to gene activation and protein degradation, and MBII, responsible for assembly of the transcriptional machinery that is critical for the majority of Myc's functions. MBIII and MBIV are located in the central region. MBIII has been implicated in transcriptional repression, apoptosis, transformation, and lymphomagenesis. MBIV is implicated in transcriptional activation and repression linked to apoptosis and transformation, as well as modulation of DNA-binding. The B-HLH-LZ domain consists on the basic region, necessary for binding to consensus sequences called Enhancer boxes (E-boxes, 5'-CACGTG-3'), and a helix-loop-helix leucine zipper domain, essential for the dimerization with Myc's obligate B-HLH-LZ partner termed Myc-associated factor X (Max) (Vita and Henriksson 2006) (Figure 4). Myc contains two nuclear localization signals (NLS), one in the central part and one in the basic region.

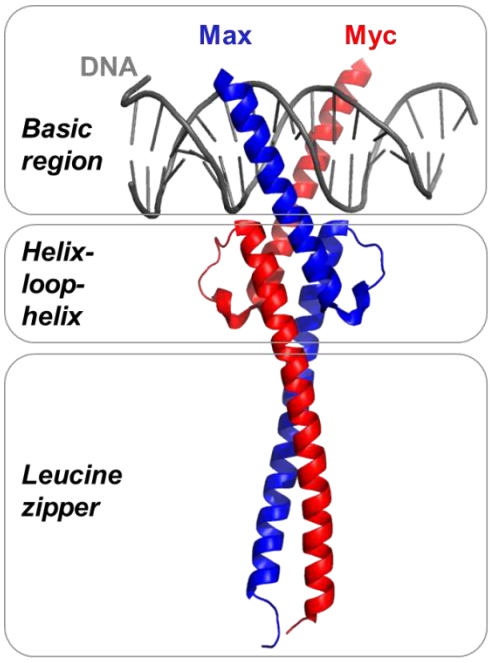

Figure 4 (modified from Nair and Burley 2003). X-ray structure of the basic helix-loop-helix leucine zipper region of a Myc (red) and Max (blue) heterodimer bound to DNA (grey). Protein Data Bank accession number: 1NKP.

Myc does not homodimerize, but heterodimerization with Max allows the basic domains to adopt helical shapes to anchor onto the DNA major grooves, activating gene transcription by several mechanisms. Recruitment of TRRAP and INI1 causes histone acetylation and chromatin remodeling (Cheng et al. 1999; McMahon et al. 2000), and binding to pTEFb activates RNA polymerase II, releasing it from a pausing state to increase the rate of gene transcription (Kanazawa et al. 2003; Rahl et al. 2010). Max, but not Myc, dimerizes with other B-HLH-LZ proteins from the Mad/Mxi family, which bind the same E-boxes as Myc/Max dimers but act as transcriptional repressors instead (Chen et al. 1995; Rottmann and Luscher 2006).

Furthermore, Myc can also induce transcriptional inhibition, and it does so through different mechanisms, the most convincingly-demonstrated being its interaction with Myc-interacting zinc finger protein-1 (Miz-1) (Peukert et al. 1997; Staller et al. 2001). Myc protein stability is regulated by phosphorylation at conserved residues serine 62 (S62) and threonine 58 (T58) (Sears 2004). Transient stabilization occurs through phosphorylation of S62 by ERK or CDK kinases, whereas phosphorylation of T58 by GSK3β triggers dephosphorylation of S62 by PP2A, ubiquitination by the SCF-Fbw7 E3 ligase, and proteasomal degradation (Welcker et al. 2004).

3.1 Myc in cancer

Myc has been linked to tumorigenesis since its discovery, and owes its name to the **my**elo**c**ytomatosis (a form of tumor involving the myelocytes) observed in chicken infected with the MC29 virus strain. The MC29 virus contains the myelocytomatosis viral oncogene (v-Myc) (Mellon et al. 1978; Sheiness et al. 1978), which allowed the identification of its homolog in the genome, c-Myc (Vennstrom et al. 1982), first in chicken and later in humans. L-Myc and N-Myc were identified shortly after (Kohl et al. 1983; Schwab et al. 1983; Nau et al. 1985).

Even though Myc is very rarely mutated in cancer - mutations are only found in some hematological malignancies, mainly Burkitt's lymphoma - its expression is deregulated in most tumor types (Tansey 2014). That is because, unlike other oncogenes, the coding sequence of Myc does not need to be changed in order for its oncogenic potential to be unleashed. At the DNA level, the *Myc* gene itself is frequently amplified and it can also be subject to viral insertional events and chromosomal translocations that alter its expression. When transcribed, *Myc* mRNA can become stabilized through both direct and indirect regulatory events. At the protein level, alterations on Myc's phosphorylation status can alter its turnover rate. Finally, since Myc is a central node where many oncogenic signals converge (Ras, PI3K, Wnt, Notch, NF-κB,...), alterations in these upstream pathways can drive its aberrant expression (Meyer and Penn 2008).

In physiologic conditions, Myc levels are low in most somatic tissues, and high in proliferating tissues like the intestinal crypts or during tissue repair and embryogenesis, where it is tightly regulated. Sustained aberrant Myc levels, however, coupled with loss of stress response checkpoints (Bcl-X_L, p53) or induction by mitogenic signals (Ras), unleash Myc's oncogenic potential. Several studies suggest that different cellular responses to physiologic and oncogenic Myc levels are controlled by promoter affinity. One common view is that, at physiologic levels of Myc, occupancy of high-affinity DNA-binding sites drives 'house-keeping' genes. At high oncogenic levels of Myc, invasion of low-affinity sites and enhancer sequences alter the transcriptome regulating specific sets of genes (Sabo et al. 2014; Walz et al. 2014; Hsieh and Dang 2016) (figure 5). Alternatively, activation of some genes could occur only if the Myc/Max complex is present long enough to recruit other cofactors (including chromatin remodeling ones), which would be consistent with tumorigenesis occurring in the presence of low but persistent levels of Myc (Murphy et al. 2008).

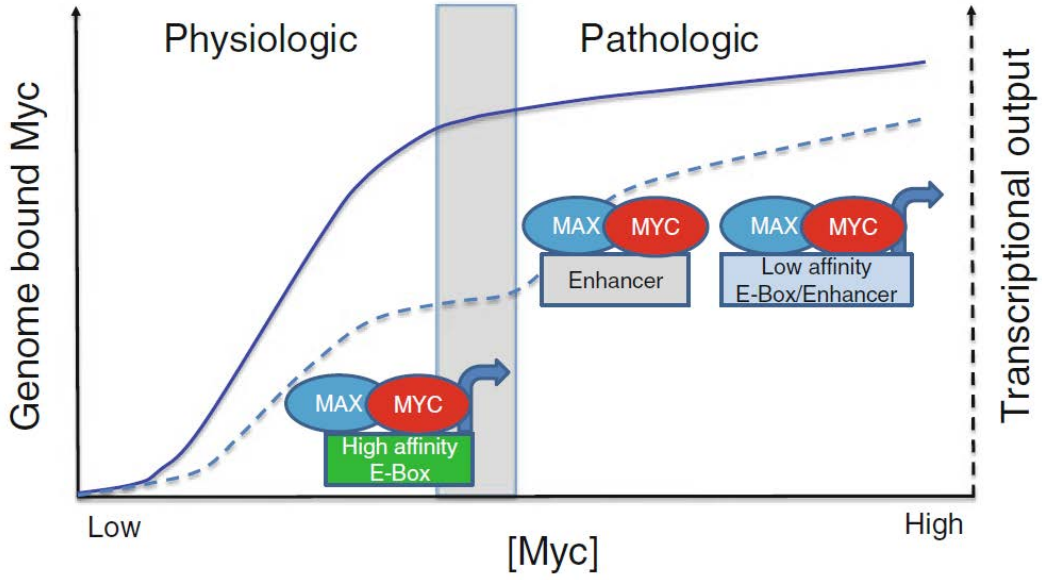

Figure 5 (Hsieh and Dang 2016). Hypothetical representation of the different transcriptional output caused by increasing levels of the Myc protein. The solid line represents the number of genes in the genome that are bound by Myc and the dashed line represents the level of transcription of Myc-bound genes. In physiologic conditions (low Myc), the Myc-Max heterodimer preferentially binds to the high-affinity E-box-containing genes and transactivates the expression of some, but not all, genes bound by Myc. Conversely, in the pathological setting, such as cancer, where Myc level is elevated, Myc-Max heterodimer binds to the enhancers ('enhancer invasion') and the low-affinity E-box-containing genes in addition to the high-affinity target genes to induce a broader and greater transcriptional output for cell growth and proliferation.

3.2 Modelling Myc-induced tumorigenesis *in vivo*

To explore the role of Myc in carcinogenesis, researchers at Dr. Gerard Evan's laboratory developed a mouse model of β cell tumorigenesis by coexpressing a switchable form of *c-Myc* together with the antiapoptotic *Bcl-X*$_L$ gene (Pelengaris et al. 2002). First, human *c-Myc* was fused with a 4-hydroxitamoxifen (4-OHT)-responsive mutant estrogen receptor (*c-MycER*^{TAM}) and put under control of an insulin promoter (*pIns*). *pIns-c-MycER*^{TAM} mice treated with tamoxifen exhibited rapid proliferation of β cells, but the proapoptotic activity of Myc predominated over its mitogenic capability, causing massive cell death that was restricted to β cells. *pIns-c-MycER*^{TAM} mice were then crossed with mice constitutively expressing the antiapoptotic *Bcl-2* homolog *Bcl-X*$_L$ under the control of the rat insulin promoter (*RIP*). Upon injection of tamoxifen, *pIns-c-MycER*^{TAM}*;RIP-Bcl-X*$_L$ mice still exhibited high levels of β cell proliferation but apoptosis was prevented, leading to the appearance of insulinomas. In the absence of apoptosis, c-Myc was able to induce dedifferentiation, angiogenesis, and invasiveness through loss of E-cadherin in a reversible manner, since tamoxifen withdrawal induced rapid

tumor regression and vasculature collapse (Pelengaris et al. 2002). These results demonstrated that c-Myc is required not only for the induction of multiple aspects of neoplastic progression, but also for its maintenance.

Myc not only transforms tumor cells but also has a profound effect on the tumor microenvironment, inducing stromal remodeling and angiogenesis. In *pIns-c-MycER^{TAM};RIP-Bcl-X$_L$* mice, Myc expression in β cells induces interleukin 1β (IL-1β)-mediated release of vascular endothelial growth factor (VEGF), promoting endothelial cell proliferation (Shchors et al. 2006). To further characterize the role of Myc in the non-cell autonomous aspects of tumorigenesis, Dr. Laura Soucek made use of the *pIns-c-MycER^{TAM};RIP-Bcl-X$_L$* mouse model (Soucek et al. 2007) and described the expression of several chemokines with chemoattractant activity towards immune cells upon Myc activation. As a consequence of this chemotaxis, mast cells accumulated in the mesenchyme surrounding the pancreas just 24 hours after tamoxifen administration (just before tumor angiogenesis onset) while macrophages and neutrophils accumulated in the islets after 1 week. Since mast cells are an abundant source of angiogenic and stromal remodeling factors such as VEGF, basic fibroblast growth factor, transforming growth factor-β, tumor necrosis factor-α (TNFα) and matrix metalloproteinase 9 (MMP9), pharmacological and genetic approaches were used to inhibit their function and assess the impact on angiogenic events. First, *pIns-c-MycER^{TAM};RIP-Bcl-X$_L$* mice were crossed with mast cell deficient *Kit$^{W\text{-}sh}$* mice, and that completely prevented Myc-induced islet expansion. In parallel, insulinoma-bearing mice were treated with sodium cromoglycate, to block mast cell degranulation. That resulted not only in the prevention of tumor expansion, but also regression of preformed tumors. Interestingly, mast cell blockade did not interfere with the first round of endothelial cell proliferation induced by Myc, but it was necessary for its maintenance, causing vasculature failure and hypoxia after only 3 days (Soucek et al. 2007).

Taken together, these results confirmed that:

- Mast cells are a potential target for therapy in pancreatic cancer.
- Myc is an instructor of dedifferentiation, cell-to-cell contact, invasion and angiogenesis, all key aspects of metastasis.

3.3 Blocking mast cell function as a therapy for Myc-driven insulinoma

Dr. Laura Soucek demonstrated that mast cells are good targets for the treatment of Myc-driven insulinoma. However, whereas sodium cromoglycate is an effective mast cell stabilizer, it has been designed for topical delivery (aerosol) and is a very poor systemic drug with low bioavailability in humans, impeding its use in patients. This issue prevented the studies published in 2007 from having a direct impact on clinical practice.

3.3.1 Ibrutinib

Ibrutinib (tradename Imbruvica®, also known as PCI-32765, figure 6) is a first-in-class, irreversible small-molecule inhibitor of Bruton's tyrosine kinase (BTK) developed by Pharmacyclics that binds covalently to cysteine C481 within BTK's ATP-binding pocket.

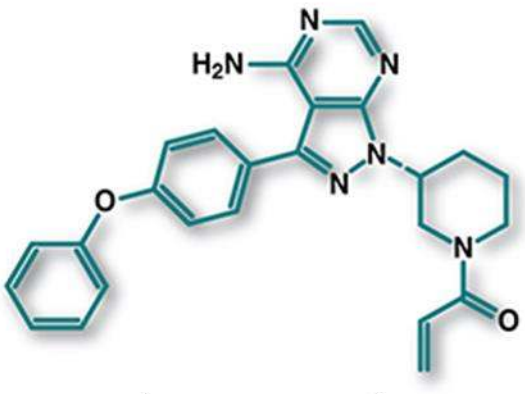

Figure 6 (DeRuiter et al. 2014). Structural formula of ibrutinib.

Since BTK is a Tec family non-receptor tyrosine kinase that is specifically required for B-cell receptor (BCR) signaling, ibrutinib was initially developed for the treatment of B-cell malignancies (Honigberg et al. 2010). Currently, it is approved for first-line treatment of chronic lymphocytic leukemia (Burger et al. 2015), and for the treatment of mantle-cell lymphoma and Waldenström's macroglobulinemia patients that have received at least one previous therapy (Wang et al. 2013; Treon et al. 2015). But BTK is also critical for mast cell degranulation and cytokine release, acting downstream of the high-affinity IgE receptor (FcεRI) (Iwaki et al. 2005; Gilfillan and Tkaczyk 2006; Jensen et al. 2008) (Figure 7).

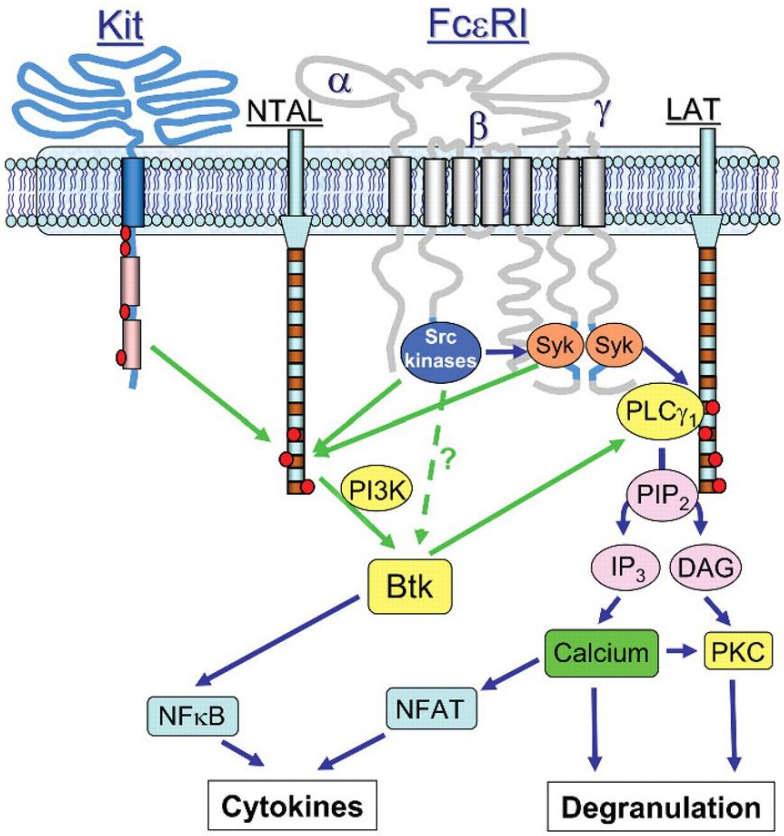

Figure 7 (modified from Iwaki et al. 2005). Role of Bruton's tyrosine kinase (BTK) in the high-affinity IgE receptor (FcεRI)-mediated mast cell degranulation and cytokine production.

Because of that, BTK-deficient mice exhibit impaired mast cell degranulation after FcεRI cross-linking (Setoguchi et al. 1998) and ibrutinib is known to be capable of inhibiting mast cell or basophil degranulation (Chang et al. 2011). Based on this property, Dr. Laura Soucek treated insulinoma-bearing *pIns-c-MycER^{TAM};RIP-Bcl-X$_L$* mice with ibrutinib (Soucek et al. 2011) to impair mast cell function. Upon treatment, mast cells were still recruited to the tumor stroma, but their degranulation was efficiently blocked. Ibrutinib triggered a dramatic regression of tumors (figure 8) without causing any discernible adverse impact on overall health of the mice, suggesting that mast cell inhibition is a practical strategy for the treatment of insulinoma, and potentially other neoplastic diseases (Soucek et al. 2011).

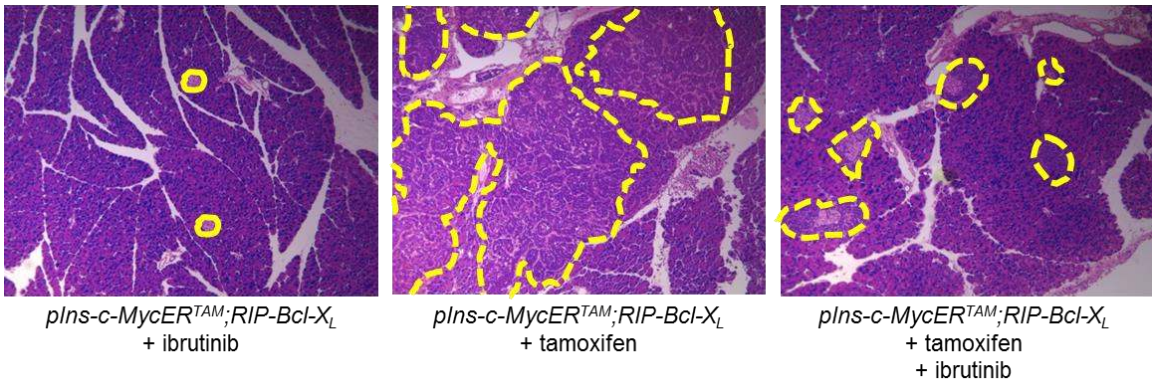

Figure 8 (modified from Soucek et al. 2011). Ibrtinib treatment causes tumor regression in insulinoma-bearing *pIns-c-MycER^{TAM};RIP-Bcl-X$_L$* mice. Vehicle (left panel) or tamoxifen (middle and right panels) was administered daily by intraperitoneal injections for 6 weeks to induce tumor formation. After two weeks of tamoxifen, ibrutinib alone (left and right panels) or vehicle (middle panel) was administered in the drinking water of the mice for 4 weeks. Pancreatic islets are circled in yellow.

Insulinomas are rare, mostly benign, and resectable at the time of diagnosis, so patients suffering from the disease have generally good prognoses. On the other hand, PDAC is much more common, aggressive, generally non-resectable, and non-responsive to therapy. Therefore, new therapies are urgently needed to boost the arsenal against this malignancy. Interestingly, analysis of human PDAC samples reported that mast cell infiltration correlated with higher tumor grade and worse survival (Strouch et al. 2010), and high mast cell numbers at the intratumoral border correlated with the presence of lymphatic and microvascular invasion, as well as with lymph node metastasis (Cai et al. 2011). Additionally, an influx of mast cells was observed in a mouse model of pancreatic cancer expressing high levels of Kras^{G12V} and, importantly, pancreatic tumors orthotopically transplanted in mast cell deficient mice grew more slowly than in control mice, conferring a survival advantage compared to tumors grown in mast cell proficient animals (Chang et al. 2011). Finally, pancreatic cancer cells and cancer associated fibroblast (CAFs) were found to promote mast cell activation, which in turn induce CAF proliferation, promoting tumor growth and preventing efficient delivery of chemotherapeutic agents (Ma et al. 2013). For these reasons, we sought to investigate the potential therapeutic impact of ibrutinib in pre-clinical models of PDAC.

3.4 Myc and metastasis

Metastasis is a multistep process involving both invasion and migration in which cancer cells acquire a combination of epigenetic and genetic changes that modify their behavior and their interactions with the microenvironment. It begins with epithelial cells

acquiring mesenchymal characteristics in a process called epithelial-to-mesenchymal transition (EMT), which allows them to migrate away from the primary tumor site. Migration is followed by invasion through the basement membrane and intravasation into the vasculature (blood circulation or the lymphatic system), where surviving cells extravasate into a distant organ establishing a secondary tumor (Vargo-Gogola and Rosen 2007). Stephen Paget hypothesized that tumor cells (the “seed”) grew preferentially in the microenvironment of select organs (the “soil”), and that metastases resulted only when the appropriate seed was implanted in its suitable soil (Paget 1989). This “seed and soil” hypothesis has been exhaustively confirmed. Indeed, metastases occur preferentially in a few target organs where a “pre-metastatic niche” has been established, namely lymph nodes, bone, brain, liver and lungs. Non-malignant cells present in the tumor microenvironment, particularly the myeloid lineage derived from the bone marrow, are involved in every step of the metastatic cascade and are recruited by cancer cells to enhance their survival, growth, invasion and dissemination (Psaila et al. 2006; Joyce and Pollard 2009; Langley and Fidler 2011). It is suggested that the formation of distant metastases may be due to the presence of cells within the primary tumor that have the ability to form metastases very early in the disease process (Russo et al. 2008). Circulating tumor cells (CTCs) are detected very early during cancer progression and tumor cells can be maintained in a quiescent form in secondary organs for decades until they proliferate again giving rise to metastases, a state known as cancer dormancy (Joosse et al. 2015).

Myc is implicated in most hallmarks of cancer, and metastasis is not an exception. Deregulation of this oncoprotein is a common feature of both high-grade premalignancy and invasive tumors and is associated with poor outcome in a variety of tumor types (Bourhis et al. 1990; Borg et al. 1992; Kozma et al. 1994; Alves Rde et al. 2014; He et al. 2014). Myc drives multiple aspects of tumor progression and metastasis by controlling the transcription of genes promoting cell proliferation and survival, genetic instability, differentiation block, chromatin remodeling, cell invasion and migration (Wolfer and Ramaswamy 2011; Whitfield and Soucek 2012). Cell proliferation, survival and genetic instability result in a higher likelihood of acquiring further mutations, contributing indirectly to the acquisition of a metastatic phenotype. Furthermore, Myc controls cellular migration and invasion directly by regulating specific downstream programs. It coordinates EMT by repressing E-cadherin, a key metastasis suppressor (Cowling and Cole 2007), and promoting the expression of Snail, RhoA and other EMT inducers (figure 9). Importantly, Myc also promotes cellular migration, invasion and metastasis *in vivo* through EMT-independent mechanisms (Wolfer and Ramaswamy 2011). In addition, Myc maintains the tumor microenvironment by instructing tissue

remodeling, angiogenesis and inflammation, even when it is not overexpressed (Sodir et al. 2011), and controls the activation of tumor-associated macrophages which increase cancer's metastatic potential (Joyce and Pollard 2009). Although necessary for the metastatic behavior of cancer cells, Myc deregulation alone seems to be insufficient. Cooperation with other genes, particularly the Ras pathway, promotes metastatic progression at early and late phases of tumorigenesis (Podsypanina et al. 2008).

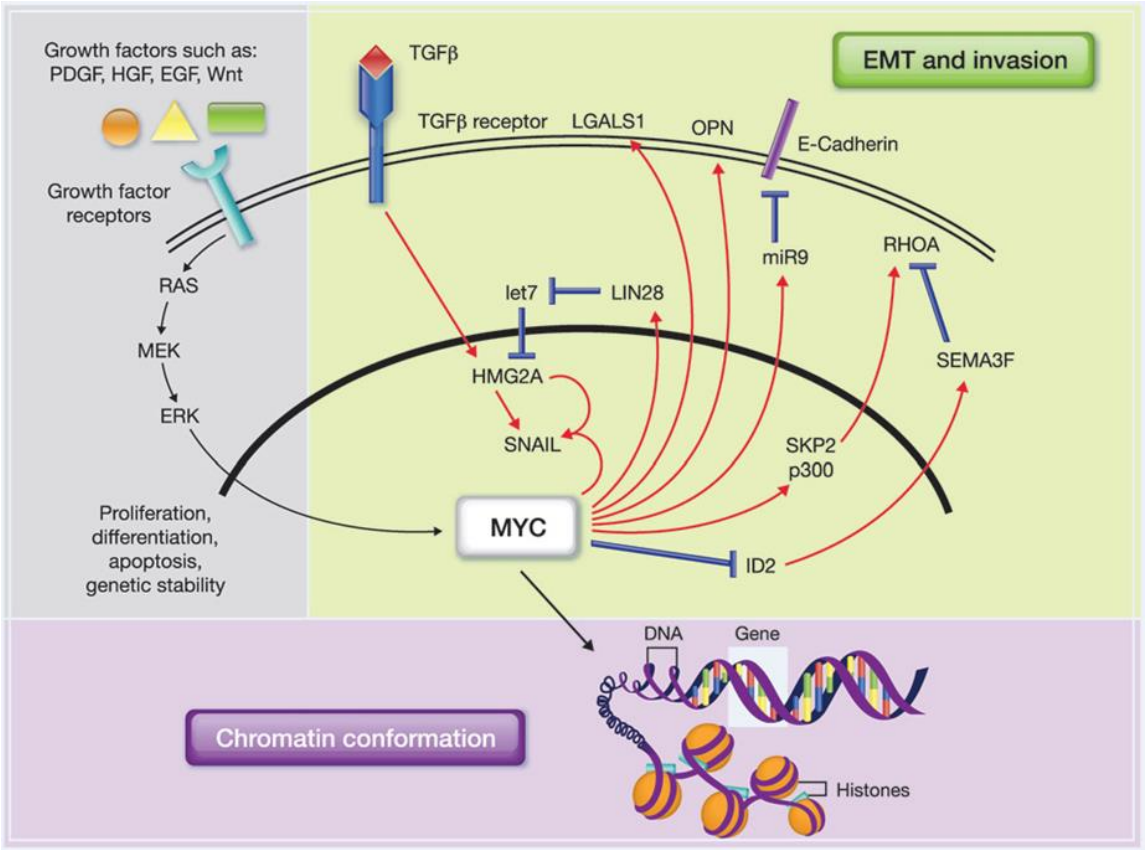

Figure 9 (Wolfer and Ramaswamy 2011). Myc regulates multiple aspects of metastasis. Its role in proliferation, differentiation, survival and genetic stability can indirectly promote and sustain metastasis (grey box). It directly regulates genes involved in cell migration, invasion, and epithelial-to-mesenchymal transition (EMT) (yellow box). Finally, Myc's control of chromatin conformation may set a "metastasis-enabling" epigenetic landscape (purple box).

3.4.1 Myc and metastatic breast cancer

Myc deregulation is a common event in breast cancer. Gene amplification has been found in about 15% of breast tumors, whereas 22-35% present overexpression at the mRNA level and 42-45% at the protein level (Xu et al. 2010). Regarding intrinsic molecular subtypes, Myc is disproportionately elevated in TNBC compared to ER, PR

and HER2+ breast tumors (Horiuchi et al. 2012) and it has been associated with BRCA1 deficiency (Ren et al. 2013). Amplification and overexpression of Myc is frequent in high grade and invasive breast cancers and is consistently correlated with poor outcome and early recurrence in multiple studies (Robanus-Maandag et al. 2003; Aulmann et al. 2006; Corzo et al. 2006; Ben-Porath et al. 2008; Wolfer and Ramaswamy 2011; Nair et al. 2014; Gogas et al. 2016). It is associated with resistance to chemotherapy and endocrine therapy (Pereira et al. 2013; Green et al. 2016) and, importantly, it is more commonly amplified in acquired metastases than in the corresponding primary tumor (Singhi et al. 2012). Despite some existing controversy regarding the role of Myc in breast cancer metastasis (Cappellen et al. 2007), most mechanistic studies point at Myc as an inducer of the metastatic phenotype in breast cancer models (Smith et al. 2009; Chan et al. 2010; Yeh et al. 2011; Kong et al. 2014). One particular study shed light into the subject: Myc was found to coordinately regulate the expression of 13 different “poor-outcome” cancer signatures in breast cancer cells, and its inactivation in breast cancer models inhibited their invasive behavior *in vitro* and the formation of distant metastasis *in vivo*, independently of its effects on proliferation and survival (Wolfer et al. 2010). All these findings combined underscore the importance of Myc as a target in breast cancer, especially in the metastatic setting.

3.5 Myc inhibition

Myc is an ideal target candidate for cancer therapy. It is deregulated in most – perhaps all – human cancers and functions as an integrator of upstream signals, controlling most of the hallmarks of cancer by directly and indirectly regulating the expression of thousands of genes. Nevertheless, no Myc inhibitor has reached the clinic yet, partly due to fear of causing catastrophic side effects in normal tissues and also due to the technical challenge of targeting a nuclear protein that displays a predominantly intrinsically disordered structure and that lacks a binding pocket (Whitfield et al. 2017). Strategies to inhibit Myc include direct inhibition of its expression (G-quadruplex stabilizers, antisense oligonucleotides, siRNA/miRNA), interference with protein/protein interactions or with binding to DNA, indirect inhibition (Bromodomain and extra-terminal domain (BET) inhibitors), indirect targeting by synthetic lethality and indirect targeting by immunotherapy (Prochownik and Vogt 2010; Posternak and Cole 2016; Shalaby and Grotzer 2016; Whitfield et al. 2017). Many have shown great success in preclinical models and some are in clinical trials, but unfortunately none has reached clinical practice.

3.5.1 Omomyc

Omomyc is a dominant negative mutant of Myc designed by Dr. Laura Soucek (Soucek et al. 1998). It comprises the B-HLH-LZ domain of Myc and harbors 4 aminoacidic substitutions in the leucine zipper (E57T, E64I, R70Q, and R71N) that alter its dimerization properties. While Myc cannot homodimerize and it only heterodimerizes with Max, Omomyc is able to form homodimers and heterodimers with both Myc (c-Myc, N-Myc, L-Myc) and Max (Soucek et al. 1998; Savino et al. 2011; Fiorentino et al. 2016). Omomyc/Myc dimers have a very low affinity for DNA, while Omomyc/Omomyc and Omomyc/Max dimers bind to E-boxes. Since neither Omomyc nor Max have a transactivation domain, Myc-dependent transactivation is inhibited in the presence of Omomyc (figure 10).

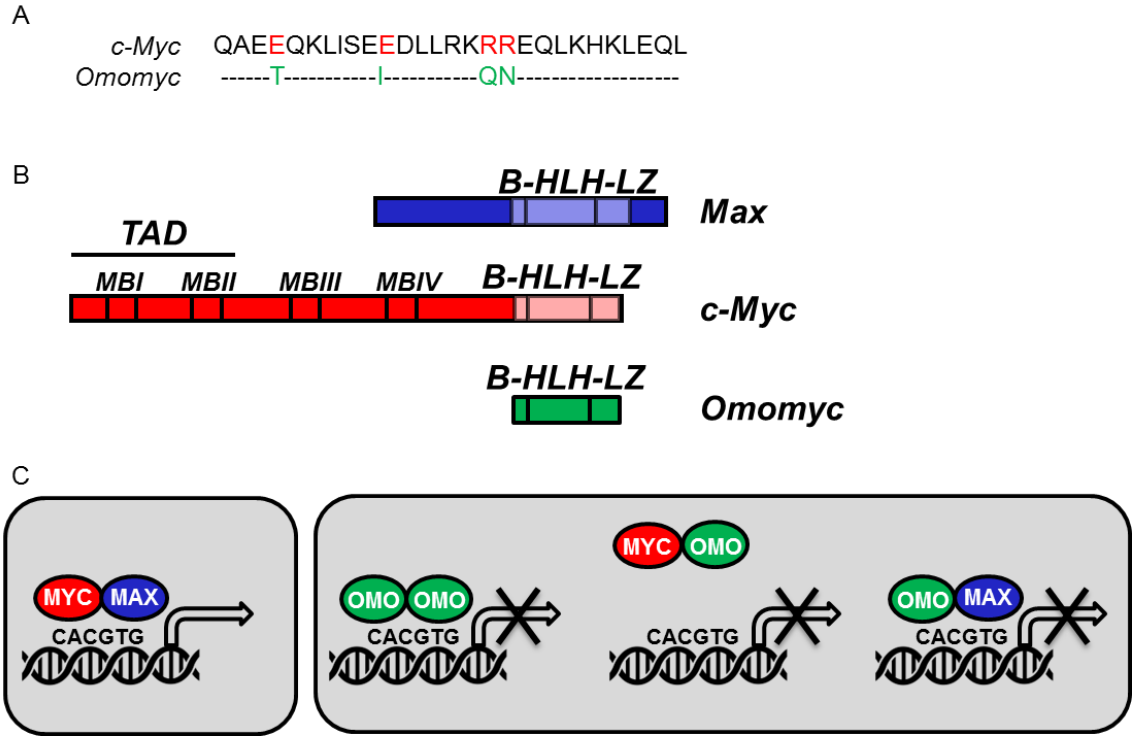

Figure 10. Omomyc acts as a dominant negative of Myc. A) Comparison between the sequence of c-Myc and Omomyc's leucine zipper showing the four mutated amino acids in Omomyc. B) Schematic representation of Max, c-Myc and Omomyc. C) In normal conditions, Myc heterodimerizes with Max and together bind E-box sequences in the DNA were Myc induces transcription of its target genes (left panel). When Omomyc is present, it forms homodimers occupying E-boxes, it heterodimerizes with Myc sequestering it away from DNA and it heterodimerizes with Max occupying E-boxes, resulting in inhibition of transcription of Myc targets (right panel). B-HLH-LZ: Basic helix-loop-helix leucine zipper. TAD: transactivation domain. MBI-IV: Myc boxes I-IV.

Omomyc also binds to Miz-1, but does not bind Mad. Owing to these properties, it has been proposed that Omomyc does not ablate all Myc functions. In fact, Omomyc impedes E-box dependent transactivation of Myc targets, but it could enhance Myc's transprepressive arm, which is E-box independent. This attribute could explain the fact that Omomyc, despite decreasing cell proliferation, promotes apoptosis (Soucek et al. 2002; Savino et al. 2011). In addition, Omomyc causes a decrease in Myc binding that is not uniform for all promoters. It has been recently proposed that Omomyc has little influence on Myc binding at promoters that are highly occupied by physiologic levels of Myc, but it interferes with Myc binding to promoters invaded by supra-physiologic (oncogenic) levels (figure 11) (Jung et al. 2017).

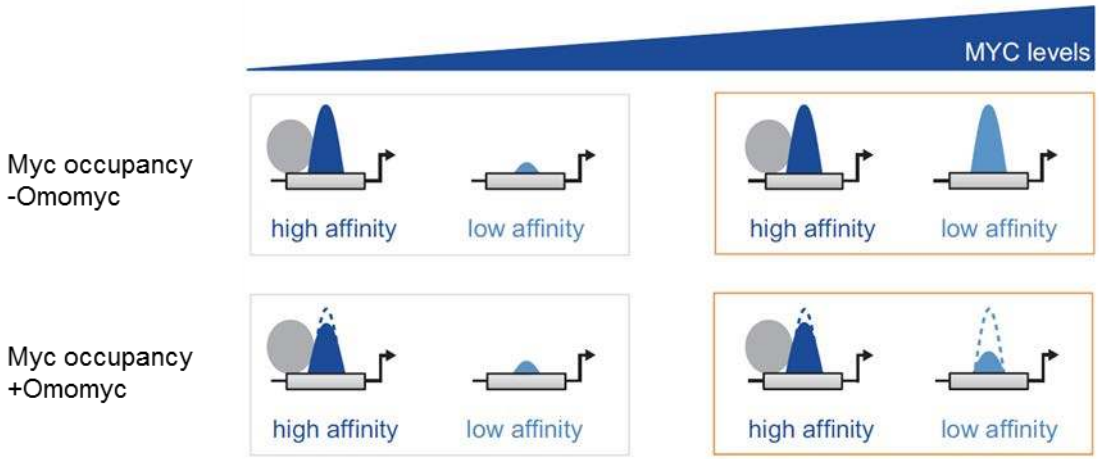

Figure 11 (modified from Jung et al. 2017). Model proposing how Omomyc binds chromatin and regulates expression of Myc target genes. Binding of Myc/Max to promoters that are highly occupied by physiologic Myc levels would be stabilized by protein/protein interactions involving the Myc amino-terminus and would not be outcompeted by Omomyc. As a result, competition by Omomyc would not be uniform and would be more effective on 'low affinity' promoters that are invaded by oncogenic Myc levels.

Using an inducible expression system to control Omomyc transcription, we demonstrated that Myc inhibition is a very potent cancer therapy in various mouse models, regardless of their driving lesion or affected tissue. More in detail, we showed that Omomyc has a dramatic therapeutic impact in a Myc-driven papilloma model (Soucek et al. 2004), in $Kras^{G12D}$-driven lung cancer with and without p53 activity (Soucek et al. 2008; Soucek et al. 2013) (figure 12A), in simian virus 40 (SV40) T antigen-driven pancreatic insulinoma (Sodir et al. 2011) and in glioma, using both V^{12}Ha-Ras-driven transgenic mice and PDX models (Annibali et al. 2014). Importantly and against any expectation, systemic Omomyc expression caused only mild, well-tolerated and reversible side effects in normal tissues (Soucek et al. 2008). This unique feature, combined with the fact that no emergence of resistance was ever observed, makes Myc inhibition by Omomyc a viable strategy even for long-term treatments

(Soucek et al. 2013; Annibali et al. 2014) (figure 12B), offering a significant alternative to the severe side effects and high rate of recurrence caused by current therapies.

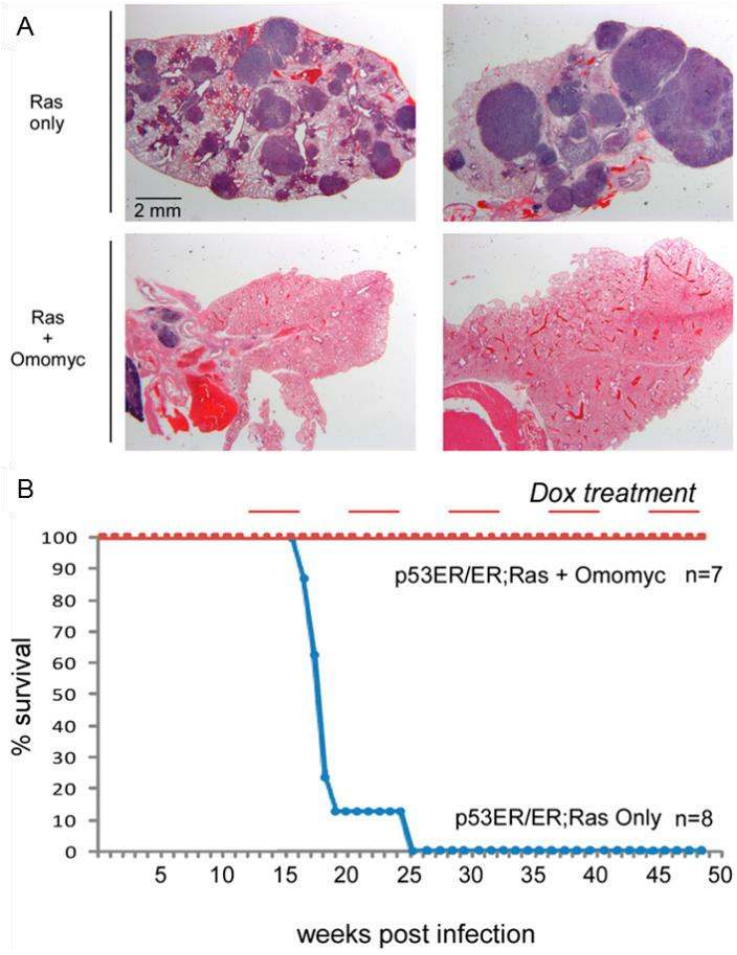

Figure 12 (Soucek et al. 2013). Myc inhibition by Omomyc triggers lung tumor regression in p53-deficient, Kras mutated mice. *$p53^{ER/ER}$;$LSLKras^{G12D}$;TRE-Omomyc;CMV-rtTA* transgenic mice were infected with adenovirus containing a Cre recombinase to induce expression of $Kras^{G12D}$ in the lung epithelium. After 15 weeks, they were treated with doxycycline in their drinking water to induce expression of Omomyc. A) Hematoxylin and eosin staining of lung tissue samples from mice at treatment onset (top panels) and after 4 weeks of doxycycline (bottom panels). B) Survival curve of vehicle-treated mice (blue line) versus counterparts subjected to repeated 4-week periods of doxycycline treatment (red line).

Furthermore, *in vitro*, Omomyc expression causes growth arrest and induction of apoptosis in small cell lung cancer (SCLC) cell lines overexpressing any form of Myc (c-Myc, N-Myc and L-Myc) (Fiorentino et al. 2016) and reverts the stem-like and angiogenic phenotype of glioblastoma cells (Galardi et al. 2016).

In all these studies, Omomyc has been employed with great success against primary tumors of different types, but its effects on the prevention, control or even reversion of metastatic disease remain unknown. Breast cancer patients are in need of improved therapies and Myc has been shown to play a major role in disease progression. Therefore, we asked whether Omomyc would be effective against metastatic breast cancer and made use of multiple models of the disease to investigate the impact of Myc inhibition against this disease.

HYPOTHESIS & OBJECTIVES

1 HYPOTHESIS 1

Mast cell blockade by ibrutinib is a useful therapeutic strategy against PDAC.

To test this hypothesis, the following objectives were established:

- Investigate the role of mast cells in PDAC maintenance by employing ibrutinib to block their degranulation.
- Characterize the effects of ibrutinib in PDAC tumors and their microenvironment.
- Validate the use of ibrutinib as a therapy against PDAC, alone or in combination with the standard of care.

2 HYPOTHESIS 2

The metastatic process is dependent on Myc and inhibiting it will be effective in both prevention and treatment of metastasis.

To test this hypothesis, the following objectives were established:

- Characterize the effect of Omomyc expression in cell lines representative of all intrinsic molecular subtypes of breast cancer.
- Study the impact of Omomyc expression in the metastatic phenotype of highly invasive breast cancer cells by measuring migration, invasion and angiogenesis *in vitro*.
- Confirm the findings obtained in the previous objectives *in vivo* by expressing Omomyc in mouse models of metastatic breast cancer.
- Validate the effect of the Omomyc peptide as a pharmacological approach against metastatic breast cancer.

MATERIALS & METHODS

1 PART 1

1.1 Cell quantification assay

Four PDAC (MIA PaCa-2, YAPC, PSN-1 and PA-TU-8988T) and two NSCLC (PC9 and H292) cell lines were seeded at the optimal density to assure growth during the whole experiment and ibrutinib was added 24 hours later at 9 different concentrations ranging from 0.004 to 1.024 μM. Cells were fixed with 4% formaldehyde and stained after 72 hours using SYTO® 60 Red fluorescent Nucleic Acid Stain (Life Technologies) and fluorescence at 678 nm was measured with a spectrophotometer.

1.2 Immunohistochemistry and staining

Tissue samples were fixed overnight in neutral pH–buffered formalin, embedded in paraffin and sectioned (5 μm). Sections were then de-paraffinized and rehydrated
For immunohistochemistry (IHC), sections were microwaved for 1 min in 0.01 M citrate buffer (pH 6.0) for antigen retrieval. Primary antibodies: rat monoclonal anti–CD11b (clone M1/70, eBioscience), rabbit polyclonal anti-Cd11b (Novus Biologicals), rat monoclonal anti-F4/80 (clone CI:A3-1, Neomarkers), rabbit monoclonal anti-Ki67 (clone SP6, Neomarkers) were applied for 2 h in blocking buffer (2.5% Bovine serum albumin (BSA), 5% goat serum and 0.3% Triton X-100 in phosphate buffered saline (PBS)), followed by Vectastain ABC kit and DAB reagents (Vector Laboratories).
Mast cells were stained by using 1% toluidine blue dissolved in ethanol.
Picrosirius Red stain kit (Polysciences, Inc.) was used to stain for collagen types I and III according to manufacturer instructions.
Images were obtained with an Axiovert S100 TV inverted fluorescence microscope (Zeiss) and Open Lab 3.5.1 software, with an Axiovert 100 inverted microscope (Zeiss) equipped with a Hamamatsu Orca digital camera or with an Olympus FSX100 microscope and FSX-BSW software.

1.3 Flow cytometry

Following resection, PDAC tumors isolated from PBS-perfused mice were immediately placed in ice-cold PBS, followed by manual mincing using scissors and a 20-min

enzymatic digestion with 1.25 mg/ml collagenase type IV (Roche), 0.1% trypsin inhibitor, and 50 U/ml DNase I (Roche) in serum-free Dulbecco's Modified Eagle's Medium (DMEM) (Life Technologies) at 37ºC with continuous stirring. Single cell suspensions were then prepared by passing tissue through 70 μm nylon strainers (BD Biosciences). Cells were incubated for 30 min at 4ºC with rat anti-mouse CD16/CD32 mAb (1:250, clone 2.4G2, BD Bioscience) in PBS, which also contained Live/Dead Aqua stain (1:250, Life Technologies) to differentiate between viable and dead cells. Cells were then incubated for 30 min in PBS containing 1% BSA (Sigma) and 2 mM ethylenediaminetetraacetic acid (EDTA) with 100 µl of fluorophore-conjugated anti-mouse antibodies (dilution; clone): PE-Cy7-CD45 (1:800; 30-F11), PerCp-Cy5.5-CD3e (1:400; 145-2C11), PerCp-Cy5.5-CD19 (1:200; 6D5), PerCp-Cy5.5-CD49b (1:400; DX5), Alexa 700-CD11b (1:400; M1/70), APC780-CD11c (1:200; N418), eFluor450-MHCII (1:800; M5/114.15.2), APC-Ly6C (1:800; HK1.4), PE-Ly6G (1:400; 1A8), and PE-Cy5-F4/80 (1:400; BM8) (eBioscience or Biolegend). Cells were then washed once in PBS containing 1% BSA and 2 mM EDTA, followed by fixation with BD Cytofix for 30 min on ice. After a final wash, cells were stored at 4ºC until data acquisition using a LSRII flow cytometer and LSRII FACSDiva software (BD Biosciences). Analysis was performed using FlowJo software (Tree Star Inc).

1.4 Animal studies

All the animal studies were performed in accordance with the ARRIVE guidelines and the 3 Rs rule of Replacement, Reduction and Refinement principles.
Mice were housed and treated following the protocols approved by the Institutional Animal Care and Use Committee (IACUC) at the University of California, San Francisco (UCSF) and by the CEEA (Ethical Committee for the Use of Experimental Animals) at the Vall d'Hebron Research Institute (VHIR), Barcelona. Mouse weights were recorded for every experiment.

1.4.1 Transgenic mice

LSLKras^{G12D};Pdx1-Cre [Kras^{tm4Tyj}; Tg(Ipf1-Cre)1Tuv] and *p53$^{ER/ER}$* [Trp53^{tm1Gev}] mice have been previously described (Jackson et al. 2001; Hingorani et al. 2003; Christophorou et al. 2005). For all experiments, 8 week old male and female *p53$^{ER/ER}$;LSLKras^{G12D};Pdx1-Cre* mice of mixed C57BL/6-FVB/N background were

randomized into two groups: treated and control. Ibrutinib (0.16 mg/ml with 1% 2-Hydroxypropyl-beta-cyclodextrin (HP-β-CD)) was added to the drinking water of treated animals, and control animals received water containing vehicle only (1% HP-β-CD). Vehicle or ibrutinib dissolved in water were both consumed at approximately 5.5 mL per day, in accordance with the reported typical daily water intake (Bachmanov et al. 2002). Gemcitabine (75 mg/kg) was injected intraperitoneally twice a week for 3 weeks followed by a 1-week rest period. Sodium cromoglycate (10 mg/kg) was dissolved in saline solution and injected intraperitoneally, and control mice were treated with vehicle only. Endpoint criteria were defined as 20% body weight loss in addition to general morbidity and lethargy caused by tumor burden. Mice euthanized due to intestinal metaplasia or mucocutaneous papillomas caused by extrapancreatic $Kras^{G12D}$ expression were excluded from the survival study.

1.4.2 Subcutaneous patient-derived xenografts (PDXs)

The anonymized human sample employed was part of the tissue biological material of the University Hospital Vall d'Hebron (HUVH). The sample had been collected with a signed patient consent form and its use had been approved by the Clinical Research Ethics Committee (CEIC). The sample was randomly selected among the patient samples available. Heterotopic xenografts were generated from a tumor biopsy of a patient that underwent pancreatectomy at HUVH: when routine pathological gross examination of a resected pancreas led to the detection of an adenocarcinoma, a slice with a thickness of 1-2 mm was transferred to RPMI 1640 media containing Antibiotic-Antimycotic (Gibco) and kept on ice; within approximately 30 min the tissue sample was cut into pieces of 15 mm^3 under sterile conditions, suspended in Matrigel (BD Biosciences) and transported to the specific pathogen free (SPF) area of the animal facility. A tumor piece was implanted subcutaneously into the flank of 2-3 female 6 week old NOD/SCID mice (Charles River Laboratory). When successfully grafted tumors reached a size of about 750 mm^3 they were transplanted. The xenograft used for the study described here was transplanted to 6 week old NOD/SCID females in generation 4, which after 6 weeks had produced a cohort of 28 mice with tumors measurable by caliper. Animals were randomized into 2 groups, 1 treated with ibrutinib (0.16 mg/ml added to the drinking water) and the other untreated. Tumor size was evaluated weekly by caliper measurements and tumor volume calculated using the following formula: volume = $(\text{length} \times \text{width})^2 / 2$. When tumor volume reached 1500

mm^3 animals were euthanized and the tumor was collected and fixed overnight in neutral pH–buffered formalin.

1.4.3 Orthotopic cell implantation

MIA PaCa-2 cells were infected with the pLEX lentiviral vector (Open Biosystems) containing a firefly luciferase (Fluc) cassette expressed constitutively. Viruses were produced in HEK293T cells with the Trans-Lenti Packaging kit from Open Biosystems. Virus-containing supernatants were filtered with 0.45 µm PVDF filters (Millipore) and transduced cells were selected with 0.8 µg/ml puromycin.

A suspension of 900,000 MIA PaCa-2 Fluc cells mixed with Matrigel (1:1) were injected in the pancreas of 40 7 week old BALB/c nude female mice (Charles River Laboratory) previously anesthetized by an intraperitoneal injection of a ketamine/xylazine mix (80 mg/kg ketamine, 10 mg/kg xylazine). Tumor growth was followed weekly by IVIS imaging. Briefly, mice were injected intraperitoneally with a D-luciferin solution (150 mg/kg in PBS) 5-10 minutes prior to acquisition. They were anesthetized with isoflurane (5% for induction and 2% during acquisition) and air flow was set at 0.8 L/min. Acquisition and data analysis were carried out by the Preclinical Imaging Platform staff at VHIR with the Xenogen IVIS Spectrum equipment and Living Image® software (Perkin Elmer). One week after surgery, mice were randomized into four groups and treated with vehicle, ibrutinib (0.16 mg/ml added to the drinking water), gemcitabine (75 mg/kg) and gemcitabine + ibrutinib. After 5 weeks of treatment, mice were euthanized and their pancreata resected for a final *ex vivo* bioluminescence imaging acquisition. Pancreata were fixed overnight in neutral pH–buffered formalin.

1.5 Statistics

Statistical analysis and representation of the data was performed using GraphPad Prism 6. For histograms, mean + standard deviation (SD) is shown. For scattered dot blots, mean ± SD is shown. For X-Y graphs, mean ± standard error of the mean (SEM) is shown to help visualization of the data. When the number of biological replicates (n) < 8, parametric tests were used. When n ≥ 8, a d'Agostino-Pearson omnibus normality test was used. If the test confirmed a Gaussian distribution of the data, a parametric test was used. Otherwise, non-parametric tests were used.

To determine statistical significance among two groups, a two-tailed unpaired T test (parametric) or a two-tailed Mann-Whitney test (non-parametric) was used. Chi-square test of homogeneity was used when comparing the degree of collagen staining in pancreatic tumors and Log-Rank test was used for Kaplan-Meier survival curves. When comparing four groups, one-way ANOVA was used for the analysis of variance, and the statistical difference between groups was determined via Dunnett's (when comparing the mean of a control group with the mean of the other groups) or Tukey's (when comparing the mean of all groups) multiple comparisons test. For all tests, an alpha level of 0.05 was established. In all graphs, *, ** and *** are used to describe p values below 0.05, 0.01 and 0.001 respectively, as stated in figure legends. For all histograms, asterisks above one bar indicate statistical significance between that bar and the control group (filled with black). For other graphs, a line between the statistically significant groups is drawn.

2 PART 2

2.1 Cell culture

2.1.1 Cell lines and lentiviral infections

All cell lines were kindly provided by the laboratories of Violeta Serra (Cal51, JIMT-1, MCF7, MDA-MB-361, MDA-MB-453 and T47D), Joaquín Arribas (BT-474, LM2-4175, MDA-MB-231 and SkBr3) and Josep Villanueva (BT-549 and Hs578T). Cal51, Hs578T, JIMT-1 and MCF7 cells were grown in DMEM medium (Life Technologies). BT-474, LM2-4175, MDA-MB-231 and SkBr3 and cells were grown in DMEM/F12 medium (Life Technologies). BT-549 and T47D cells were grown in RPMI medium (Life Technologies). MDA-MB-361 and MDA-MB-453 cells were grown in L-15 medium (Life Technologies). All culture mediums were supplemented with 10% fetal bovine serum (FBS) and 1% glutamine. All cells were grown at 37ºC and 5% CO_2, except MDA-MB-361 and MDA-MB-453 which were grown at 37ºC without CO_2.

MDA-MB-231-derived LM2-4175 TGL cells were described previously (Minn et al. 2005). They contain a triple-fusion protein reporter construct encoding herpes simplex virus thymidine kinase 1, green fluorescent protein (GFP) and firefly luciferase obtained by retroviral infection (Ponomarev et al. 2004).

All cell lines were infected with the pSLIK-hygro lentiviral vector (Addgene) containing a GFP or Omomyc cassette, which were inserted by gateway technology in Gerard Evan's laboratory. For infections, HEK293T cells were seeded at 30% confluence and the following morning 25 mM chloroquine added. Two hours later, HEK293T cells were transfected with pSLIK-Omomyc or pSLIK-GFP plus the lentiviral vectors pMD2G and psPAX2 by the $CaPO_4$ method. The medium was changed the following day and sodium butyrate added at 5 mM. Viral supernatants were harvested on the subsequent 2 days, filtered with 0.45 µm PVDF filters (Millipore) and added to target cells with polybrene (0.8 mg/ml). Transduced cells were selected with 1 mg/ml hygromycin.

2.1.2 Clonogenic assays

500 cells/well were plated in 6 well plates in the presence or absence of 0.6 µg/ml doxycycline. Cells were fixed with 4% formaldehyde between 2 and 7 weeks later, depending on the doubling time of each cell line. After 20 minutes of fixation, colonies

were stained with 0.05% crystal violet for 1 hour and the plates washed with distilled water and air-dried. The bottom of the plate was scanned in high resolution and the images obtained were analyzed with the ColonyArea plugin (Guzman et al. 2014) for ImageJ software (Schneider et al. 2012) to determine, for each well, the area percentage occupied with cells and the intensity of the staining, as described previously (Guzman et al. 2014).

2.1.3 Western blots

For western blots, cells were cultured in the presence or absence of 0.6 µg/ml doxycycline for 3 days. Then, culture media was discarded and cells were placed on ice. PBS + 1 mM EDTA was added to the plate and cells were scraped, centrifuged and washed twice. Cell pellets were frozen and kept at -80ºC.

Cells were lysed with RIPA buffer supplemented with protease and phosphatase inhibitors (Roche) and the protein fraction collected. Proteins were quantified by the DC™ Protein Assay (Bio-Rad) and absorbance at 560 nm was measured with the Victor3 spectrophotometer (PerkinElmer). 15-30 µg of protein extract in Laemmli buffer +15% β-mercaptoethanol were run on 10% or 12% precast gels (Life Technologies). Proteins were transferred to PVDF membranes by the iBlot® 2 Dry Blotting System (Life Technologies) and membranes were stained with Ponceau red. After washing with PBS + 0.1% Tween and blocking with 2% milk, membranes were incubated overnight at 4ºC with the following primary antibodies: mouse monoclonal anti-c-Myc (9E10) (Santa Cruz Biotechnology, 1:500), mouse monoclonal anti-RNA polymerase III (H-9) (Santa Cruz Biotechnology, 1:50), mouse monoclonal anti-β-actin (AC-15) (Sigma, 1:50,000) or rabbit polyclonal anti-Omomyc (affinity purified and selected against recognition of the MYC b-HLH-LZ epitope, 1:12,000). Membranes were washed with PBS-tween and incubated for 1 hour at room temperature with the following secondary antibodies: ECL™ anti-rabbit IgG-HRP and ECL™ anti-mouse IgG-HRP (GE Healthcare 1:5,000). Membranes were washed twice with PBS-tween and once with PBS, and then incubated for 5 minutes with SuperSignal™ West Pico Chemiluminescent Substrate (Thermo Fisher Scientific) before revealing. To quantify the Omomyc levels expressed in each cell line, the intensity of the Omomyc and β-actin bands was quantified with ImageJ and a ratio Omomyc/β-actin established. This ratio was then correlated with the relative cell number obtained in the colony formation assays.

2.1.4 Flow cytometry

2.1.4.1 Detection of lentivirally-expressed Omomyc

For the detection of lentivirally-expressed Omomyc, MDA-MB-231 pSLIK Omomyc or LM2-4175 TGL pSLIK Omomyc cells were treated for 3 days with or without 0.6 µ/ml doxycycline, harvested by trypsinization and fixed/permeabilized in absolute ethanol overnight at 4ºC. Cells were washed with PBS-Azide (PBS with 0.1% Sodium Azide and 1% BSA) and blocked with 2.5% BSA in PBS for 30 min at room temperature. Cells were stained with rabbit polyclonal anti-Omomyc antibody (1:50) for 1 hour at room temperature. After washing, cells were incubated with goat anti-rabbit AlexaFluor®647 (1:1,000, Life Technologies) for 45 minutes at room temperature. Navios Flow Cytometer (Beckman Coulter) was used for data acquisition and FlowJo V10 software (Tree Star Inc) was used for data analysis.

2.1.4.2 BrdU incorporation and cell cycle analysis

For bromodeoxyuridine (BrdU) incorporation and cell cycle analysis, MDA-MB-231 pSLIK GFP, MDA-MB-231 pSLIK Omomyc or MDA-MB-231 cells were treated for 3 days with either vehicle, 0.6 µ/ml doxycycline, 20 µM Omomyc cell-penetrating peptide ($Omomyc^{CPP}$) or 20 µM TMTP1-Omomyc, then labeled with 10 µM BrdU for 2h, harvested by trypsinization and fixed/permeabilized in absolute ethanol overnight at 4ºC. After denaturation in 2 M HCl for 30 min at room temperature, they were neutralized with 0.5 M sodium borate and stained with anti-BrdU-FITC antibody (BD Pharmingen, 1:5) diluted in PBS + 0.5% BSA and 0.5% Tween. Cells were incubated in 25 mg/L propidium iodide (PI) + 100 µg/mL RNAse A and 0.3 µM Triton X-100 for 30 minutes. Navios Flow Cytometer (Beckman Coulter) was used for data acquisition and FCS Express 4 software was used for data analysis.

2.1.4.3 $Omomyc^{CPP}$ and TMTP1-Omomyc cell entry

MDA-MB-231 cells were treated with buffer (25 mM NaAc 2 M urea), 0.5 µM, 1 µM, 10 µM or 20 µM $Omomyc^{CPP}$-AlexaFluor 488, or with 0.5 µM TMTP1-Omomyc-AlexaFluor 488 for 15 minutes. Then, they were tryspinized with 0.25% Trypsin-EDTA (Gibco™)

for 30 minutes at 37ºC to remove membrane-bound peptide and trypsin was deactivated with 10% FBS. Cells were washed and resuspended in PBS and immediately analyzed. CytoFlex Flow Cytometer (Beckman Coulter) was used for data acquisition and CytExpert software (Beckman Coulter) was used for data analysis.

2.1.5 Proliferation assays

2.1.5.1 Lentivirally expressed Omomyc

20,000 MDA-MB-231 pSLIK GFP, MDA-MB-231 pSLIK Omomyc or LM2-4175 TGL pSLIK Omomyc cells/well were plated in 6 well plates with or without 0.6 µg/ml doxycycline. After 6 days, cells were either trypsinized or fixed with 4% formaldehyde. Trypsinized cells were counted with the Tali™ Image-based Cytometer (Life Technologies). Fixed cells were stained with 0.05% crystal violet for 1 hour and the plates washed with distilled water, air-dried and scanned.

2.1.5.2 Treatment with Omomyc^{CPP} and TMTP1-Omomyc

For the proliferation assay, 500 MDA-MB-231 cells/well were seeded in a 24 well plate and the next day treated with vehicle (PBS), 5 µM and 20 µM Omomyc^{CPP} or 5 µM and 20 µM TMTP1-Omomyc, in triplicates. The medium was removed 3 times a week and new peptide was added. After 2 weeks, cells were harvested by trpsinization and counted with the Tali™ Image-based Cytometer (Life Technologies).
For the cell death assay, MDA-MB-231 cells were treated with a single dose of vehicle (PBS), 20 µM Omomyc^{CPP} or 20 µM TMTP1-Omomyc and the percentage of trypan blue-positive cells was measured after 6 days with the Vi-CELL™ Cell Counter (Beckman Coulter).

2.1.6 Angiogenesis assay

1 million MDA-MB-231 pSLIK GFP +/- 0.6 µg/ml doxycycline, 1 million MDA-MB-231 pSLIK Omomyc cells without doxycycline and 1.5 million MDA-MB-231 pSLIK Omomyc cells + 0.6 µg/ml doxycycline were plated and their conditioned media collected after 3 days. Cells expressing Omomyc were plated at a higher density so that at the time of

medium collection the number of cells was the same as the non-expressing ones. Conditioned media was centrifuged and filtered with 0.45 µm PVDF filters (Millipore). 75,000 human umbilical vein endothelial cells (HUVEC) were mixed with 300 µl of each conditioned media and 100 µl of the mix containing 25,000 cells was plated per well in a 96 well plate, on top of a Matrigel layer to allow tube formation. After 6 hours, representative images were acquired with an IX71 Olympus inverted microscope. Tube formation was assessed by the Angiogenesis Analyzer plugin for ImageJ (NIH) as described previously (Lee et al. 2014).

2.1.7 Wound healing assay

MDA-MB-231 pSLIK GFP and MDA-MB-231 pSLIK Omomyc cells were plated with or without 0.6 µg/ml doxycycline. After 3 days, cells were trypsinized, counted and 400,000 cells/well were seeded in triplicates in a 12 well plate +/- doxycycline. 7 hours later, when cells were attached and forming a confluent monolayer, a p1000 pipette tip was used to scratch the surface of the well forming a wound. An Olympus CellR microscope equipped with a Hamamatsu C9100 camera was used to follow the closure of the wound. Pictures were taken automatically every 30 minutes and wound area was measured at the endpoint with ImageJ. Cells were then trypsinized, counted with the Tali™ Image-based Cytometer (Life Technologies) and the difference in wound area was corrected for the total number of cells.

2.1.8 Boyden Chamber assays

2.1.8.1 Migration assays

MDA-MB-231 pSLIK GFP, MDA-MB-231 pSLIK Omomyc, BT-549 pSLIK GFP, BT-549 pSLIK Omomyc, Cal51 pSLIK GFP, Cal51 pSLIK Omomyc, MCF7 pSLIK GFP, MCF7 pSLIK Omomyc and LM2-4175 TGL pSLIK Omomyc cells were plated in complete medium (+10% FBS) with our without 0.6 µg/ml doxycycline. After 3 days, cells were washed with PBS and refed with medium containing 0.5% FBS +/- doxycycline and left overnight. Then, cells were counted with the Tali™ Image-based Cytometer (Life Technologies) and 30,000 cells/well were seeded on top of Corning® FluoroBlok™ inserts in a 24 well plate (Figure 13A). The inserts consisted on a chamber with a dark porous membrane (pore diameter: 8 µm). Cells were seeded in triplicates, +/-

doxycycline, in medium containing 0.5% FBS, and the bottom of the well was filled with complete medium +/- doxycycline. After 24 or 48 hours, depending on the migratory capacity of each cell line, migrated cells were stained with the fluorescent CellTracker™ Green CMFDA dye (Life Technologies), fixed with 4% formaldehyde and representative images were taken with an IX71 Olympus inverted microscope (Figure 13B and C). In parallel, 30,000 cells/well were seeded in a 24 well control plate under the same conditions, with the exception of the inserts. After 24 or 48 hours, they were harvested by trypsinization and counted with the Tali™ Image-based Cytometer. Migrated cells from the acquired images were analyzed with Fiji, a distribution of the ImageJ software (Schindelin et al. 2012). First, the original image was converted to binary and the watershed tool was used to discriminate between individual cells that were in aggregates (Figure 13D). Some fluorescent signal from non-migrated cells was visible through the pores of the membrane. To avoid counting those as cells, the area of some migrated cells was measured and compared with the area of the pores, and a threshold was established. Cells above this threshold value were counted with the 3D objects counter analysis tool (Figure 13E). The values of the images from the same condition were averaged, normalized, and corrected for the difference in cell number obtained from the control plate, if any was observed.

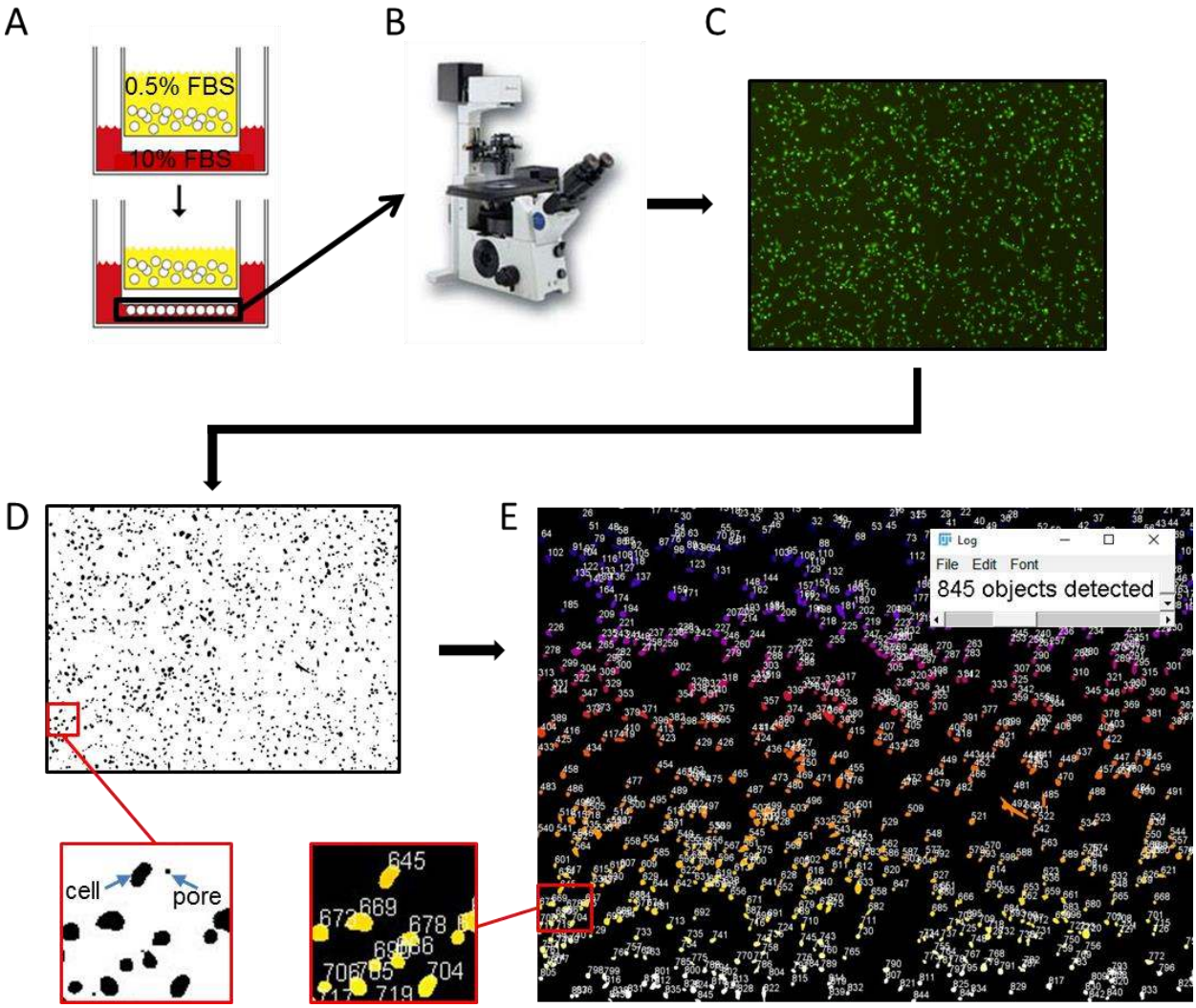

Figure 13. Schematic representation of the migration assay and its quantification.

A. Cells are plated on top of the chamber in medium containing 0.5% FBS. The bottom of the well is filled with medium containing 10% FBS.
B. After migration, cells are stained, fixed and observed under an inverted fluorescence microscope.
C. Representative images of fluorescently-labeled migrated cells are acquired.
D. Fiji Software is used to convert the image to binary. Pores and migrated cells are distinguished by their different area and a threshold in between is established.
E. Objects corresponding to migrated cells are counted automatically with Fiji's 3D object counter tool.

2.1.8.2 Invasion assay

MDA-MB-231 pSLIK GFP, MDA-MB-231 pSLIK Omomyc and LM2-4175 TGL pSLIK Omomyc cells were plated under the same conditions as the migration assay. The only difference was the use of Corning® BioCoat™ Invasion Chambers, in which the porous

membrane is coated with a layer of Matrigel to mimic an extra cellular matrix (ECM). Cells were allowed to invade through the coated membrane for 24 hours and they were fixed, stained and counted as explained for the migration assay (Figure 13). A control plate under the same conditions was also plated, and the differences in invasive capacity of the cells were corrected for the difference in cell number.

2.1.9 Clonal selections and bioluminescence quantification *in vitro*

LM2-4175 TGL pSLIK Omomyc or LM2-4175 TGL pSLIK Omomyc c#11 cells were harvested by trypsinization and a theoretical number of 0.5 cells/well were seeded in a 96 well plate. Wells that contained one single cell were followed over time until it had clonally expanded. The different clonal populations were trypsinized and seeded on a new 96 well plate at a density of 10,000 cells/well. Firefly luciferase activity was measured by the Dual-GLo® Luciferase Assay System following manufacturer's instructions, and luminescence was measured with a Victor3 spectrophotometer (PerkinElmer)

2.1.10 Omomyc^{CPP} cell entry by confocal microscopy

MDA-MB-231 cells were treated with vehicle or 20 μM Omomyc^{CPP}-AlexaFluor 488 for 15 minutes, quickly washed with a solution of 0.2 M acetic acid and 0.2 M NaCl to remove membrane and glass-bound peptide and immediately washed twice with PBS, stained with 10 μg/mL Hoechst 33342 trihydrochloride, trihydrate (Thermo Fisher) for 5 minutes, washed twice with PBS, mounted and analyzed. Confocal microscopy images were captured using a Nikon C2+ confocal microscope and NIS-elements software.

2.1.11 IC50 calculations

5,000 MDA-MB-231 cells/well were seeded in a 24 well plate and the next day treated with a single dose of increasing concentrations of Omomyc^{CPP} and TMTP1-Omomyc (0, 2.34, 4.69, 6.25, 9.38, 12.5, 18.75, 25, 37.5, 50 and 100 μM). After 6 days, alamarBlue® (Thermo Fisher Scientific) was added to the wells and 4 hours later fluorescence at 590 nm was measured with a Spark® microplate reader (Tecan). IC50s were calculated using GraphPad Prism 6.

2.2 Animal studies

All the animal studies were performed in accordance with the ARRIVE guidelines and the 3 Rs rule of Replacement, Reduction and Refinement principles.
Mice were housed and treated following the protocols approved by the CEEA (Ethical Committee for the Use of Experimental Animals) at the Vall d'Hebron Research Institute (VHIR), Barcelona. Mouse weights were recorded for every experiment.

2.2.1 Cell-line derived orthotopic model

A suspension of LM2-4175 TGL pSLIK Omomyc c#11 cells were mixed with Matrigel (1:1) and 1.5 million cells/mouse were injected between the fourth and fifth right mammary fat pads of 33 6 week old BALB/c nude females (Janvier). Before surgery, mice were anesthetized with 2% isoflurane and buprenorphine (0.75 mg/kg) was administered subcutaneously. Tumor size was evaluated three times a week by caliper measurements and tumor volume calculated using the following formula: volume = (length x width)^2 / 2. When tumors reached 100 mm^3, mice were randomized into three groups: doxycycline (n=11), TMTP1-Omomyc (n=11) and vehicle (n=11). The doxycycline group was given 2 g/L doxycycline in 5% sucrose in the drinking water to induce expression of the Omomyc transgene. The TMTP1-Omomyc group received 3 intratumoral injections per week of a 1 mM solution of TMTP1-Omomyc in 50 mM NaAc 150 mM NaCl pH 6.15. The volume administered was adjusted to tumor size according to table 2. The vehicle group was given 5% sucrose in the drinking water and received 3 intratumoral injections per week of 50 mM NaAc 150 mM NaCl pH 6.15. The volume administered was also adjusted to tumor size according to table 2. Doxycycline- and TMTP1-Omomyc-treated mice received intratumoral injections of vehicle and 5% sucrose in the drinking water respectively.

Tumor volume (mm^3)	Volume administered (µL)
100-200	10
200-300	20
300-400	30
400-500	40
>500	50

Table 2. Relationship between tumor volume and the volume of TMTP1-Omomyc (1 mM solution) or vehicle (50 mM NaAc 150 mM NaCl pH 6.15) administered.

Mice were treated for 4 weeks and euthanized by CO_2 inhalation. Tumors were then excised, weighed, fixed for 48h in buffered 4% formaldehyde, transferred to 70% ethanol and embedded in paraffin.

2.2.2 Cell line-derived lung colonization model

2.2.2.1 Omomyc transgene activation

A suspension of 500,000 LM2-4175 TGL pSLIK Omomyc c#11 cells in PBS were inoculated through the lateral tail vein of 20 BALB/c nude female mice (Janvier). Starting the day after inoculation, lung colonization and growth of tumor cells was monitored by IVIS imaging. 10 days after inoculation, mice were randomized into two groups and treated with either 2 g/L doxycycline and 5% sucrose in the drinking water (n=10) or with 5% sucrose only (n=10). 5 weeks later, a final *in vivo* bioluminescence detection was performed. Moreover, µCT scans were performed to allow visualization of individual lung lesions. Mice were euthanized by CO_2 inhalation and their lungs excised, fixed for 48h in buffered 4% formaldehyde, transferred to 70% ethanol and embedded in paraffin.

2.2.2.2 Treatment with TMTP1-Omomyc, alone and in combination with paclitaxel

A suspension of 500,000 LM2-4175 TGL pSLIK Omomyc c#11 cells in PBS were inoculated through the lateral tail vein of 41 BALB/c nude female mice (Janvier). Starting the day after inoculation, lung colonization and growth of tumor cells was monitored by IVIS imaging. 3 weeks after inoculation, when lung tumors were established, mice were randomized into 4 groups and treated with vehicle (n=10), paclitaxel (PTX) (n=10), TMTP1-Omomyc (n=11) or PTX + TMTP1-Omomyc (n=10). PTX was diluted in PBS and administered intraperitoneally twice a week at a dose of 10 mg/kg (200 µL). TMTP1-Omomyc was diluted in 50 mM NaAc 150 mM NaCl pH 6.15 and administered intranasally 4 times a week at a dose of 5 mg/kg (30 µL). Vehicle-treated mice received PBS intraperitoneally and 50 mM NaAc 150 mM NaCl pH 6.15 intranasally. PTX- and TMTP1-Omomyc-treated mice received vehicle intranasally and intraperitoneally respectively. After 4 weeks of treatment, a final *in vivo* bioluminescence detection was performed. Moreover, µCT scans were performed to

allow visualization of individual lung lesions. Mice were euthanized by CO_2 inhalation and their lungs excised, fixed for 48h in buffered 4% formaldehyde, transferred to 70% ethanol and embedded in paraffin.

2.2.3 Cell line-derived orthotopic model with surgical resection and metastatic spread

A suspension of LM2-4175 TGL pSLIK Omomyc c#11 cells were mixed with Matrigel (1:1) and 1.5 million cells/mouse were injected between the fourth and fifth right mammary fat pads of 50 6 week old BALB/c nude females (Janvier). Before surgery, mice were anesthetized by an intraperitoneal injection of a ketamine/xylazine mix (80 mg/kg ketamine, 10 mg/kg xylazine). Tumor size was evaluated weekly by caliper measurements and tumor volume calculated using the following formula: volume = $(\text{length} \times \text{width})^2 / 2$. Tumors were also followed by weekly IVIS imaging. Between 8 and 10 weeks after inoculation, primary tumors were surgically resected. After resection, 12 mice presented metastases and none of the 38 mice left developed metastases during the following 12 weeks. Metastasis-bearing mice were randomized into two groups and treated with either 2 g/L doxycycline and 5% sucrose in the drinking water (n=6) or with 5% sucrose only (n=6). The evolution of metastases was followed weekly by IVIS imaging and mice were treated for a maximum of 12 weeks. Two control mice from the sucrose-treated group had to be euthanized 3 and 6 weeks after treatment onset due to metastatic burden. Mice were euthanized by CO_2 inhalation and an *ex vivo* IVIS scan was performed. Organs that were positive for luciferase activity were collected, fixed for 48h in buffered 4% formaldehyde, transferred to 70% ethanol and embedded in paraffin.

2.2.4 IVIS and µCT imaging

IVIS studies were performed with a Xenogen IVIS Spectrum (Perkin Elmer) and micro-computed tomography (µCT) studies were performed with a Quantum GX microCT Imaging System (Perkin Elmer). Acquisition and analysis were carried out by the Preclinical Imaging Platform staff at VHIR.

For IVIS imaging, mice were injected intraperitoneally with a D-luciferin solution (150 mg/kg in PBS) 5-10 minutes prior to acquisition. For both IVIS and µCT, mice were

anesthetized with isoflurane (5% for induction and 2% during acquisition). Air flow was set at 0.8L/min.

IVIS data were analyzed with Living Image® software (Perkin Elmer). Study analysis consists in a light radiance quantification. Signals from the light sources were detected and characterized. Working units were photons/sec/cm/strd, which allow comparison between images obtained by different acquisition parameters.

µCT reconstructions were performed with the Quantum GX microCT software and AMIDE software was used for the analysis (http://amide.sourceforge.net).

2.2.5 Transgenic mice

TRE-Omomyc;CMV-rtTA (C57BL/6-FVB/N mixed background) mice were described previously (Soucek et al. 2008; Soucek et al. 2013; Annibali et al. 2014). Mice were imported from University of California San Francisco (UCSF) and rederived through embryonic transference into pathogen-free foster mothers to comply with VHIR's housing requirements.

TRE-Omomyc;βactin-rtTA (FVB/N pure background) mice were described previously (Soucek et al. 2008; Parker et al. 2017). Mice were imported from Cambridge University.

MMTV-PyMT mice (MT#634 line) (FVB/N pure background) were described previously (Guy et al. 1992). Mice were purchased from Charles Rivers Laboratory.

2.2.5.1 Backcrossing and tumor latency comparison

MMTV-PyMT mice were crossed with both *TRE-Omomyc;CMV-rtTA* and *TRE-Omomyc;βactin-rtTA* mice. In the first case, mice were backcrossed for 4 generations to dilute the C57BL/6 background. After backcrossing, tumor growth from *MMTV-PyMT;TRE-Omomyc;CMV-rtTA* females was compared with the one from *MMTV-PyMT* females. Tumors were measured weekly by caliper from 4 to 13 weeks of age, and their volume calculated using the following formula: volume = (length x width)^2 / 2. At 13 weeks, mice were euthanized by CO_2 inhalation and their lungs perfused with 4% buffered formaldehyde, washed with PBS, fixed for 48h in buffered 4% formaldehyde, transferred to 70% ethanol and embedded in paraffin. Lung sections were stained with hematoxylin and eosin (H&E) and metastatic foci were counted and their area measured with ImageJ.

2.2.5.2 Immunofluorescence

MMTV-PyMT;TRE-Omomyc, *MMTV-PyMT;TRE-Omomyc;CMV-rtTA* and *MMTV-PyMT;TRE-Omomyc;βactin-rtTA* mice were treated with 5% sucrose or 2 g/L doxycycline in 5% sucrose in their drinking water for 1 week. Then, mice were euthanized by CO_2 inhalation and their pancreas, lungs and mammary fat pads fixed in buffered 4% formaldehyde for 48 hours, transferred to 70% ethanol and paraffin-embedded. Sections were cut at 4 micrometers thick. Antigen retrieval was performed by heating 20 min at 400 W in a microwave in 0.01 M citrate buffer pH 6.0. After blocking 45 minutes in 3% BSA and washing in PBS, slides were incubated overnight at 4ºC with 0.02 mg/mL rabbit polyclonal anti-Omomyc antibody diluted 1/100 in Dako Ready-to-use diluent (Dako S2022). After a PBS wash, slides were incubated with goat anti-rabbit IgG (H+L)–AlexaFluor®488 conjugate (Thermo Fisher Scientific A-11008) diluted 1/200 and stained with Hoechst 33258 (Sigma) diluted 1/10,000, washed once with water and mounted with Fluorescence mounting medium (Dako S3023). The same procedure was performed in pancreas sections from *TRE-Omomyc;CMV-rtTA* mice treated with doxycycline at UCSF.

2.2.5.3 Sequencing

Tissue samples from *TRE-Omomyc;CMV-rtTA* mice from UCSF and *MMTV-PyMT;TRE-Omomyc;CMV-rtTA* generated at VHIR were collected and their genomic DNA extracted with the DNeasy® Blood & Tissue Kit (Qiagen). Omomyc was amplified by PCR for 30 cycles and an annealing temperature of 72ºC with the following primers (forward: CGAGTAGGCGTGTACGGTGGGAGG 0.5 µM, reverse: GGGCGGCCGCGGATCCTTACGCACAAGAGTTCCGTAGCTG 0.5 µM), 200 µM dNTP mix (Agilent) and 2U Phusion® High-Fidelity DNA polymerase (New England BioLabs) in a final volume of 50 µL.

PCR products were run in a 1% agarose gel for 45 minutes at 85V. Bands of ~400 bp corresponding to Omomyc were cut and purified with the Zymoclean™ Gel DNA Recovery kit (Zymo Research). Samples were sequenced by capillary electrophoresis using the High Technology Unit (UAT) services at VHIR. Briefly, samples were adjusted to 100 ng/µL, specific sequencing primers added at 5 µM (forward: TCAAGAGGCGAACACACAAC, reverse: GAGCTTTTGCGTCTCTGCTT) and a final volume of 10 µL was sent to the external provider Macrogen Europe for further sequencing.

2.2.5.4 Induction of Omomyc expression and tumor/metastasis quantification

5 week old *MMTV-PyMT;TRE-Omomyc;CMV-rtTA*, *MMTV-PyMT;TRE-Omomyc;βactin-rtTA* and *MMTV-PyMT;TRE-Omomyc* female mice were treated with 5% sucrose or 2g/L doxycycline in 5% sucrose added to their drinking water for 8 weeks. Primary tumors were measured weekly by caliper and their volume calculated using the following formula: volume = (length x width)^2 / 2. At 13 weeks, mice were euthanized by CO_2 inhalation and their mammary fat pads photographed and weighed. Lungs were perfused with 4% buffered formaldehyde and washed with PBS. Mammary fat pads and lungs were fixed for 48h in buffered 4% formaldehyde, transferred to 70% ethanol and embedded in paraffin. The whole lung was sectioned and serial sections were stained with H&E. Metastatic foci were counted and their area measured with ImageJ.

2.3 Statistics

Statistical analysis and representation of the data was performed using GraphPad Prism 6. For histograms, mean + standard deviation (SD) is shown. For scattered dot and box & whiskers plots, mean ± standard deviation (SD) is shown. For X-Y graphs, mean ± standard error of the mean (SEM) is shown to help visualization of the data. When the number of biological replicates (n) < 8, parametric tests were used. When n ≥ 8, a d'Agostino-Pearson omnibus normality test was used. If the test confirmed a Gaussian distribution of the data, a parametric test was used. Otherwise, non-parametric tests were used.

To determine statistical significance among two groups, a two-tailed unpaired T test (parametric) or a two-tailed Mann-Whitney test (non-parametric) was used. When comparing 3 or more groups, one-way ANOVA (parametric) or Kruskal-Wallis (non-parametric) was used for the analysis of variance, and the statistical difference between groups was determined via Dunnett's (parametric) or Dunn's (non-parametric) multiple comparisons test. For all tests, an alpha level of 0.05 was established. In all graphs, *, **, *** and **** are used to describe p values below 0.05, 0.01, 0.001 and 0.0001 respectively, as stated in figure legends. For all histograms, asterisks above one bar indicate statistical significance between that bar and the control group (filled with black). For other graphs, a line between the statistically significant groups is drawn.

To identify outliers, the interquartile range (25% percentile - 75% percentile) was multiplied by 1.5 and the result was added to the 75% percentile and subtracted from

the 25% percentile. If one or more values were outside the range between these two numbers, it was considered an outlier and discarded from the analysis.

RESULTS

1 PART 1

1.1 Ibrutinib prevents mast cell degranulation and reduces cell proliferation and inflammatory cell infiltration

For *in vivo* studies, we used the *p53$^{ER/ER}$;LSLKras^{G12D};Pdx1-Cre* immune competent mouse model of PDAC. In this model, the disruption of p53 signaling in combination with Kras mutation leads to rapid tumorigenesis and histopathological features typical of human PDAC, starting with pancreatic intraepithelial neoplasia (PanIN1a/b, PanIN2 and PanIN3) that lead to the appearance of adenocarcinomas within 8 weeks. At this stage the animals were treated with ibrutinib (n=4), added at a dose of 35 mg/Kg/day to their drinking water, or with vehicle control (n=4) (Figure 14A).

No detectable side effects of the treatment were observed and the animals did not lose significant weight throughout (Figure 14B). Mice were euthanized 4 weeks later and their pancreata harvested for analysis. As expected, mast cells were still recruited to the tumor stroma, but their degranulation was efficiently inhibited by ibrutinib treatment. In vehicle-treated mice, the border of many mast cells was broken and the content of their granules released, while ibrutinib-treated mast cells were intact and displayed concentrated staining (Figure 14C). Strikingly, tumors treated with ibrutinib displayed a significant reduction in their proliferation rate (Figure 14D). Since the decrease in proliferation seemed to occur both in the tumor cells and in the desmoplastic stroma, immune cell infiltration was quantified. CD11b positive leukocytes (neutrophils, natural killer cells, granulocytes and macrophages) and F4/80 positive macrophages were both reduced as shown by immunohistochemistry (IHC) (Figure 14E). These results were confirmed by flow cytometry in pancreas cell suspensions of ibrutinib-treated and untreated tumor-bearing animals, as well as healthy littermates (Figure 14F).

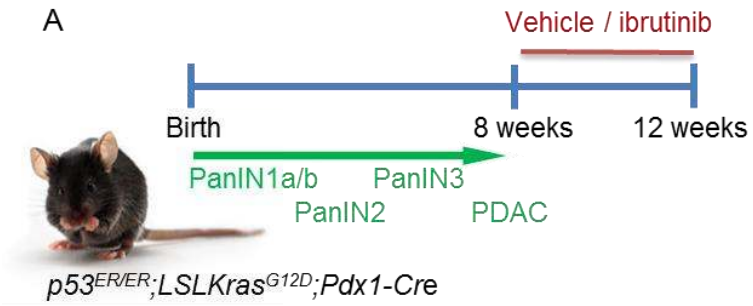
A
Vehicle / ibrutinib
Birth
8 weeks
12 weeks
PanIN1a/b
PanIN3
PanIN2
PDAC
p53ER/ER;LSLKrasG12D;Pdx1-Cre

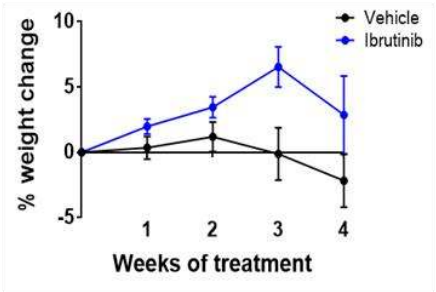
B
% weight change
Vehicle
Ibrutinib
Weeks of treatment

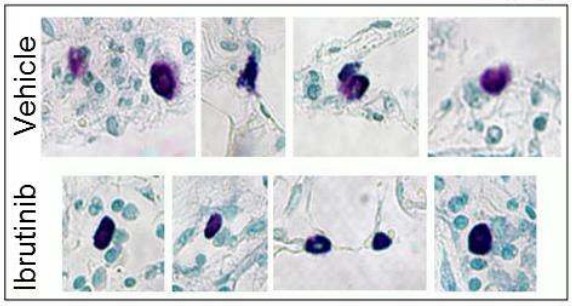
C
Vehicle
Ibrutinib

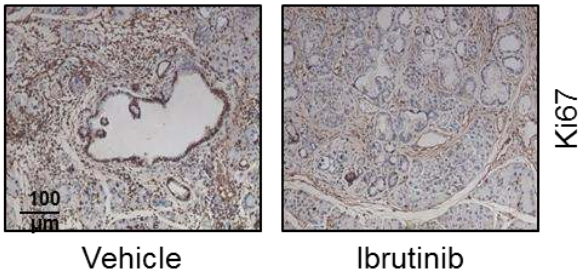
D
100 µm
Ki67
Vehicle
Ibrutinib

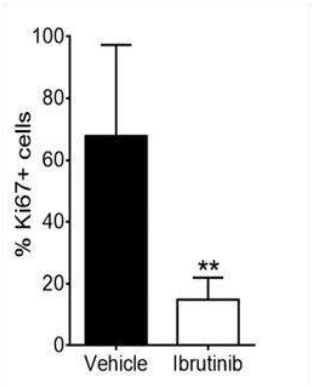
% Ki67+ cells
Vehicle
Ibrutinib

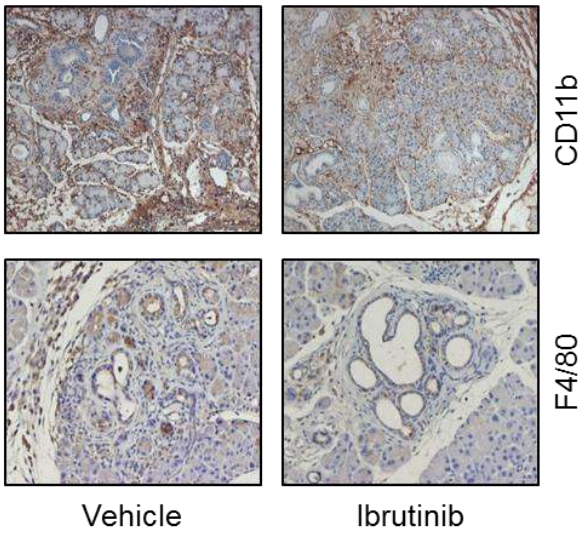
E
CD11b
F4/80
Vehicle
Ibrutinib

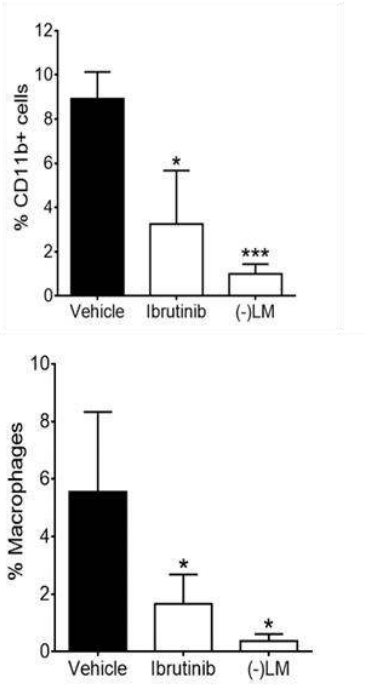
F
% CD11b+ cells
Vehicle
Ibrutinib
(-)LM
% Macrophages
Vehicle
Ibrutinib
(-)LM

Figure 14. Ibrutinib treatment has a profound effect on the tumor microenvironment in a transgenic mouse model of PADC. Tumor-bearing *p53$^{ER/ER}$;LSLKras^{G12D};Pdx1-Cre* mice were treated with vehicle or ibrutinib for 4 weeks.

A. Schematic representation of the mouse model. PanIN: pancreatic intraepithelial neoplasia. PDAC: pancreatic ductal adenocarcinoma.
B. Weekly change in bodyweight represented as percentage from treatment onset. Results shown represent mean ± SEM.
C. Toluidine blue staining was performed on pancreatic samples from tumor-bearing mice. In vehicle-treated mice the mast cell border is broken and the content of their granules is being released, while ibrutinib-treated mast cells are intact and display concentrated staining.
D. Histological analysis of pancreata shows a reduction in Ki-67 positivity in ibrutinib-treated mice compared to control animals. Statistical significance was determined via two-tailed Mann-Whitney test (**, P < 0.01). Results shown represent mean + SD. Three animals per condition and 5 sections per animal were analyzed. All cells in the tumor area were scored, independently of their cell type.
E. IHC shows a clear reduction of CD11b and F4/80 positivity in ibrutinib-treated compared to vehicle-treated mice.
F. Percentages of CD11b+ cells (CD45+CD11c-) and tumor-associated macrophages (CD45+CD11b+Ly6C-Ly6G-F4/80+) in single cell suspensions of normal pancreas isolated from negative untreated littermates [(-)LM], and from tumor-bearing mice treated with ibrutinib or vehicle, as assessed by flow cytometry and expressed as a percentage of total cells. Statistical significance was determined via two-tailed unpaired T test (*, P < 0.05; ***, P < 0.001). . Results shown represent mean + SD. At least three animals per condition were analyzed.

1.2 Ibrutinib reduces collagen deposition

Surprisingly, the most striking change induced by ibrutinib treatment in the tumor stroma was on fibrosis, reflected by collagen deposition as detected by Picrosirius Red staining, a three-step dyeing protocol which stains specifically collagen I and III fibrils. Treatment with ibrutinib dramatically reduced the amount of collagen present in the tumors (Figure 15A). To quantify the extent of fibrosis, sections were assigned blindly into three different categories (+, ++ or +++) according to the extent and intensity of red stain (Figure 15B). Most tumors in vehicle-treated mice fell into the category with the highest collagen content, while most ibrutinib-treated tumors presented either low or intermediate staining (Figure 15C).

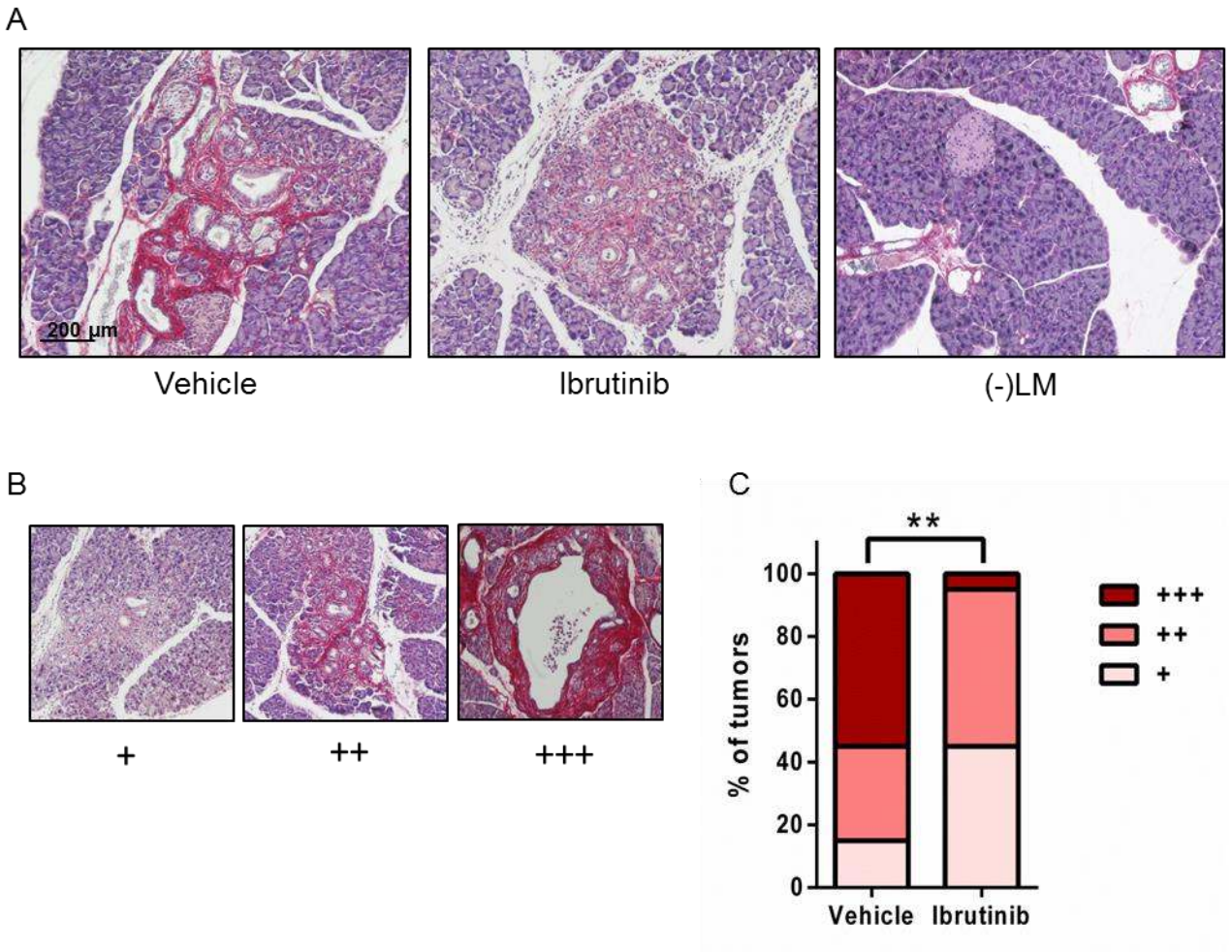

Figure 15. Ibrutinib reduces collagen deposition in a transgenic mouse model of PDAC. Tumor-bearing *p53$^{ER/ER}$;LSLKras^{G12D};Pdx1-Cre* mice were treated with vehicle or ibrutinib for 4 weeks.

A. Picrosirius Red staining of pancreas samples from tumor-bearing mice treated with ibrutinib or vehicle and from negative littermates [(-)LM]. Animals treated with ibrutinib show a reduced amount of collagen compared to vehicle-treated animals. Four animals per condition and five sections per animal were analyzed. Red staining shows collagen in the tumor stroma.

B. Representative images of tumors stained with Picrosirius Red classified into three categories (+, ++ or +++) according to their collagen content.

C. Scoring of treated (n = 20) and untreated (n = 20) tumors according to their collagen content. Sections stained with Picrosirius Red were scored blindly and assigned to three categories (+, ++ or +++). The percentages of tumors classified into each category are shown. A χ^2 test of homogeneity was utilized for statistical analysis of the data (**, $P < 0.01$).

1.3 Ibrutinib does not have a direct effect on PDAC tumor cells *in vitro*

In order to verify that this effect on fibrosis was specifically due to mast cell interference, we first asked whether ibrutinib could have any direct activity on tumor cells *per se*. In order to address this question we treated 4 different human PDAC cell lines with increasing amounts of ibrutinib *in vitro*. We chose four cell lines presenting a similar mutational profile to the one displayed by our mouse model and the majority of human tumors (i.e. Kras and p53 mutation): MIA PaCa-2, YAPC, PSN-1 and PA-TU-8988T. Two Non-Small Cell Lung Cancer (NSCLC) cell lines previously shown to respond to ibrutinib, PC9 and H292 (Gao et al. 2014), were added to the panel as positive controls. While both NSCLC cell lines responded to ibrutinib in a dose-dependent manner (Figure 16, in red), none of the PDAC ones responded significantly to the treatment (Figure 16, in black), pointing to the activity of ibrutinib on tumor stroma – rather than a direct effect on pancreatic cell survival – as the best candidate for ibrutinib's anti-tumorigenic effect in PDAC (Figure 16).

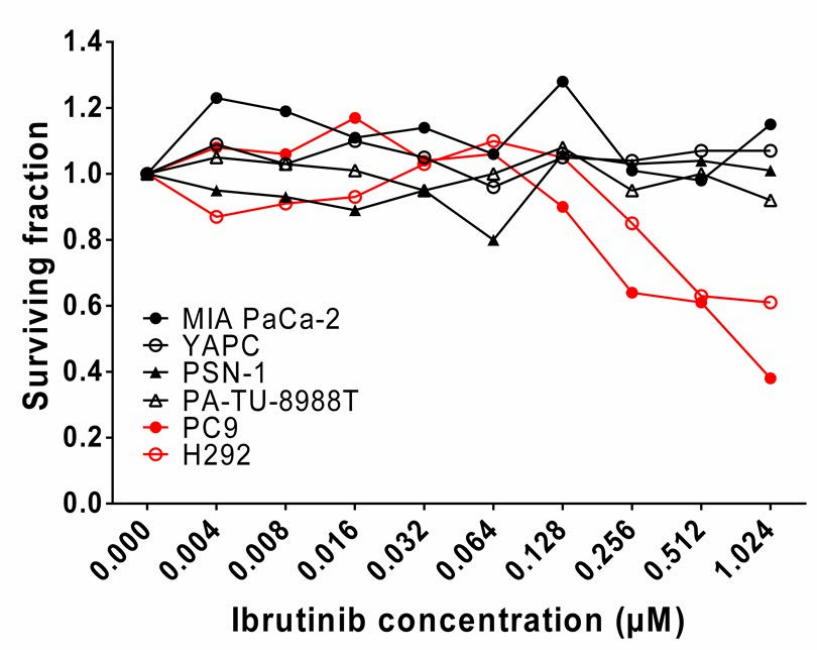

Figure 16. Ibrutinib does not affect growth of PDAC cell lines.
Four PDAC cell lines (MIA PaCa-2, YAPC, PSN-1 and PA-TU-8988T, in black) and two NSCLC cell lines (PC9 and H292, in red) were treated with increasing concentrations of ibrutinib ranging from 0.004 to 1.024 μM. While the NSCLC cells showed a dose-dependent decrease in viability, PDAC cell lines were unaffected.

1.4 Ibrutinib reduces fibrosis in a B-cell independent manner

With this line of reasoning in mind and to verify the hypothesis that mast cell interference played a role in the anti-fibrotic effect displayed by ibrutinib, we performed two independent control experiments to exclude the known effect of ibrutinib on B cell signaling as the cause of the reduced fibrosis.

In the first one, we made use of subcutaneous xenografts of a patient-derived PDAC tumor in NOD/SCID mice, which are defective for both B and T cell function. 6 weeks after surgery, mice were treated with ibrutinib (n=14) or vehicle control (n=13) until tumors reached 1500 mm^3 (Figure 17A). Once again, ibrutinib did not affect the weight of the animals (Figure 17B), prevented mast cell degranulation (Figure 17C) and led to a reduction in tissue fibrosis detected by Picrosirius Red staining (Figure 17D and E), excluding B and T cell signaling modulation as ibrutinib's main mechanism of action in this context. Importantly, the animals treated with ibrutinib also showed a delay in tumor growth, which was translated into a significant survival advantage, when compared to untreated littermates (Figure 17F). Interestingly, in contrast to the PDAC transgenic mouse model, IHC analysis of F4/80 and Cd11b positive cells showed only a slight and non-significant reduction of both cell types (Figure 17G and H).

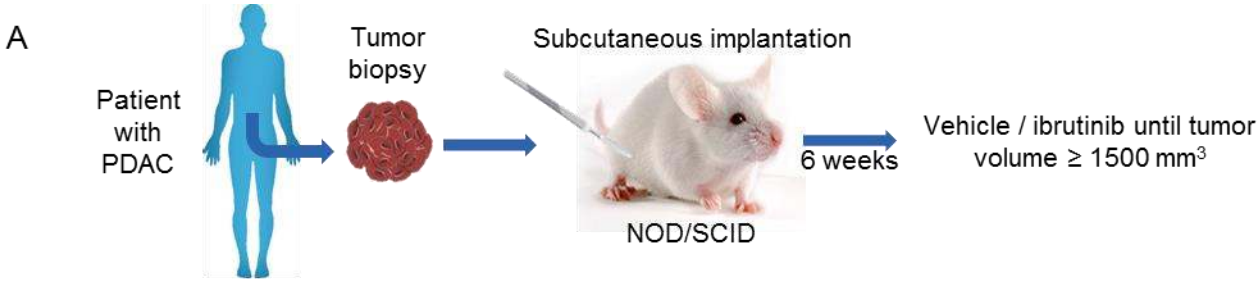

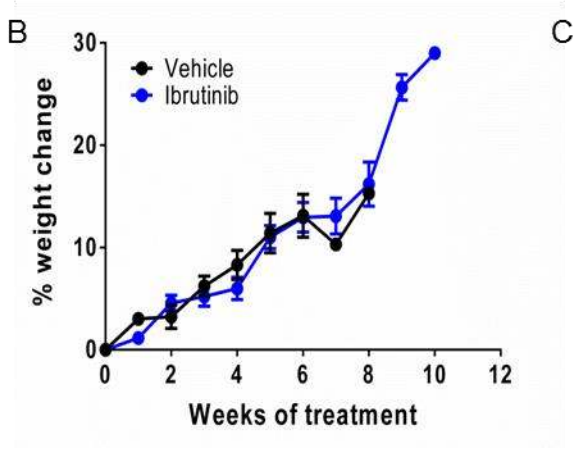

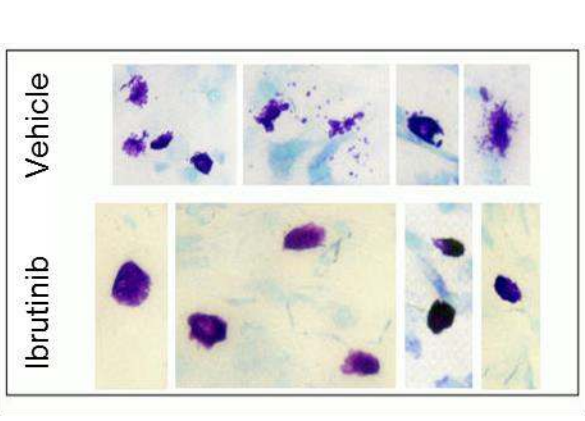

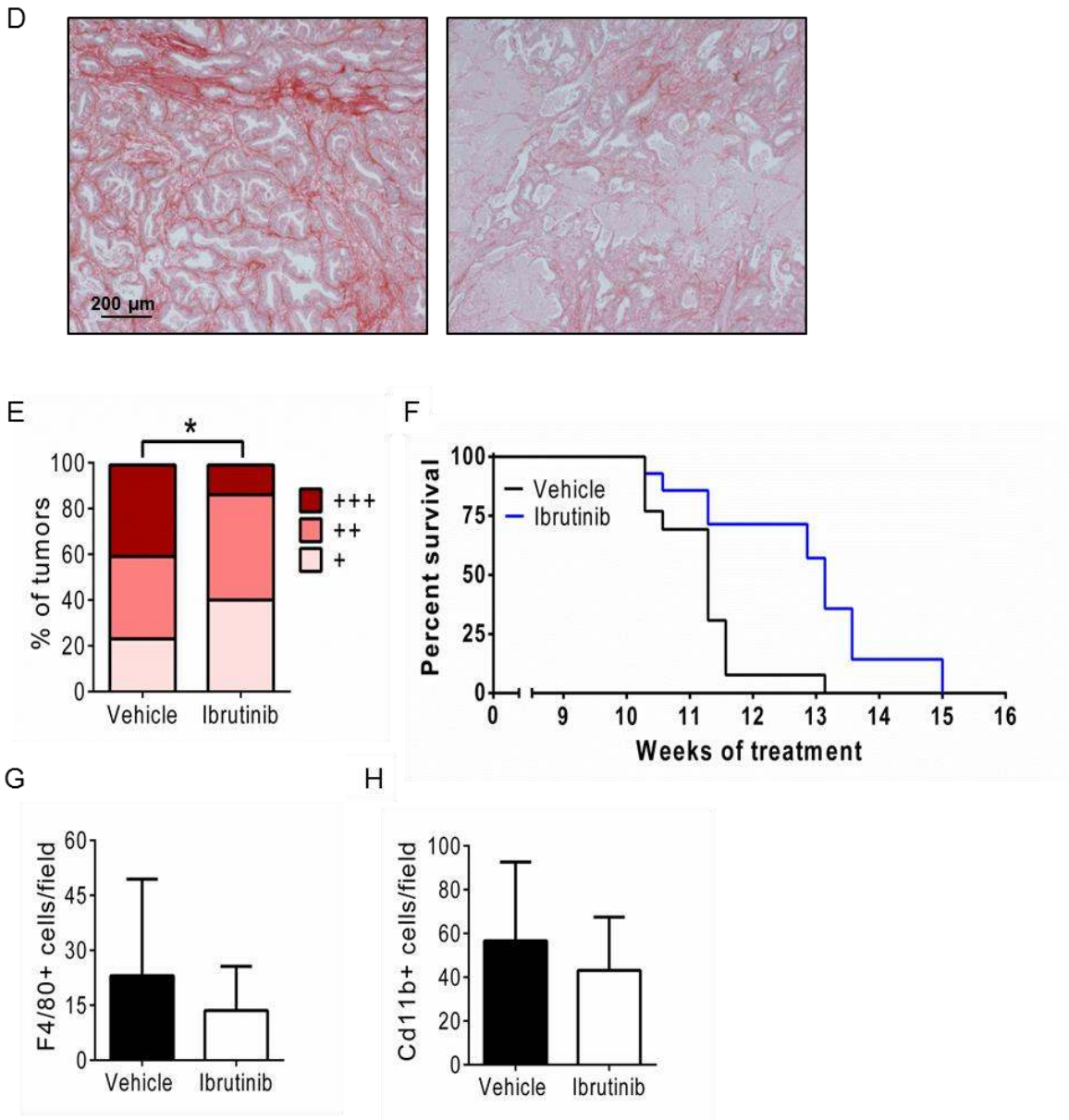

Figure 17. Ibrutinib diminishes tissue fibrosis in a PDX model of PDAC. Tumor-bearing NOD/SCID mice were treated with vehicle or ibrutinib until tumor volume reached 1500 mm^3.

A. Schematic representation of the model.

B. Weekly change in bodyweight represented as percentage from treatment onset. Results shown represent mean ± SEM.

C. Toluidine blue staining of tumor samples. In control mice the mast cell border is broken and the content of their granules is being released, while ibrutinib-treated mast cells are intact and display concentrated staining.

D. Picrosirius Red staining was performed on tumor samples from untreated or ibrutinib-treated mice and indicates collagen deposition in the tumor stroma. Six animals per condition and four sections per animal were analyzed.

E. Scoring of sections from treated (n = 26) and untreated (n = 26) tumors according to their collagen content. Sections stained with Picrosirius Red were scored blindly and assigned to three

categories (+, ++ or +++). The percentages of tumors classified into each category are shown. A χ^2 test of homogeneity was utilized for statistical analysis of the data (*, P = < 0.05).

F. Kaplan-Meyer survival curve of mice treated with ibrutinib (n = 14) or vehicle (n = 13). Ibrutinib treatment reduces tumor growth which translates into a significant survival advantage. Log-rank test was utilized for statistical analysis of the data (P = 0.0021).

G. Quantification of F4/80-positive cells per microscopic field on the border of the subcutaneous tumors shows a non-significant reduction in ibrutinib-treated vs. control mice. Statistical significance was determined via two-tailed Mann-Whitney test. Results shown represent mean ± SD. At least three animals per condition and four sections per animal were analyzed.

H. Quantification of Cd11b-positive cells per microscopic field on the border of the subcutaneous tumors shows a non-significant reduction in ibrutinib-treated vs. control mice. Statistical significance was determined via two-tailed Mann-Whitney test. Results shown represent mean ± SD. At least three animals per condition and four sections per animal were analyzed.

1.5 Ibrutinib's effect on the tumor stroma is mast-cell dependent

In a second set of experiments, we made use of sodium cromoglycate (cromolyn), a well-characterized blocker of mast cell degranulation and inflammogen release (Thompson et al. 1983; Soucek et al. 2007). We treated the *p53$^{ER/ER}$;LSLKras^{G12D};Pdx1-Cre* mice intraperitoneally with a daily injection of 10 mg/kg of cromolyn (n=6) or vehicle (n=5), starting at 8 weeks of age (Figure 18A). The animals were euthanized 4 weeks later and their pancreata analyzed. We verified that cromolyn treatment did not induce significant weight loss (Figure 18B) and blocked mast cell degranulation (Figure 18C). Strikingly, treatment with cromolyn recapitulated the anti-fibrotic effect displayed by ibrutinib (Figure 18D and E) confirming that mast cell function is required for maintenance of tumor fibrosis. Once again, this effect was accompanied by a reduction in F4/80+ cells and a significant decrease in CD11b+ cells in the tumor stroma (Figure 18F and G).

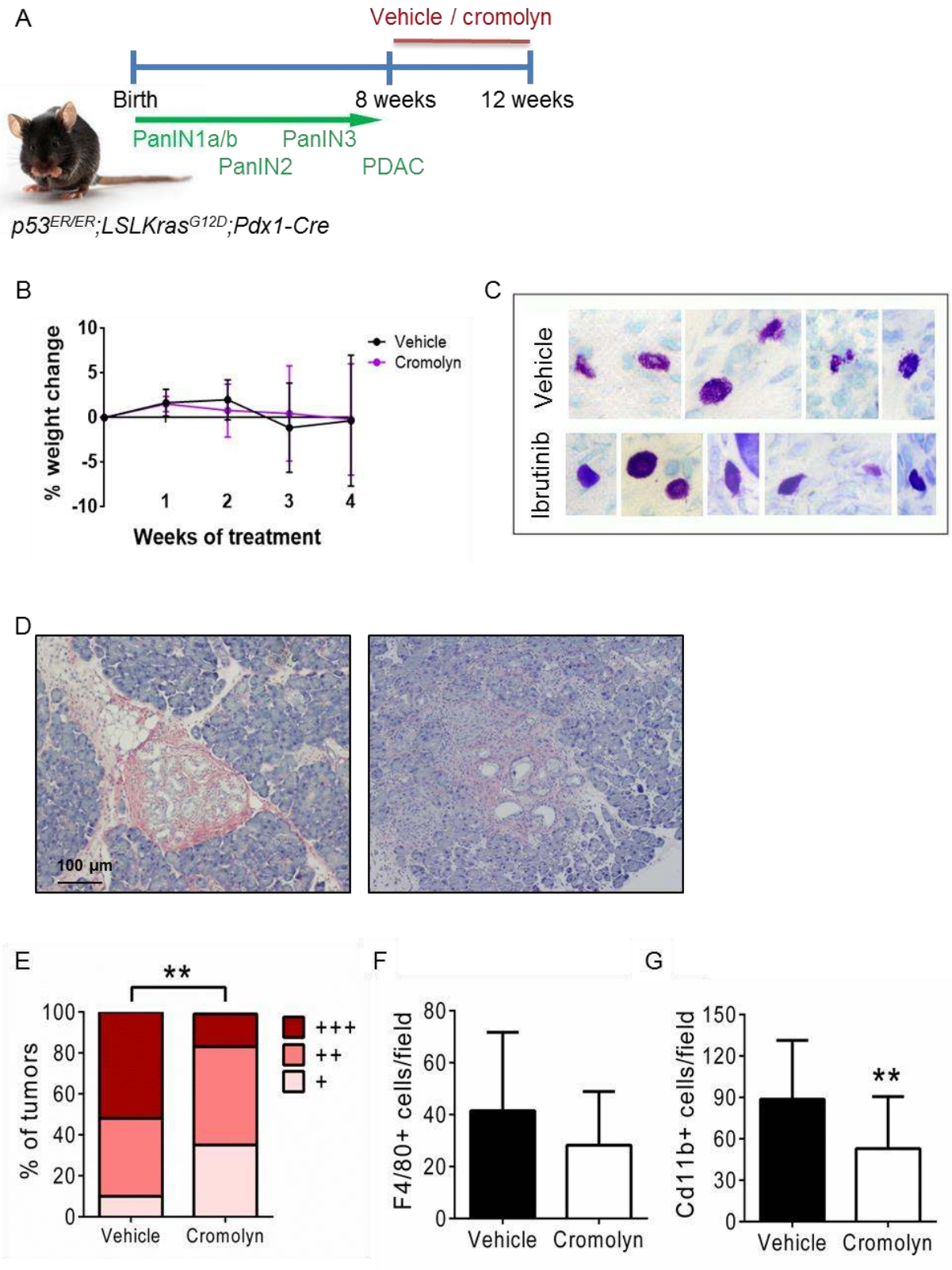

Figure 18. Mast cell function inhibition by cromolyn diminishes tissue fibrosis in a transgenic mouse model of PDAC. Tumor-bearing *p53$^{ER/ER}$;LSLKras^{G12D};Pdx1-Cre* mice were treated with vehicle or cromolyn for 4 weeks.

A. Schematic representation of the mouse model. PanIN: pancreatic intraepithelial neoplasia. PDAC: pancreatic ductal adenocarcinoma.

B. Weekly change in bodyweight represented as percentage from treatment onset. Results shown represent mean ± SEM.
C. Toluidine blue staining of tumor samples. In control mice the mast cell border is broken and the content of their granules is being released, while cromolyn-treated mast cells are intact and display concentrated staining.
D. Mice were treated with intraperitoneal sodium cromoglycate (n = 6) or vehicle control (n = 5) for 4 weeks. Histologic analysis of pancreata by Picrosirius Red staining shows reduced collagen deposition in cromolyn-treated mice compared with vehicle-treated control animals. Five animals per condition and at least five sections per animal were analyzed. Red staining shows collagen in the tumor stroma.
E. Scoring of treated (n = 30) and untreated (n = 25) tumors according to their collagen content. Sections stained with Picrosirius Red were scored blindly and assigned to three categories (+, ++, or +++). The percentages of tumors classified into each category are shown. A χ^2 test of homogeneity was utilized for statistical analysis of the data (**, P < 0.01).
F. Quantification of F4/80-positive cells per microscopic field in the tumor area shows a nonsignificant reduction in cromolyn-treated versus vehicle-treated mice. Statistical significance was determined via two-tailed Mann–Whitney test. Results shown represent mean ± SD. Five animals per condition and four sections per animal were analyzed.
G. Quantification of CD11b-positive cells per microscopic field in the tumor area shows a significant reduction in cromolyn-treated versus vehicle-treated mice. Statistical significance was determined via two-tailed Mann–Whitney test (**, P < 0.01). Results shown represent mean ± SD. Five animals per condition and four sections per animal were analyzed.

1.6 Ibrutinib improves the outcome of standard care in a transgenic mouse model of PDAC

In PDAC, dense stromal fibrosis is a considerable obstacle to therapeutic intervention. Consequently, we hypothesized that the anti-fibrotic effect of ibrutinib represented a promising therapeutic opportunity to improve the outcome of standard of care. Therefore, we performed two independent survival experiments in the *p53$^{ER/ER}$;LSLKras^{G12D};Pdx1-Cre* mouse model: the first one sought to explore the therapeutic impact of ibrutinib alone and the second one to assess the impact of ibrutinib in combination with gemcitabine, the best characterized therapy available to pancreatic cancer patients during the past decade (Figure 19A). As monotherapy, ibrutinib did not induce any toxicity in the long term (Figure 19B) and conferred a significant survival advantage to treated mice (n = 14) compared to untreated controls (n = 13) (Figure 19C). In the second experiment, gemcitabine alone (n = 9) resulted in slight toxicity (Figure 19D and E), although ibrutinib (n = 8) ameliorated it and significantly extended survival compared to gemcitabine alone (Fig 19E), confirming

our hypothesis that the standard of care outcome can be improved by addition of ibrutinib.

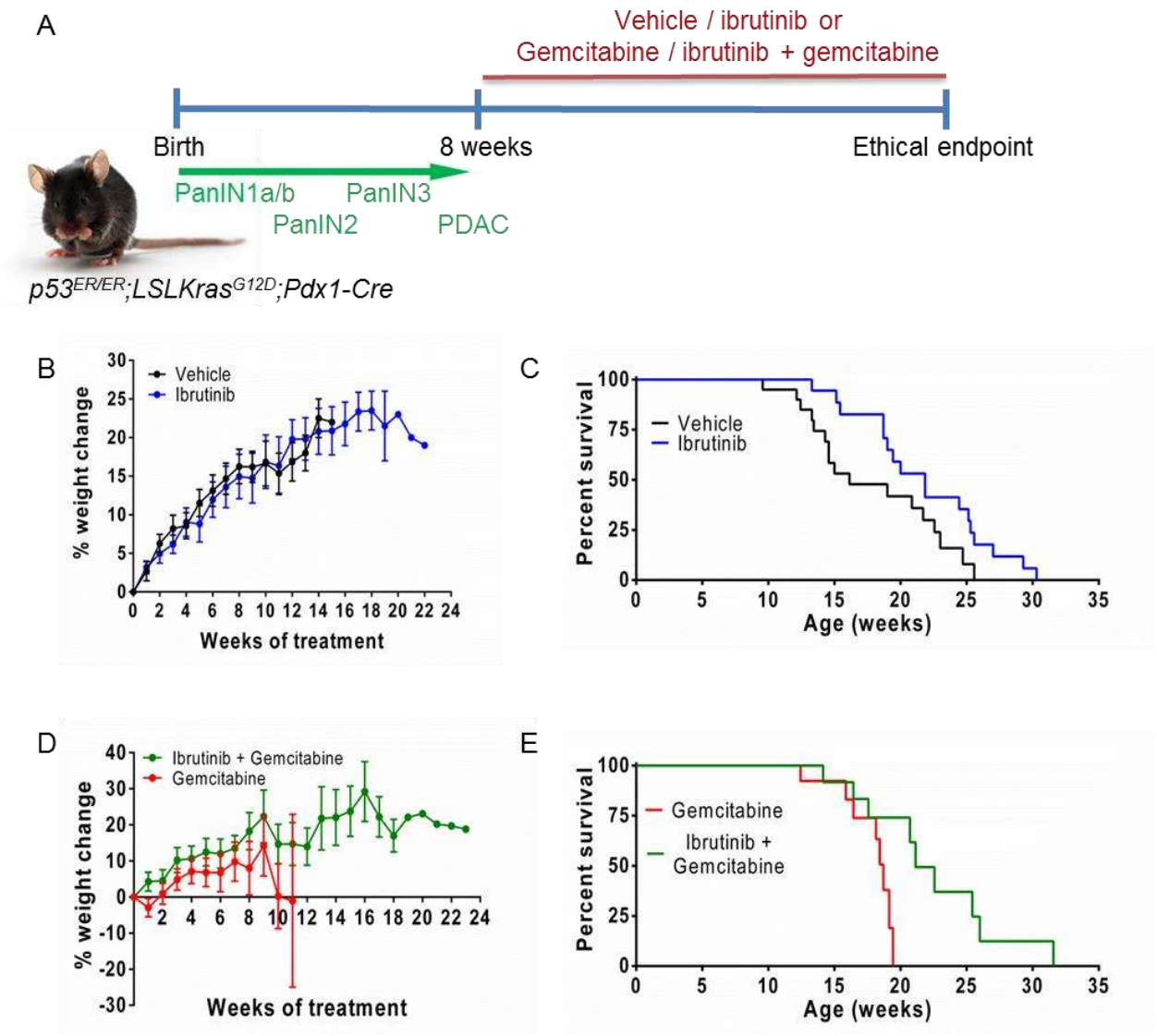

Figure 19. Ibrutinib has a significant therapeutic impact as monotherapy and in combination with standard of care. *p53$^{ER/ER}$;LSLKras^{G12D};Pdx1-Cre* mice were treated with vehicle, ibrutinib, gemcitabine or gemcitabine + ibrutinib until they had to be euthanized.

A. Schematic representation of the mouse model. PanIN: pancreatic intraepithelial neoplasia. PDAC: pancreatic ductal adenocarcinoma.

B. Weekly change in bodyweight from mice treated with vehicle or ibrutinib, represented as percentage from treatment onset. Results shown represent mean ± SEM.

C. Kaplan-Meyer survival curve of mice treated with ibrutinib or vehicle. Ibrutinib treatment confers a significant survival advantage. Log-rank test was utilized for statistical analysis of the data (P = 0.03).

D. Kaplan-Meyer survival curve of mice treated with gemcitabine or the combination of gemcitabine and ibrutinib. Addition of ibrutinib to standard of care significantly improves animal survival. Log-rank test was utilized for statistical analysis of the data (P = 0.025).

E. Weekly change in bodyweight from mice treated with gemcitabine or ibrutinib + gemcitabine, represented as percentage from treatment onset. Results shown represent mean ± SEM.

1.7 The synergistic effect between ibrutinib and gemcitabine is dependent on the tumor stroma

To validate our hypothesis that ibrutinib improves the outcome of gemcitabine-treated mice due to its anti-fibrotic effect, we performed one more experiment in a mouse model of PDAC that lacks the desmoplastic stroma. The human PDAC cell line MIA PaCa-2 was infected with a lentiviral vector harboring constitutive expression of luciferase, inoculated orthotopically in the pancreas of BALB/c nude mice and tumor growth followed by IVIS imaging. 9 days after inoculation, when tumors were established, mice were divided into 4 groups and treated with vehicle (n = 10), ibrutinib (n = 10), gemcitabine (n = 10) or ibrutinib + gemcitabine (n = 10) for 5 weeks (Figure 20A). Even though few mast cells were present in the tumor stroma, treatment with ibrutinib blocked their degranulation (Figure 20B). Only animals treated with gemcitabine suffered a slight toxicity resulting in weight loss during the first two weeks (Figure 20C). The weekly follow-up of luminescence by IVIS showed that these mice presented a non-significant decrease in tumor burden, but no effect of ibrutinib as a monotherapy and no additive effect nor synergy between ibrutinib and gemcitabine was observed (Figure 20D). Curiously, in the *ex vivo* analysis of the pancreata, ibrutinib and gemcitabine seemed to have an effect on reducing tumor burden although this was non-significant, but again no additive effect nor synergy was observed in the ibrutinib + gemcitabine group (Figure 20E). Similar results were obtained when measuring pancreas weight at the endpoint, with only gemcitabine as monotherapy showing significant differences with the control group (figure 20F). Tumor samples from each group were stained with Picrosirius Red and, as expected from previous experience with this model, no collagen fibers were detected in any of the groups; while a positive control from a subcutaneous PDX obtained by inoculating a tumor biopsy in BALB/c nude mice shows clear positivity (Figure 20G). The fact that this cell-line derived model lacks the desmoplastic stroma, combined with the observation that gemcitabine was effective as a monotherapy, suggests that fibrosis limits the action of gemcitabine and that its presence is a requirement for the synergy with ibrutinib.

A


MIA PaCa2 Fluc
Orthotopic inoculation
BALB/c nude
9 days
5-week treatment with:
- Vehicle
- Ibrutinib
- Gemcitabine
- Ibrutinib+gemcitabine

B

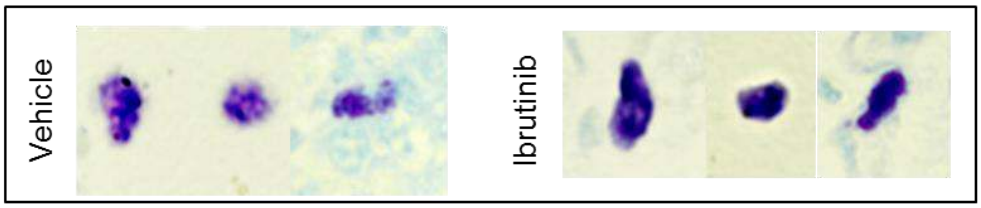
Vehicle
Ibrutinib

C

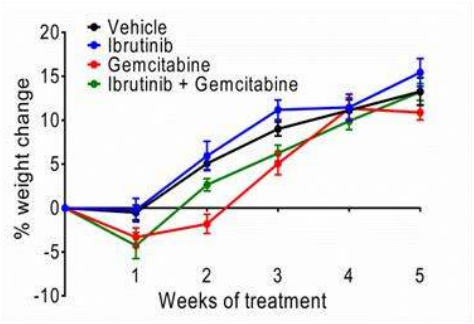
Vehicle
Ibrutinib
Gemcitabine
Ibrutinib + Gemcitabine
% weight change
Weeks of treatment

D

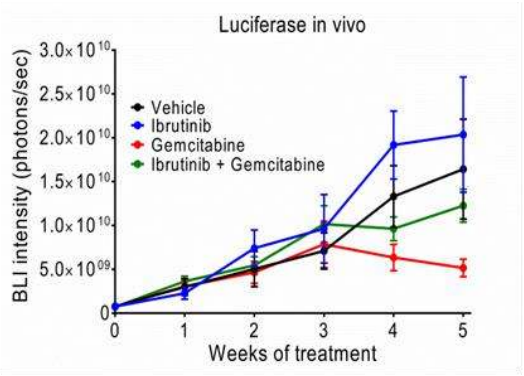
Luciferase in vivo
BLI intensity (photons/sec)
Vehicle
Ibrutinib
Gemcitabine
Ibrutinib + Gemcitabine
Weeks of treatment

E

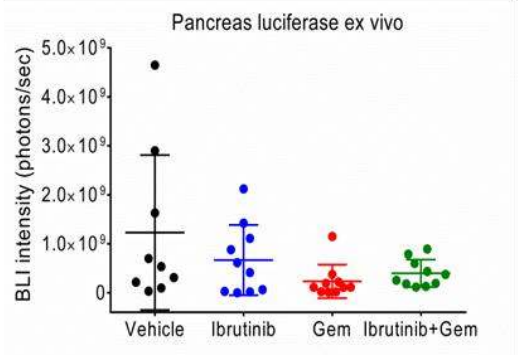
Pancreas luciferase ex vivo
BLI intensity (photons/sec)
Vehicle
Ibrutinib
Gem
Ibrutinib+Gem

F

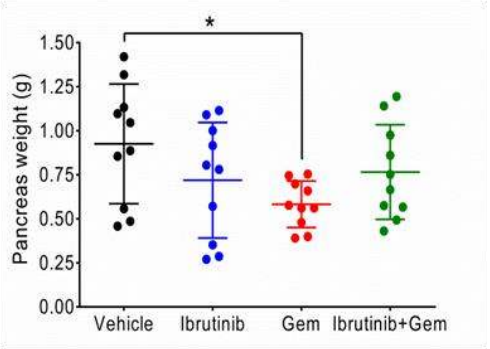
*
Pancreas weight (g)
Vehicle
Ibrutinib
Gem
Ibrutinib+Gem

G

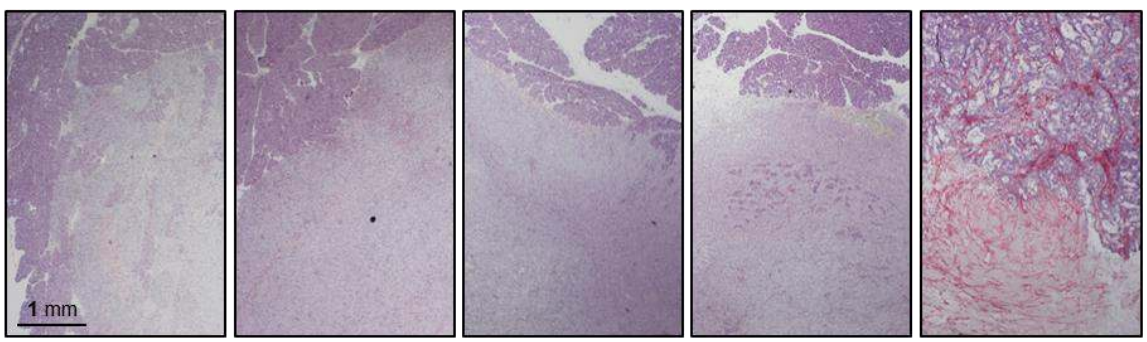
1 mm
Vehicle
Ibrutinib
Gemcitabine
Ibrutinib + Gem
Untreated PDX (positive control)

Figure 20. The absence of a desmoplastic stroma prevents ibrutinib from synergizing with gemcitabine.
MIA PaCa-2 cells where orhotopically injected in BALB/c nude mice that were treated with vehicle, gemcitabine, ibrutinib and ibrutinib + gemcitabine for 5 weeks.

A. Schematic representation of the model.
B. Toluidine blue staining of tumor samples. In control mice the mast cell border is broken and the content of their granules is being released, while ibrutinib-treated mast cells are intact and display concentrated staining.
C. Weekly change in bodyweight represented as percentage from treatment onset. Results shown represent mean ± SEM.
D. *In vivo* luciferase activity. While gemcitabine has a non-significant but evident effect on tumor growth, ibrutnib and ibrutinib + gemcitabine groups behave similarly to the vehicle-treated mice. One-way ANOVA was used for the analysis of variance, and the statistical difference between groups was determined via Dunnett's multiple comparisons test. Results shown represent mean ± SEM.
E. *Ex vivo* luciferase activity. Gemcitabine and ibrutinib + gemcitabine groups show a non-significant but evident effect on tumor burden compared with vehicle-treated mice, no synergy between gemcitabine and ibrutinib is observed. One-way ANOVA was utilized for statistical analysis of the data. Results shown represent mean ± SD
F. Pancreas weight at experimental endpoint. Only gemcitabine-treated mice show a significant decrease in weight. One-way ANOVA was used for the analysis of variance, and the statistical difference between groups was determined via Dunnett's multiple comparisons test (*, $P < 0.05$). Results shown represent mean ± SD.
G. Representative images of Hematoxylin + Picrosirius Red-stained tumors from mice treated with vehicle, ibrutinib, gemcitabine or the combination ibrutinib + gemcitabine show absence of collagen positivity in all groups. A positive sample from a subcutaneous PDX stained in parallel is shown (right panel).

Finally, we analyzed the presence of mast cells in the pancreas of transgenic C57BL/6-FVB/N mice with and without tumors and compared it with BALB/c nude mice, also with and without tumors (Figure 21). Normal pancreata from immune competent mice (*p53$^{ER/ER}$;LSLKras^{G12D}* and *p53$^{ER/ER}$;Pdx1-Cre*) presented relatively high mast cell infiltration, which was significantly increased in tumorigenic ones (*p53$^{ER/ER}$;LSLKras^{G12D};Pdx1-Cre*). On the contrary, immunocompromised mice showed low levels of mast cells in their pancreas before and after orthotopic inoculation of PDAC cells. These observations could explain the differences in tumor fibrosis observed between those models, as well as their difference in terms of responsiveness to the combination treatment with ibrutinib and gemcitabine.

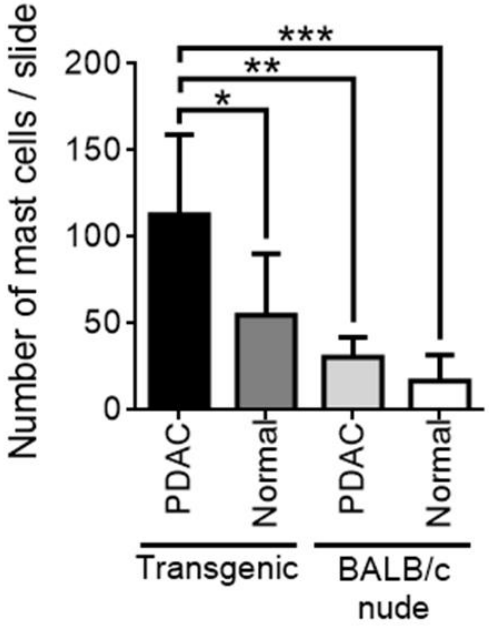

Figure 21: Mast cell infiltration is low in BALB/c nude mice with or without orthotopic cell-line derived tumors in comparison to PDAC-bearing *p53$^{ER/ER}$;LSLKras^{G12D};Pdx1-Cre* mice.

Quantification of toluidine-blue positive mast cells per slide in pancreas sections from *p53$^{ER/ER}$;LSLKras^{G12D};Pdx1-Cre* mice (Transgenic PDAC), *p53$^{ER/ER}$;LSLKras^{G12D}* and *p53$^{ER/ER}$;Pdx1-Cre* mice (Transgenic Normal), BALB/c nude mice inoculated with MIA PaCa-2 cells (BALB/c nude PDAC) and control BALB/c nude mice (BALB/c nude Normal) is shown. One-way ANOVA was used for the analysis of variance, and the statistical difference between groups was determined via Tukey's multiple comparisons test (*, $P < 0.05$; **, $P < 0.01$; ***, $P < 0.001$). Results shown represent mean + SD. At least 4 animals per condition were analyzed

2 PART 2

2.1 Omomyc is efficiently expressed in a panel of human breast cancer cell lines causing a dose-dependent reduction in colony formation capacity

To test the hypothesis that Omomyc is an effective therapy against breast cancer, we successfully infected a panel of well characterized and commercially available human breast cancer cell lines with lentiviral vectors containing a doxycycline-inducible Omomyc cassette or a GFP control. 11 stable cell lines representative of the four intrinsic molecular subtypes of breast cancer, with a special focus on the subtypes with fewer therapeutic options (HER2-enriched and triple negative), were generated and are described in table 3.

Luminal A	Luminal B	HER2-enriched	Triple negative
MCF7 pSLIK GFP	MDA-MB-361 pSLIK GFP	JIMT-1 pSLIK GFP	MDA-MB-231 pSLIK GFP
MCF7 pSLIK Omomyc	MDA-MB-361 pSLIK Omomyc	JIMT-1 pSLIK Omomyc	MDA-MB-231 pSLIK Omomyc
T47D pSLIK GFP		MDA-MB-453 pSLIK GFP	Cal51 pSLIK GFP
T47D pSLIK Omomyc		MDA-MB-453 pSLIK Omomyc	Cal51 pSLIK Omomyc
		BT474 pSLIK GFP	BT-549 pSLIK GFP
		BT474 pSLIK Omomyc	BT-549 pSLIK Omomyc
		SKbr3 pSLIK Omomyc	Hs578t pSLIK GFP
			Hs578t pSLIK Omomyc

Table 3. Panel of stable human breast cancer cell lines with inducible expression of Omomyc or GFP generated by lentiviral infection.

To assess the impact of Omomyc expression on the proliferative capacity of the cells, we utilized all the Omomyc-infected cell lines and a selection of GFP-infected ones to carry out clonogenic assays. Omomyc or GFP expression was induced by adding 0.6 µg/ml of doxycycline to the culture media, a concentration shown to have no effect in proliferation of normal cells by toxicity assays performed in the laboratory. Cells were treated for periods of 2 to 7 weeks depending on the proliferative rate of each cell line. While cells expressing GFP showed no impairment in their colony formation capacity, all Omomyc-expressing cells presented fewer and smaller colonies (Figure 22A). Quantification of the crystal violet intensity in each cell line revealed significant differences when Omomyc, but not GFP, was expressed (Figure 22B, left and right

panels). The degree of sensitivity to Omomyc expression was variable between cell lines and did not seem to correlate with the different molecular subtypes (Figure 22B, left panel). In parallel, Omomyc was detected by Western blot in cells treated for three days with doxycycline. A band of 11 kDa corresponding to Omomyc was present in cell extracts from all doxycycline-treated cells tested except the MDA-MB-453, the ones that showed the least response (Figure 22C). After this observation, we correlated the relative cell number obtained in the clonogenic assays with the levels of Omomyc expressed in each cell line and found it significant (Figure 22D). Hence, the variability in the response to Omomyc is not due to genetic differences among cell lines but rather to the amount of transgenic Omomyc that the cells are expressing.

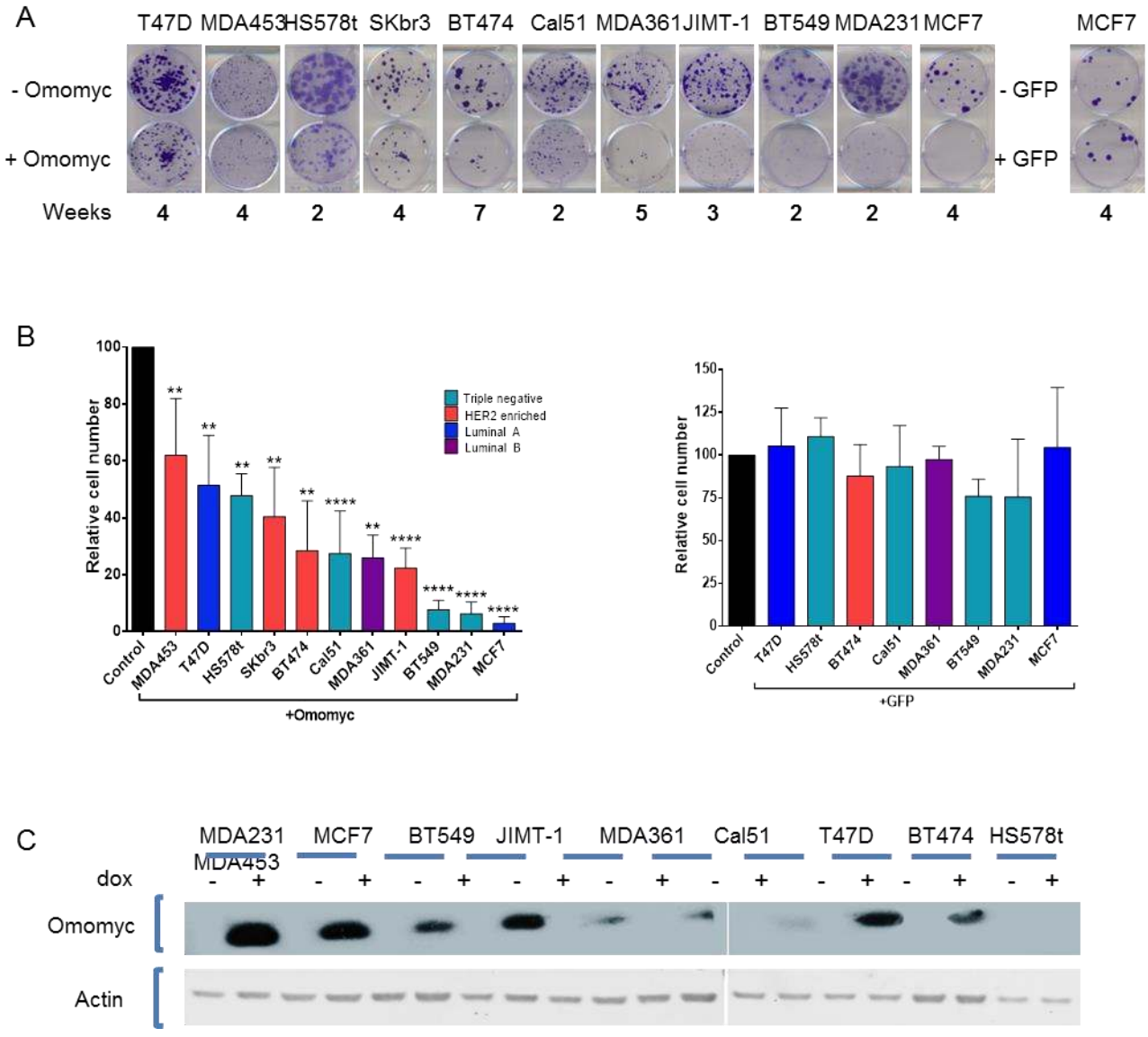

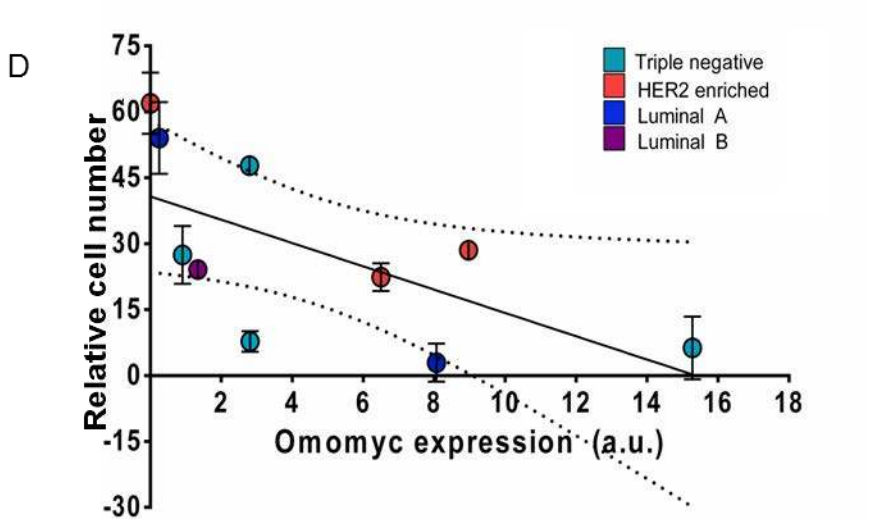

Figure 22. Clonogenic assays after Omomyc or GFP expression in a panel of human breast cancer cell lines shows a significant reduction in cell number when Omomyc is expressed, which correlates with its expression levels.

A. Representative images of wells stained with crystal violet after Omomyc expression in all cell lines. An example of a GFP-expressing cell line is also shown. Expression of Omomyc or GFP was induced by addition 0.6 μg/ml doxycycline in the culture media. Differences in the number and size of colonies are evident in the Omomyc-expressing cells.
B. Quantification of relative cell number after Omomyc (left panel) or GFP (right panel) expression. Statistical significance was determined via two-tailed Mann–Whitney test (**, $P < 0.01$; ****, $P < 0.0001$). Results shown represent mean + SD.
C. Western blot of Omomyc three days after addition of 0.6 μg/ml doxycycline.
D. Linear regression of relative cell number vs. Omomyc expression levels in each cell line. A significant correlation between Omomyc expression levels and its effect in terms of cell number reduction was determined by two-tailed Pearson correlation ($p < 0.05$). Results shown represent mean ± SD.

2.2 Omomyc impairs cell proliferation and arrests cells in G0/G1

The MDA-MB-231 pSLIK Omomyc cell line was chosen to characterize the phenotypic changes induced by Omomyc expression due to several reasons: it belongs to the triple negative molecular subtype, which lacks therapeutic options; it expresses high levels of Omomyc; it is tumorigenic in mice and it is highly metastatic *in vitro* and *in vivo*. MDA-MB-231 pSLIK GFP cells were used as controls for the effect of doxycycline alone and the expression of an exogenous protein in large amounts.

Omomyc expression was confirmed by flow cytometry and no leakiness was observed in untreated cells (Figure 23A). Then, to make sure that Omomyc was interfering with Myc transactivation functions, MDA-MB-231 pSLIK Omomyc cells were treated with

doxycycline for 3 days and Omomyc, c-Myc and RNA polymerase III (Pol III), a bona fide Myc target, were detected by Western blot (Figure 23B). As expected, c-Myc levels remained unchanged after Omomyc expression, but Pol III, a protein directly regulated by Myc (Gomez-Roman et al. 2003), was downregulated (Figure 23B) indicating that Omomyc was affecting Myc's transcriptional activity. Pol III downregulation was also observed in Cal51 and MCF7 cells expressing Omomyc (data not shown). As a consequence of such interference, in a proliferation assay, doxycycline addition to the culture media for 6 days caused a remarkable proliferation arrest in Omomyc-expressing cells, but not in GFP positive control cells (Figure 23C, crystal violet staining; and 23D, quantitation). We further characterized the cell cycle of MDA-MB-231 pSLIK GFP and pSLIK Omomyc cells treated with or without doxycycline for three days, looking at bromodeoxyuridine (BrdU) incorporation and propidium iodide (PI) staining. In these assays, Omomyc expression induced a clear reduction in DNA synthesis during the S phase of the cell cycle and caused accumulation of cells in the G0/G1 phase (Figure 23E, flow cytometry for BrdU-FITC; 23F, F and G, quantitation).

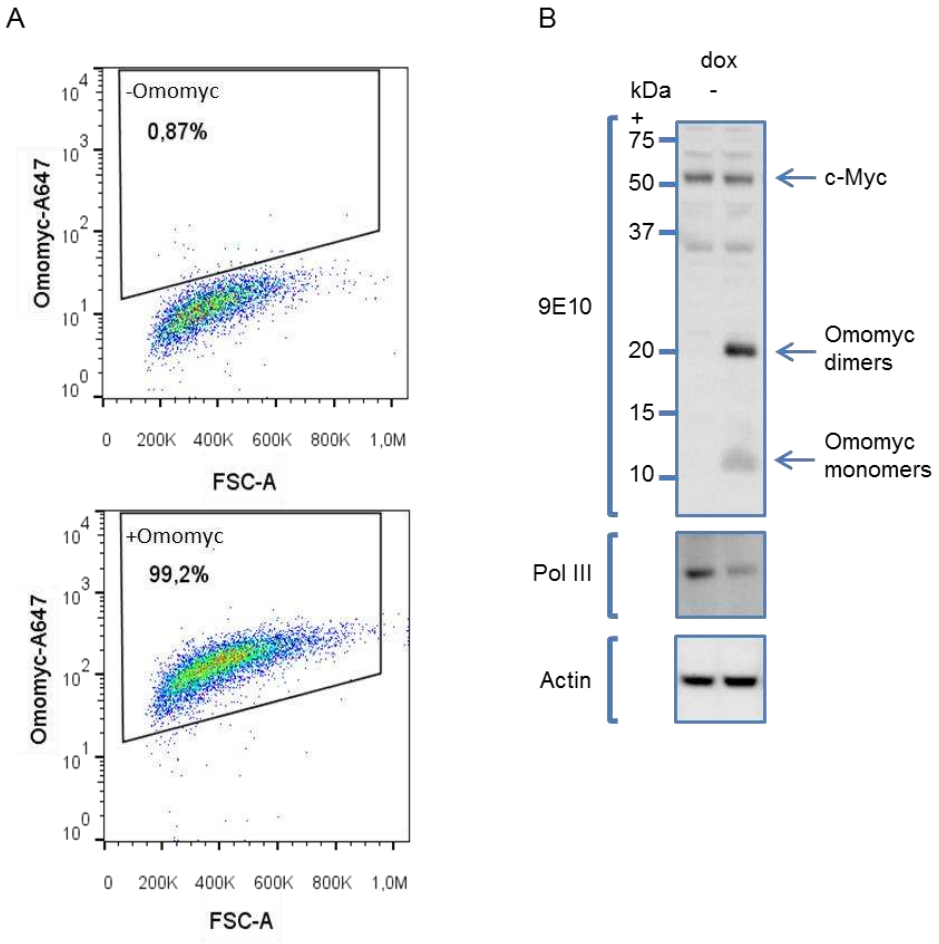

C

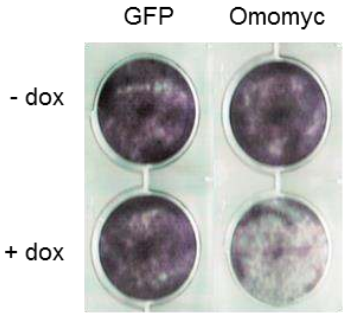
GFP
Omomyc
- dox
+ dox

D

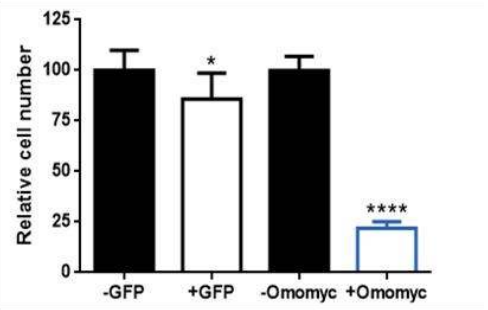
Relative cell number
125
100
75
50
25
0
*
****
-GFP
+GFP
-Omomyc
+Omomyc

E

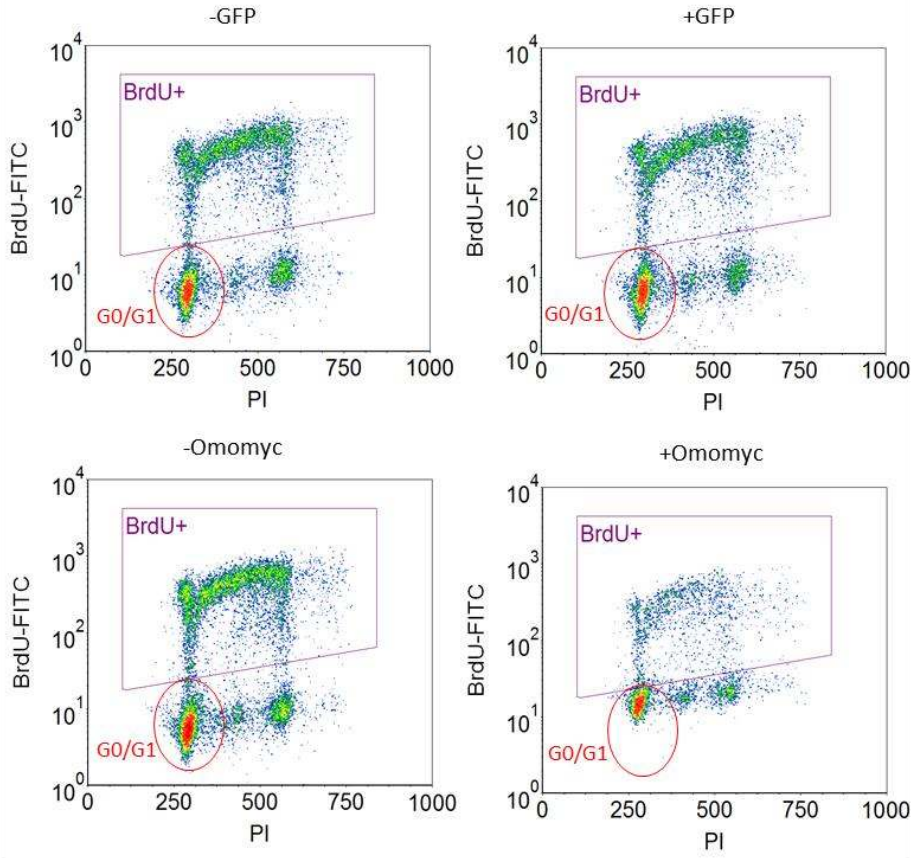
-GFP
+GFP
-Omomyc
+Omomyc
BrdU+
G0/G1
BrdU-FITC
PI
0
250
500
750
1000

F

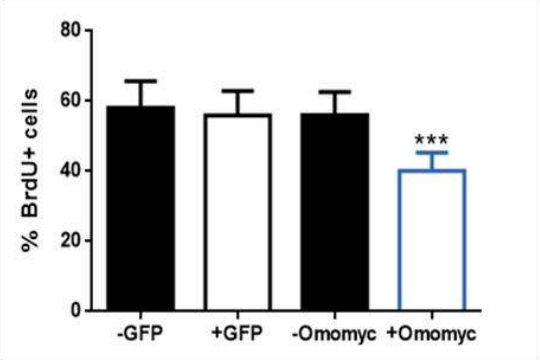
% BrdU+ cells
80
60
40
20
0
***
-GFP
+GFP
-Omomyc
+Omomyc

G

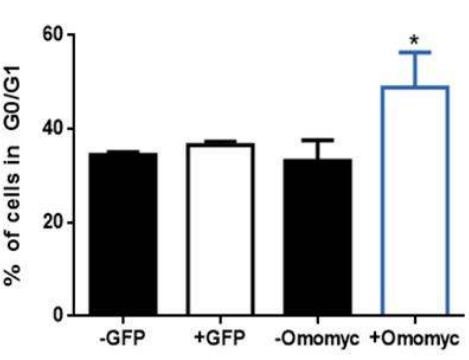
% of cells in G0/G1
60
40
20
0
*
-GFP
+GFP
-Omomyc
+Omomyc

Figure 23. Omomyc expression reduces proliferation of MDA-MB-231 cells *in vitro*.

A. Representative density plots of Omomyc levels in MDA-MB-231 pSLIK Omomyc cells untreated (-Omomyc) or treated with 0.6 μg/ml doxycycline for 3 days (+Omomyc) measured by flow cytometry.
B. Western blot of MDA-MB-231 pSLIK Omomyc cells untreated (-) or treated with 0.6 μg/ml doxycycline (dox) for 3 days (+) shows that, upon Omomyc expression, Pol III levels are reduced while Myc levels remain unchanged. 9E10: Anti-Myc antibody that recognizes both endogenous c-Myc and Omomyc.
C. Crystal violet staining of MDA-MB-231 pSLIK GFP (GFP) and MDA-MB-231 pSLIK Omomyc (Omomyc) cells untreated (-dox) or treated with 0.6 μg/ml doxycycline (+dox) for 6 days shows a clear reduction in the amount of Omomyc-expressing cells.
D. Cell counts of MDA-MB-231 pSLIK GFP and pSLIK Omomyc cells under the same conditions as C shows a significant but slight reduction in GFP-expressing cells and a very dramatic reduction in Omomyc-expressing cells after 6 days. Statistical significance was determined via two-tailed unpaired T test (*, $P > 0.05$; ****, $P < 0.0001$). Results shown represent mean + SD.
E. Representative density plots of MDA-MB-231 pSLIK GFP untreated cells (-GFP) or treated with 0.6 μg/ml doxycycline (+GFP) and MDA-MB-231 pSLIK Omomyc untreated cells (-Omomyc) or treated with 0.6 μg/ml doxycycline (+Omomyc) for 3 days measured by flow cytomerty. BrdU-FITC: Bromodeoxyuridine-Fluorescein isothiocyanate. PI: Propidium idodide.
F. % of BrdU-positive MDA-MB-231 cells from E shows a clear reduction in the amount of BrdU+ cells in the Omomyc-expressing population after 3 days. Statistical significance was determined via two-tailed unpaired T test (***, $P < 0.001$). Results shown represent mean + SD.
G. % of G0/G1 MDA-MB-231 cells from E shows an arrest in that phase of the cell cycle in Omomyc-expressing cells. Statistical significance was determined via two-tailed unpaired T test (*, $P < 0.05$). Results shown represent mean + SD.

2.3 Omomyc impairs the capacity of MDA-MB-231 cells to induce angiogenesis *in vitro*

Given that Myc is a pro-angiogenic factor and that angiogenesis is a key aspect in metastasis, we analyzed the capacity of MDA-MB-231 cells to induce angiogenesis after Omomyc expression and compared it to that of untreated or GFP-expressing cells. We collected the conditioned media of pSLIK GFP and pSLIK Omomyc MDA-MB-231 cells treated with or without doxycycline for 3 days. To correct for the reduced growth rate observed upon Omomyc treatment, 50% more cells were plated for the Omomyc-expressing cells, so that at the time of media collection the final number of total cells per well was the same. Conditioned media were added to human umbilical vein endothelial cells (HUVEC) seeded in Matrigel-coated wells and, 6 hours later, tube formation was quantified. Cells exposed to conditioned media from Omomyc-expressing cells presented a clear impairment in tube formation (Figure 24A),

demonstrating that Omomyc reduces the capacity of MDA-MB-231 cells to induce angiogenesis. To quantify the extent of angiogenesis inhibition, the number of nodes, junctions, segments, and branches, plus total length, total branching length and total segments length of tubes were quantified as previously described (Lee et al. 2014), showing a very significant reduction in all of them when HUVEC cells were exposed to conditioned media from Omomyc-expressing cells but not in the other controls (Figure 24B).

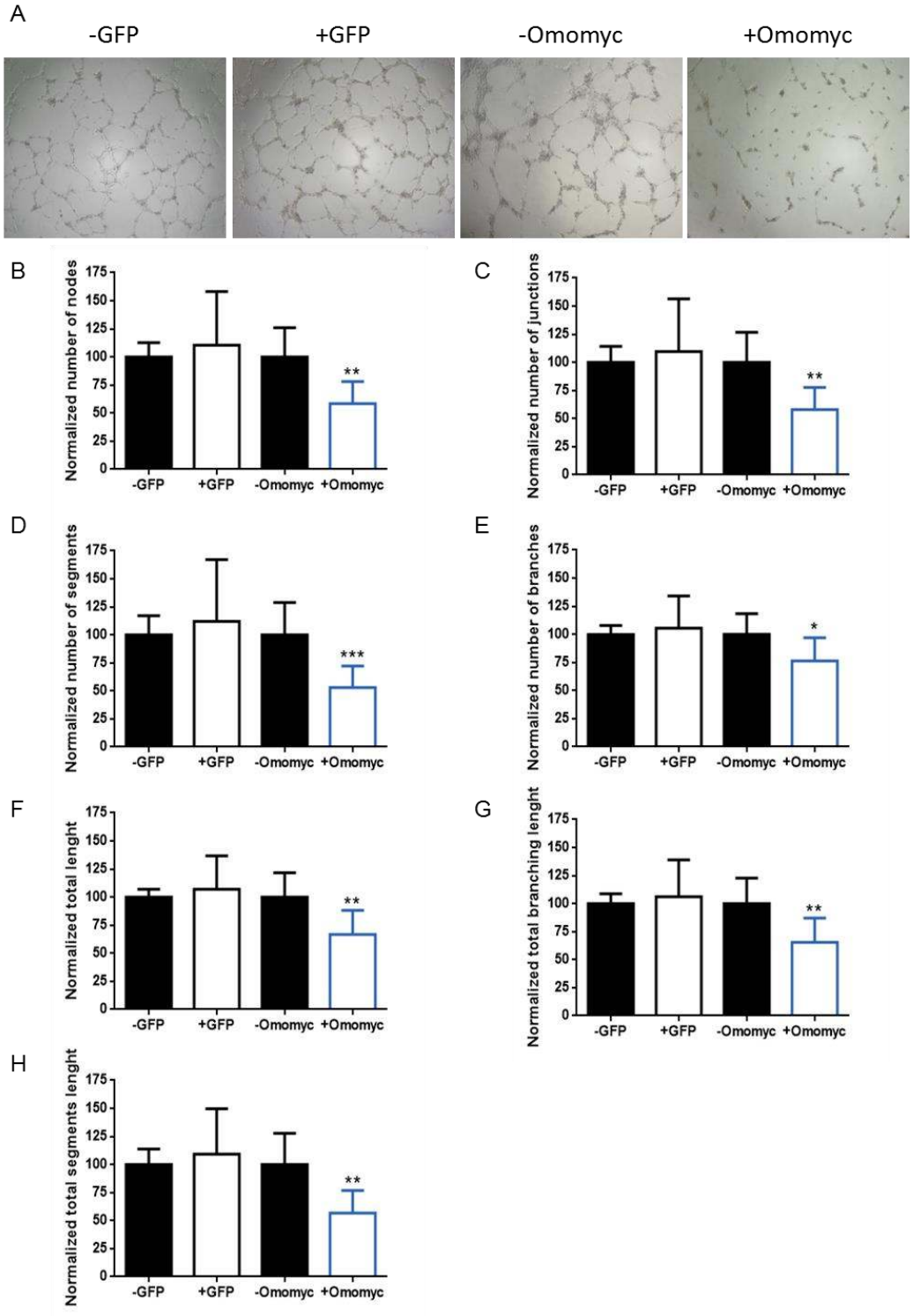

Figure 24. Omomyc reduces the capacity of MDA-MB-231 cells to induce angiogenesis.

A. Representative images of HUVEC cells 6 hours after addition of conditioned media from MDA-MB-231 pSLIK GFP cells untreated (-GFP) and treated with 0.6 µg/ml doxycycline for 3 days (+GFP) and from MDA-MB-231 pSLIK Omomyc cells untreated (-Omomyc) and treated for 3 days with 0.6 µg/ml doxycycline (+Omomyc).

B-H. Quantification of tube formation in HUVEC cells from A. Number of nodes (B), number of junctions (C), number of segments (D), number of branches (E), total length (F), total branching length (G) and total segments length (H) are reduced in cells exposed to conditioned media from Omomyc-expressing cells. Statistical significance was determined via two-tailed unpaired T test (*, P < 0.05; **, P < 0.01; ***, P <0 .001). Results shown represent mean + SD.

2.4 Omomyc reduces the metastatic features of breast cancer cells *in vitro*

To test the capacity of Omomyc to affect the metastatic phenotype of breast cancer cells, we conducted three different experiments in MDA-MB-231 pSLIK GFP and pSLIK Omomyc cells

The first experiment was a wound healing assay, to test the capacity of cells to perform directional migration. We created a gap in a monolayer of confluent cells that had been with or without doxycycline for 3 days, and followed its closure over time. After 12 hours, cells expressing Omomyc showed a delay in the closure of the gap (Figure 25A and B). Of note, even though no significant differences in cell number are observed after only 12 hours of Omomyc expression, cells were counted after the experiment and the percentage of wound area was corrected accordingly for both GFP and Omomyc-expressing cells.

The second experiment was a Boyden chamber migration assay, to test the ability of cells to migrate in response to nutrients. Untreated cells or pre-treated with doxycycline were placed inside a hollow plastic chamber with medium containing 0.5% FBS, sealed at one end with a dark porous membrane. This chamber was suspended over a larger well which contained medium with 10% FBS, which acts as a chemoattractant, and cells were allowed to migrate for 24h. Migrated cells were then stained with a fluorescent dye, and counted. Strikingly, the capacity of cells to migrate was reduced by 50% when Omomyc was expressed (Figure 25C and D).

Once again, the number of migrated cells was corrected to take into account the slight difference in proliferation rate (over the course of 24h) between GFP and Omomyc-expressing cells.

Finally, in order to test the invasive capacity of cells to migrate through an extracellular matrix (ECM), we made use of a Boyden chamber assay like the one described above,

with the difference that the porous membrane was coated with a layer of Matrigel, which mimics the ECM. To be able to migrate through the membrane, cells need to secrete proteolitic enzymes, as metastatic cells do *in vivo* to reach the bloodstream or the lymphatic system. Under these conditions, Omomyc-expressing cells showed a more dramatic 80% of reduction in their capacity to invade (Figure 25E and F).

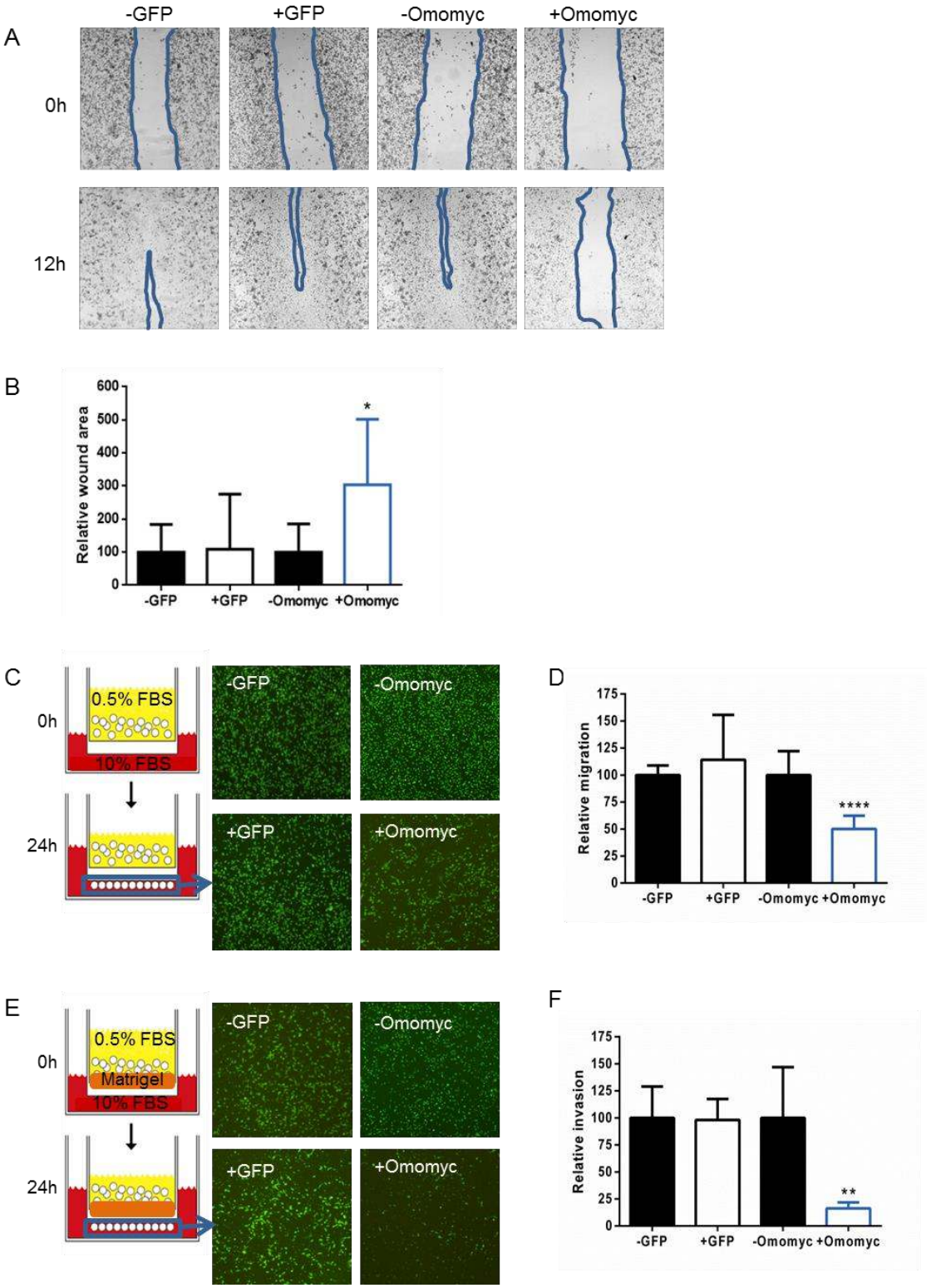

Figure 25. Omomyc reduces the metastatic phenotype of MDA-MB-231 cells *in vitro*.

A. Representative images of a wound healing assay at 0h (onset) and 12h (endpoint) with the approximate area of the wound delimited by a blue line, showing a bigger wound area in Omomyc-expressing cells at endpoint.
B. Relative wound area at endpoint, corrected for the total cell number. Statistical significance was determined via two-tailed Mann-Whitney test (*, $P < 0.05$). Results shown represent mean + SD.
C. Schematic representation of Boyden chamber assay and representative images of fluorescently labeled cells after 24 hours of migration. Fewer cells reach the other side of the membrane when expressing Omomyc.
D. Quantification of migrated cells from C corrected for the total cell number. Statistical significance was determined via two-tailed unpaired T test (****, $P < 0.0001$). Results shown represent mean + SD.
E. Schematic representation of Matrigel-coated Boyden chamber assay and representative images of fluorescently labeled cells after 24 hours of invasion. Fewer cells reach the other side of the membrane when expressing Omomyc.
F. Quantification of migrated cells from E corrected for the total cell number. Statistical significance was determined via two-tailed unpaired T test (**, $P < 0.01$). Results shown represent mean + SD.

Taken together, these results demonstrate that Omomyc can reduce several aspects of the metastatic phenotype of the highly invasive MDA-MB-231 cells. In order to verify if this was also true for other metastatic breast cancer cell lines, Boyden chamber migration experiments were performed in: an additional highly metastatic cell line (BT-549) and two poorly metastatic cell lines (MCF7 and Cal51). Even though the ability of the cells to migrate was very different among cell lines, Omomyc expression reduced their migratory capacity by approximately 50% in all cases (Figure 26 A-F), demonstrating that this feature is not restricted to MDA-MB-231 cells. A 24h or 48h time point was chosen for the analysis of the data depending on the migratory capacity of each cell line. Oddly, GFP expression or doxycycline induced some migration of Cal51 cells after 48 hours (Figure 26D).The reasons for this are unclear.

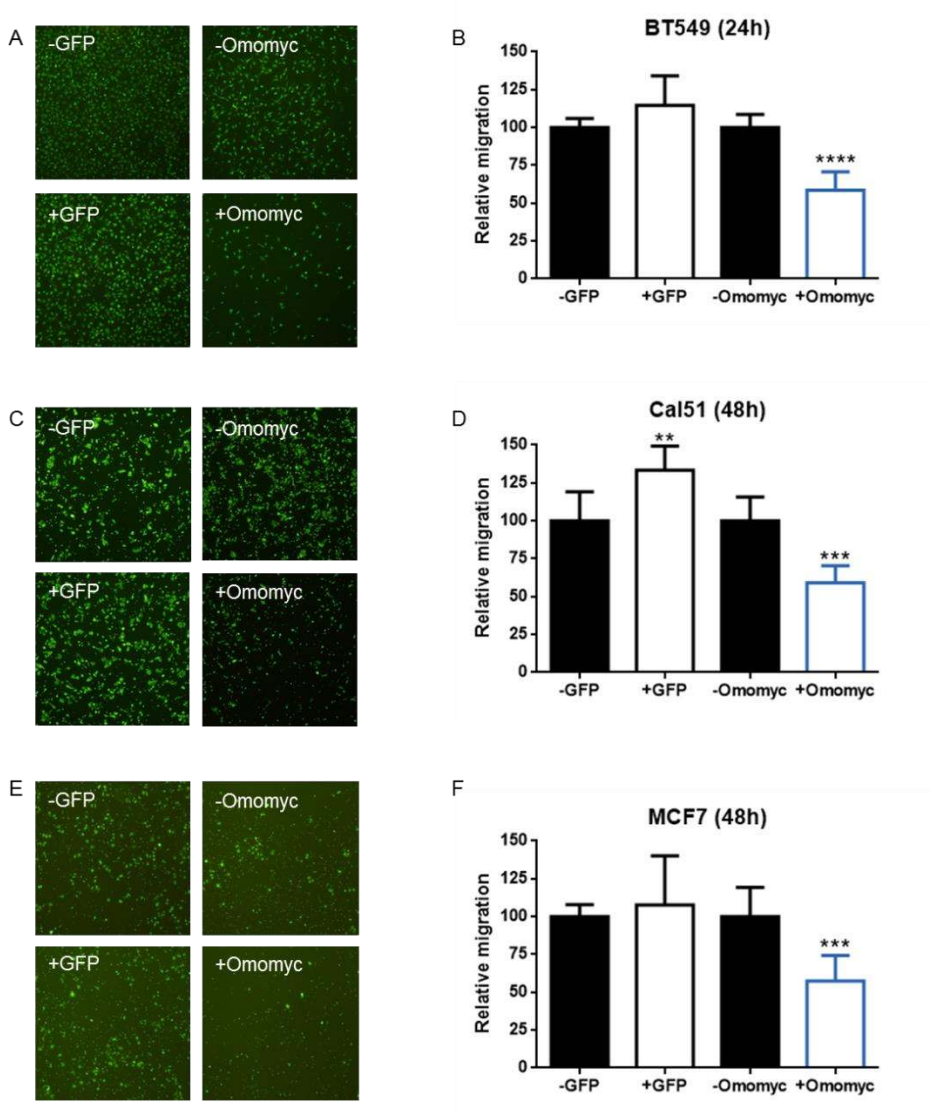

Figure 26. Omomyc reduces migration of BT-549, Cal51 and MCF7 cells *in vitro*.

A. Representative images of fluorescently labeled BT-549 cells after 24 hours of migration. Fewer cells reach the other side of the membrane when expressing Omomyc.
B. Quantification of migrated BT-549 cells corrected for the total cell number. Statistical significance was determined via two-tailed unpaired T test (****, P < 0.0001). Results shown represent mean + SD.
C. Representative images of fluorescently labeled Cal51 cells after 48 hours of migration. Fewer cells reach the other side of the membrane when expressing Omomyc.
D. Quantification of migrated Cal51 cells corrected for the total cell number. Statistical significance was determined via two-tailed unpaired T test (**, P < 0.01; ***, P < 0.001). Results shown represent mean + SD.
E. Representative images of fluorescently labeled MCF7 cells after 48 hours of migration. Fewer cells reach the other side of the membrane when expressing Omomyc.
F. Quantification of migrated MCF7 cells corrected for the total cell number. Statistical significance was determined via two-tailed unpaired T test (***, P<0.001). Results shown represent mean + SD.

2.5 Omomyc expression reduces the growth of primary mammary tumors *in vivo* in a xenograft orthotopic model

To test the effect of Omomyc expression *in vivo*, we used an aggressive and highly metastatic variant of the MDA-MB-231 cells. This variant, called LM2-4175, was selected for its tropism to the lung after *in vitro* expansion of lung metastases originated from intracardiac inoculation of MDA-MB-231 cells into BALB/c nude mice (Minn et al. 2005). These cells grow faster in the mammary fat pad compared to parental MDA-MB-231 cells, have comparable abilities to metastasize to bone and present an enhancement in lung metastasis after orthotopic inoculation or tail vein injection. They contain a triple-fusion protein reporter construct termed TGL encoding herpes simplex virus thymidine kinase 1, GFP and firefly luciferase (Ponomarev et al. 2004).

LM2-4175 TGL cells were infected with the pSLIK Omomyc lentiviral construct and selected with hygromycin. Since there is no selection marker for TGL expression (the original cells were selected through cell sorting) and firefly luciferase expression could have changed after several passages and the transfection process, we performed a clonal selection *in vitro* to obtain an experimental system with high and uniform expression of luciferase for *in vivo* testing. Thirteen clones were generated and luciferase activity was measured in each of them. While 4 of the clones showed high levels of luciferase activity, 9 of them showed very low levels, demonstrating that the original population was highly heterogeneous in terms of luciferase activity (Figure 27A, Clonal sel. 1). The highest-expressing clone (clone 11) was expanded and used for the following *in vivo* inoculations. To confirm that they remained homogeneous with regards to luciferase activity, a second clonal selection was performed after several passages and all 12 clones obtained showed similar luciferase activity (Figure 13A, Clonal sel. 2). Omomyc expression in clone 11 (from now on c#11) was confirmed by Western blot and flow cytometry 3 days after the addition of doxycycline (Figure 27B and C). Three *in vitro* experiments were carried out to confirm that LM2-4175 cells responded to Omomyc expression in a similar fashion to the parental MDA-MB-231 cells. As expected, Omomyc expression dramatically impaired cell proliferation (Figure 27D) and reduced the capacity of the cells to migrate (Figu3re 27E) and invade (Figure 27F).

A

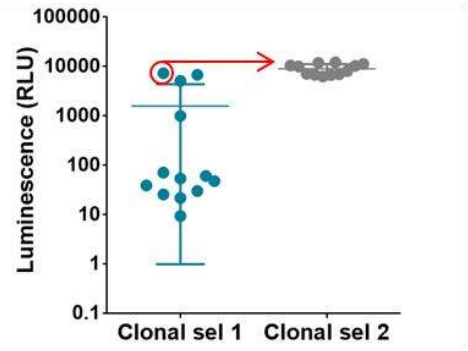
Luminescence (RLU)
100000
10000
1000
100
10
1
0.1
Clonal sel 1
Clonal sel 2

B

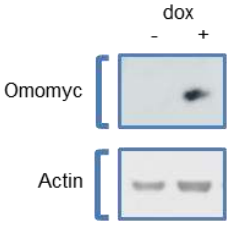
dox
-
+
Omomyc
Actin

C

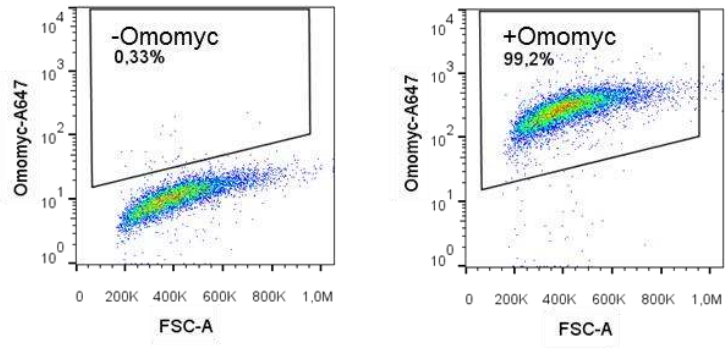
-Omomyc
0,33%
+Omomyc
99,2%
Omomyc-A647
FSC-A
0
200K
400K
600K
800K
1,0M

D

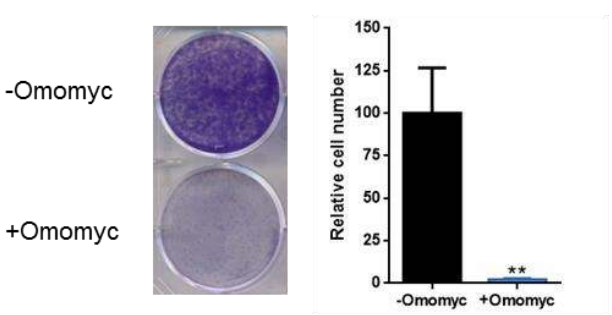
-Omomyc
+Omomyc
Relative cell number
150
125
100
75
50
25
0
**
-Omomyc
+Omomyc

E

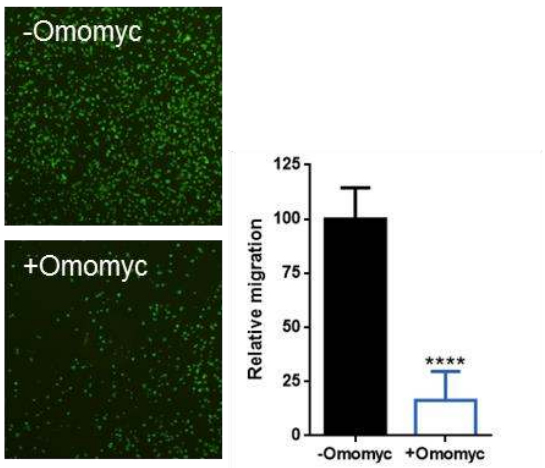
-Omomyc
+Omomyc
Relative migration
125
100
75
50
25
0
****
-Omomyc
+Omomyc

F

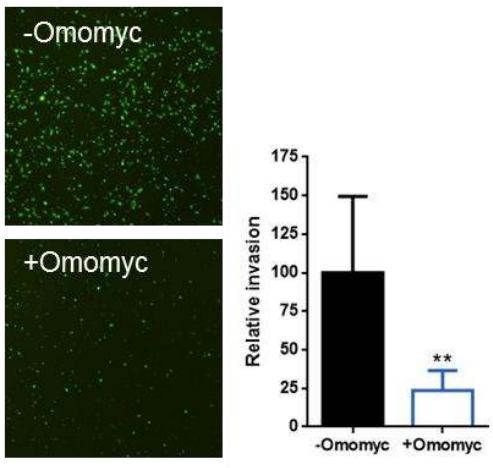
-Omomyc
+Omomyc
Relative invasion
175
150
125
100
75
50
25
0
**
-Omomyc
+Omomyc

Figure 27. Omomyc expression in LM2-4175 cells reduces proliferation and their capacity to migrate and invade.

A. Luciferase activity of clones obtained after two consecutive clonal selections of LM2-4175 TGL pSLIK Omomyc cells. Results shown represent mean ± SD. The clone used for the second selection is circled in red.
B. Western blot of LM2-4175 TGL pSLIK Omomyc c#11 cells untreated (-) or treated with 0.6 µg/ml doxycycline (dox) for 3 days (+) shows clear Omomyc expression in doxycycline-treated cells.
C. Flow cytometry analysis of LM2-4175 TGL pSLIK Omomyc c#11 cells untreated (-) or treated with 0.6 µg/ml doxycycline (dox) for 3 days (+) shows clear Omomyc expression in doxycycline-treated cells. A647: AlexaFluor 647
D. Crystal violet staining (left) and quantification (right) of LM2-4175 TGL pSLIK Omomyc c#11 untreated cells (-Omomyc) or treated with 0.6 µg/ml doxycycline (+Omomyc) after 6 days show a clear reduction in the amount of Omomyc-expressing cells. Statistical significance was determined via two-tailed unpaired T test (**, $P < 0.01$). Results shown represent mean + SD.
E. Representative images of fluorescently labeled cells after 24 hours of migration (left) and quantification of migrated cells corrected for the total cell number (right). Statistical significance was determined via two-tailed unpaired T test (****, P < 0 0001). Results shown represent mean + SD.
F. Representative images of fluorescently labeled cells after 24 hours of invasion (left) and quantification of migrated cells corrected for the total cell number (right). Statistical significance was determined via two-tailed unpaired T test (**, $P < 0.01$). Results shown represent mean + SD.

LM2-4175 TGL pSLIK Omomyc c#11 cells were then inoculated orthotopically in the mammary fat pad of 22 BALB/c nude mice. When tumors reached 100 mm^3, mice were randomized into two groups and treated with 5% sucrose (n = 11) or 2 g/L doxycycline diluted in 5% sucrose (n = 11) added to their drinking water for 4 weeks (Figure 14A). Sucrose is used to counteract the bitter taste of doxycycline so that mice drink enough water. Tumors from Omomyc-expressing mice showed a much slower growth rate than controls. That translated into a very significant difference in tumor volume just 5 days after treatment onset (Figure 28B), a difference that was maintained and increased until the experimental endpoint. At that stage, most of the control animals were close to the ethical endpoint (tumor volume ≥ 1500 mm^3), while none of the treated ones had reached that stage yet (Figure 28B and C). Tumor weight at the endpoint also reflected the change in tumor size, showing a very significant difference among groups (Figure 28D). Notably, Omomyc expression did not cause any sign of toxicity to the mice, which did not lose weight throughout the experiment, except for a drop during the first 2 days that was reverted at 4 days and was probably due to the change from pure water to water with doxycycline. Differences in weight starting from 9 days after treatment onset were mainly due to differences in tumor size (Figure 28E).

A


LM2-4175 TGL pSLIK Omomyc
Orthotopic inoculation
100 mm3
Sucrose / doxycycline
for 4 weeks
BALB/c nude

B

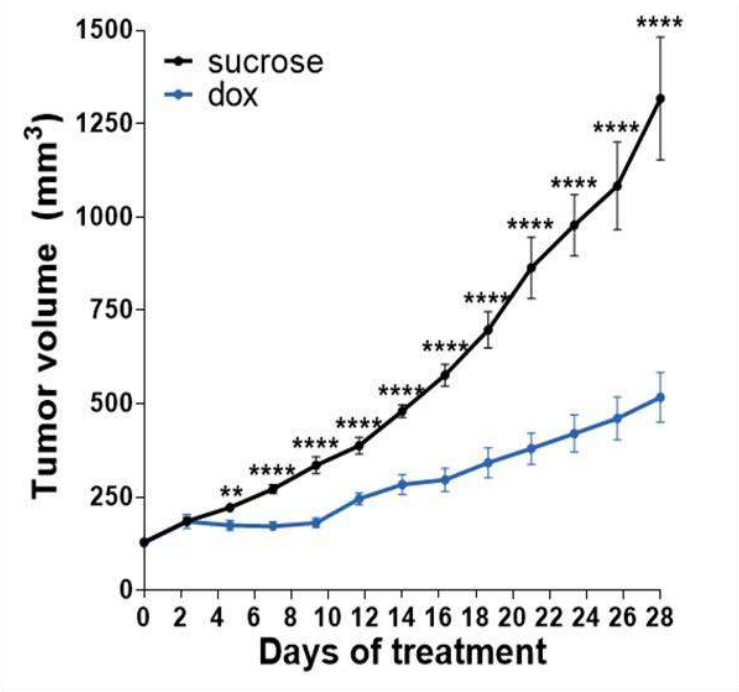
sucrose
dox
Tumor volume (mm3)
Days of treatment

C

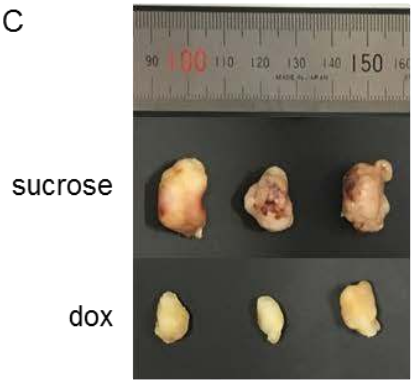
sucrose
dox

D

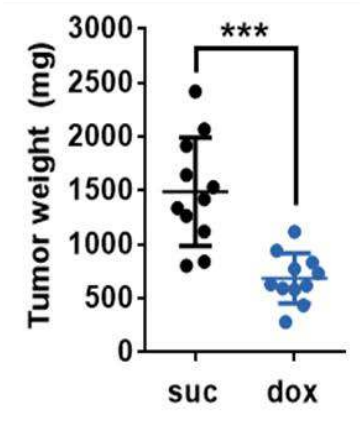
Tumor weight (mg)
suc
dox

E

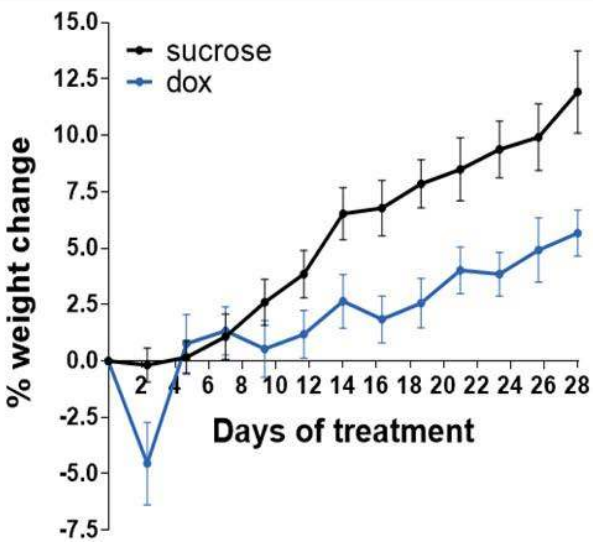
sucrose
dox
% weight change
Days of treatment

Figure 28. Omomyc expression reduces primary tumor growth in a cell-line derived orthotopic model. LM2-4175 TGL pSLIK Omomyc c#11 cells were inoculated into BALB/c nude females. When tumors reached 100 mm^3, mice were treated with 5% sucrose (sucrose/suc) and or with 2g/L doxycycline in 5% sucrose (dox) for 4 weeks.

A. Schematic representation of the mouse model.
B. Tumor volume of sucrose- and doxycycline-treated tumors for 4 weeks shows a clear difference among them. Statistical significance was determined via two-tailed Mann-Whitney test (**, $P < 0.01$; ****, $P < 0.0001$). Results shown represent mean ± SEM.
C. Image of 3 representative tumors from sucrose- and doxycycline-treated mice.
D. *Ex vivo* tumor weight shows a significant difference among control and treated mice. Statistical significance was determined via two-tailed unpaired T test (***, $P < 0.001$). Results shown represent mean ± SD.
E. Weight change in sucrose- and doxycycline-treated mice. Results shown represent mean ± SEM.

2.6 Omomyc expression impairs the growth of lung tumors established after tail vein injection of breast cancer cells

After these encouraging results and with the hypothesis that Omomyc would be also effective against metastasis *in vivo*, the therapeutic impact of Omomyc was challenged with a model of lung colonization in which LM2-4175 TGL pSLIK Omomyc c#11 cells were injected into the bloodstream of 20 BALB/c nude mice through the lateral tail vein (Minn et al. 2005). Lung colonization and tumor growth was then followed weekly by IVIS imaging. One week after inoculation, mice were randomized into two groups, control (n = 10) or treated (n = 10), receiving sucrose or doxycycline respectively for 5 consecutive weeks (Figure 29A). Importantly, Omomyc expression in the doxycycline-treated group did not induce any visible sign of toxicity, nor any weight loss (Figure 15B). Most strikingly, though, lung lesions in doxycycline-treated mice presented a much slower growth rate than those from control mice, showing statistical differences in bioluminescence already 1 week after treatment onset, which were maintained until the endpoint (Figure 29C). At the experimental endpoint, bioluminescence intensity in the lungs from treated mice was significantly lower than the ones from untreated controls (Figure 29D and E).

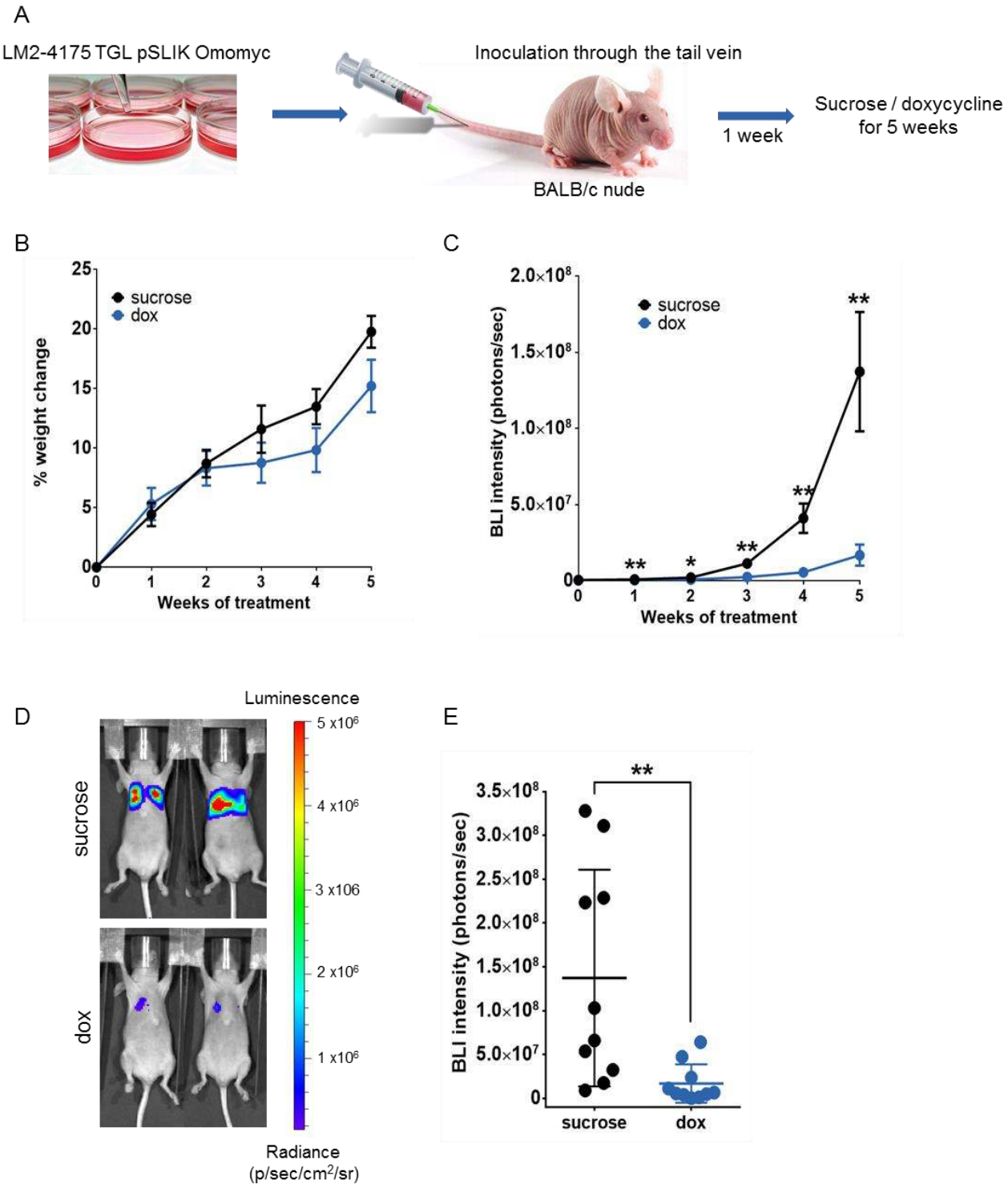

Figure 29. Omomyc expression reduces tumor appearance and growth in a cell-line derived model of lung colonization. LM2-4175 TGL pSLIK Omomyc c#11 cells were inoculated through the lateral tail vein into BALB/c nude females. 1 week later, they were treated with 5% sucrose (sucrose) or with 2g/L doxycycline in 5% sucrose (dox) for 5 weeks.

A. Schematic representation of the mouse model.
B. Weekly weight change in sucrose- and doxycycline-treated mice. Results shown represent mean ± SEM.

C. Luciferase activity measured weekly by IVIS imaging as bioluminescence (BLI) intensity, showing a significant difference between sucrose- and doxycycline-treated mice. Statistical significance was determined via two-tailed Mann-Whitney test (*, $P < 0.05$ **, $P < 0.01$). Results shown represent mean ± SEM.
D. Luminescence images representative of two sucrose-treated and two doxycycline-treated mice.
E. Luciferase activity at experimental endpoint measured by IVIS imaging as bioluminescence (BLI) intensity, showing a significant difference between sucrose- and doxycycline-treated mice. Statistical significance was determined via two-tailed Mann-Whitney test (**, $P < 0.01$). Results shown represent mean ± SD.

In order to analyze lung lesions individually, micro-computed tomography (µCT) images of the thoracic cavity were acquired for each mouse after 5 weeks of treatment. Lung tumors were counted and their volume calculated, showing that Omomyc expression significantly reduced both their number (Figure 30A, B and C) and volume (Figure 30A, B and D), resulting in a significant reduction of the total tumor burden per mouse (Figure 30E).

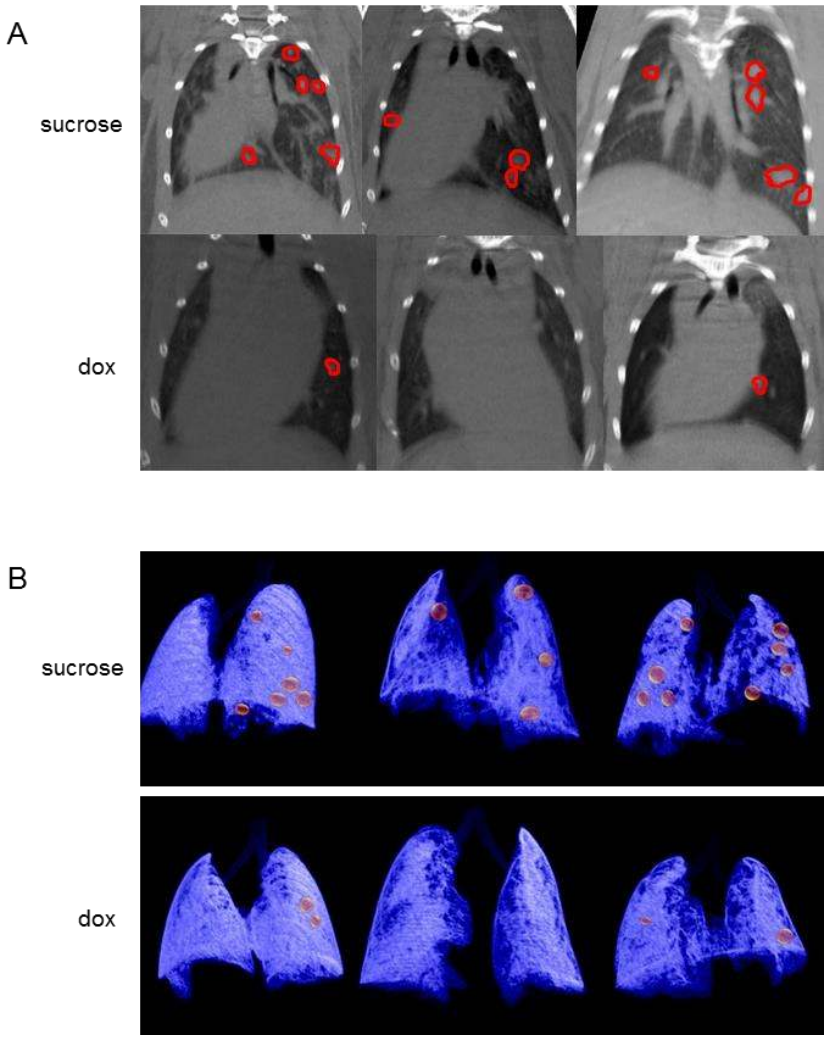

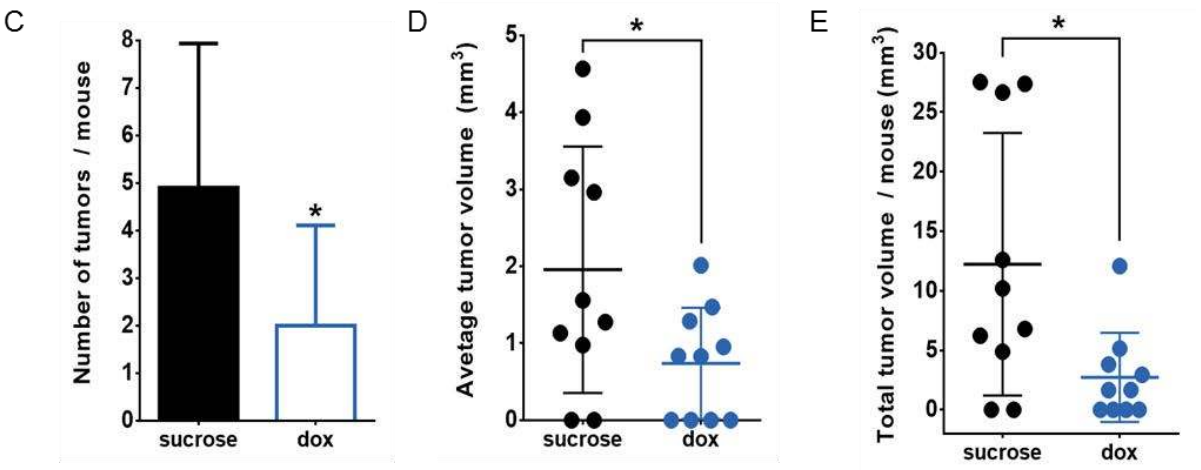

Figure 30. Omomyc expression reduces tumor number and size in a cell-line derived model of lung colonization. LM2-4175 TGL pSLIK Omomyc c#11 cells were inoculated through the lateral tail vein into BALB/c nude females. 1 week later, they were treated with 5% sucrose (sucrose) or with 2g/L doxycycline in 5% sucrose (dox) for 5 weeks.

A. Representative micro-computed tomography (μCT) images of three mice treated with sucrose and three mice treated with doxycycline for 5 weeks. Tumors are circled in red.
B. Renders of the lungs of three representative mice from sucrose-treated and doxycycline-treated (dox) groups obtained from μCT data. Healthy lung tissue is shown in blue and tumors in red.
C. Number of tumors in the lungs of sucrose- and doxycycline-treated mice counted from μCT images. Statistical significance was determined via two-tailed unpaired T test (*, $P < 0.05$). Results shown represent mean + SD.
D. Average tumor volume per mouse in the lungs of sucrose- and doxycycline-treated mice measured from μCT images. Statistical significance was determined via two-tailed unpaired T test (*, $P < 0.05$). Results shown represent mean ± SD.
E. Total tumor volume per mouse in the lungs of sucrose- and doxycycline-treated mice measured from μCT images, obtained from the sum of all individual tumors. Statistical significance was determined via two-tailed Mann-Whitney test (*, $P < 0.05$). Results shown represent mean ± SD.

2.7 Omomyc expression causes regression of established metastases after primary tumor resection

To assess the effect of Omomyc in a model where cells metastasize starting from the primary tumor site, LM2-4175 TGL pSLIK Omomyc c#11 cells were inoculated orthotopically in the mammary fat pad of BALB/c nude mice until primary tumors established and grew. 8 to 10 weeks later, they were surgically resected to mimic the standard clinical procedure for human patients. When metastases were detected by bioluminescence in secondary organs, mice were treated for 12 weeks with sucrose or doxycycline (Figure 31A). During the whole experiment, tumor and metastatic growth were followed weekly by IVIS imaging. Unfortunately, out of 50 mice inoculated, only

12 developed stable metastases and could be added to one of the groups. Despite the small number of animals per group, though, a clear difference was observed: the majority of sucrose-treated mice showed sustained growth of established metastases, while most of doxycycline-treated mice actually showed metastatic regression (Figure 16B, C and D). More in detail, from the sucrose-treated group, 4 out of 6 mice showed sustained growth, 1 showed metastasis stabilization and 1 showed spontaneous regression. It should also be noted that 2 of the sucrose-treated mice had to be euthanized before the experimental endpoint, at 3 and 6 weeks, due to metastatic burden (Figure 31B and Table 4). From the doxycycline-treated group, instead, none of the mice showed clear progression, 1 out of 6 mice showed fluctuating bioluminescence levels, but the other 5 showed clear regression, and in 4 of these we even observed complete eradication of metastasis. The difference in bioluminescence from treatment onset until experimental endpoint was calculated for both groups and was significantly different. The average was positive in the control group, indicating metastatic growth, and negative in the treated one, indicating metastatic regression (Figure 31D). After *ex vivo* analysis of the mice, control animals presented an average of 4.3 metastases, compared to 0.3 in treated mice (Table 2). Metastases in sucrose-treated mice were found in the pancreas (3 mice), liver (2), lungs (2), intestine (2), brain (1), spleen (1), diaphragm (1), several in the lymph nodes and other unidentified metastatic nodules. The only two metastases found in Omomyc-expressing mice were located in the skin, close to the upper mammary chain, and in the peritoneum, close to the location of the original primary tumor (Figure 31E). Weight was stable in mice receiving doxycycline, while sucrose-treated animals showed weight gain that later stabilized (Figure 31F).

A

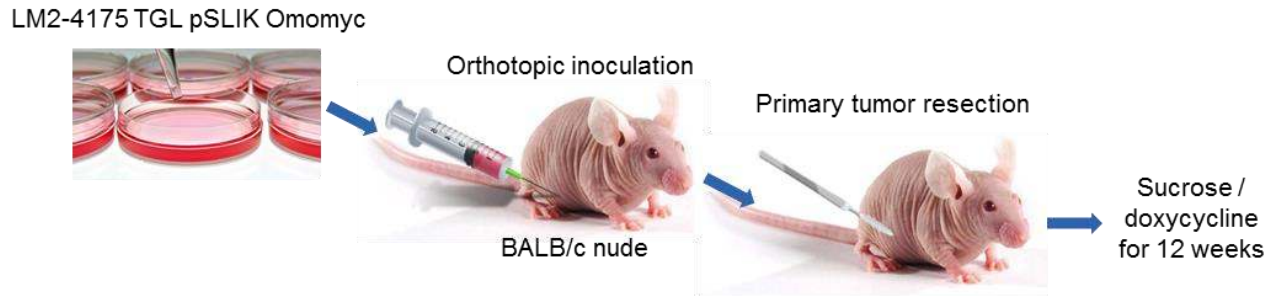
LM2-4175 TGL pSLIK Omomyc
Orthotopic inoculation
BALB/c nude
Primary tumor resection
Sucrose / doxycycline for 12 weeks

B

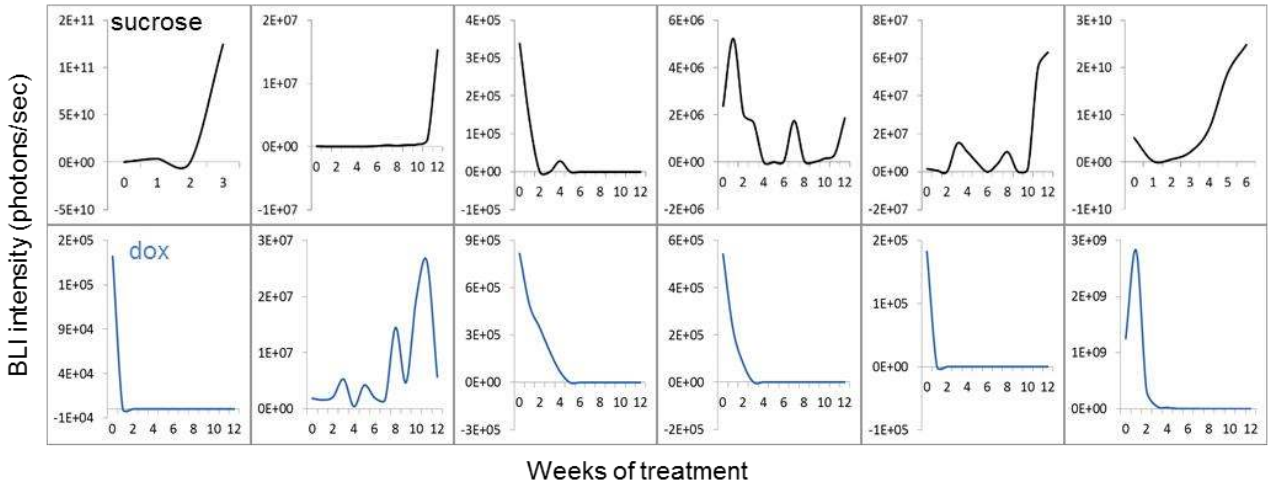
sucrose
dox
BLI intensity (photons/sec)
Weeks of treatment

C

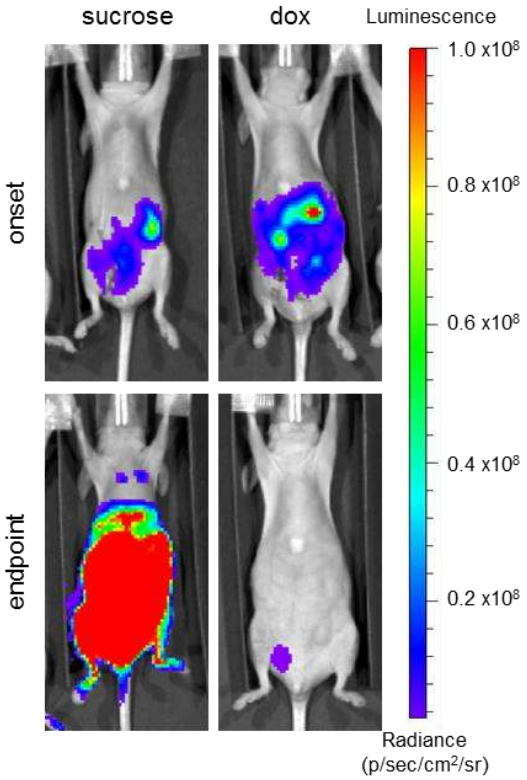
sucrose
dox
Luminescence
1.0 x10⁸
0.8 x10⁸
0.6 x10⁸
0.4 x10⁸
0.2 x10⁸
onset
endpoint
Radiance (p/sec/cm²/sr)

D

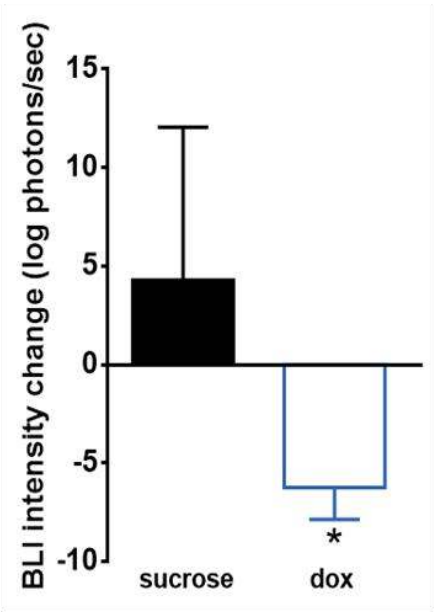
BLI intensity change (log photons/sec)
15
10
5
0
-5
-10
*
sucrose
dox

E

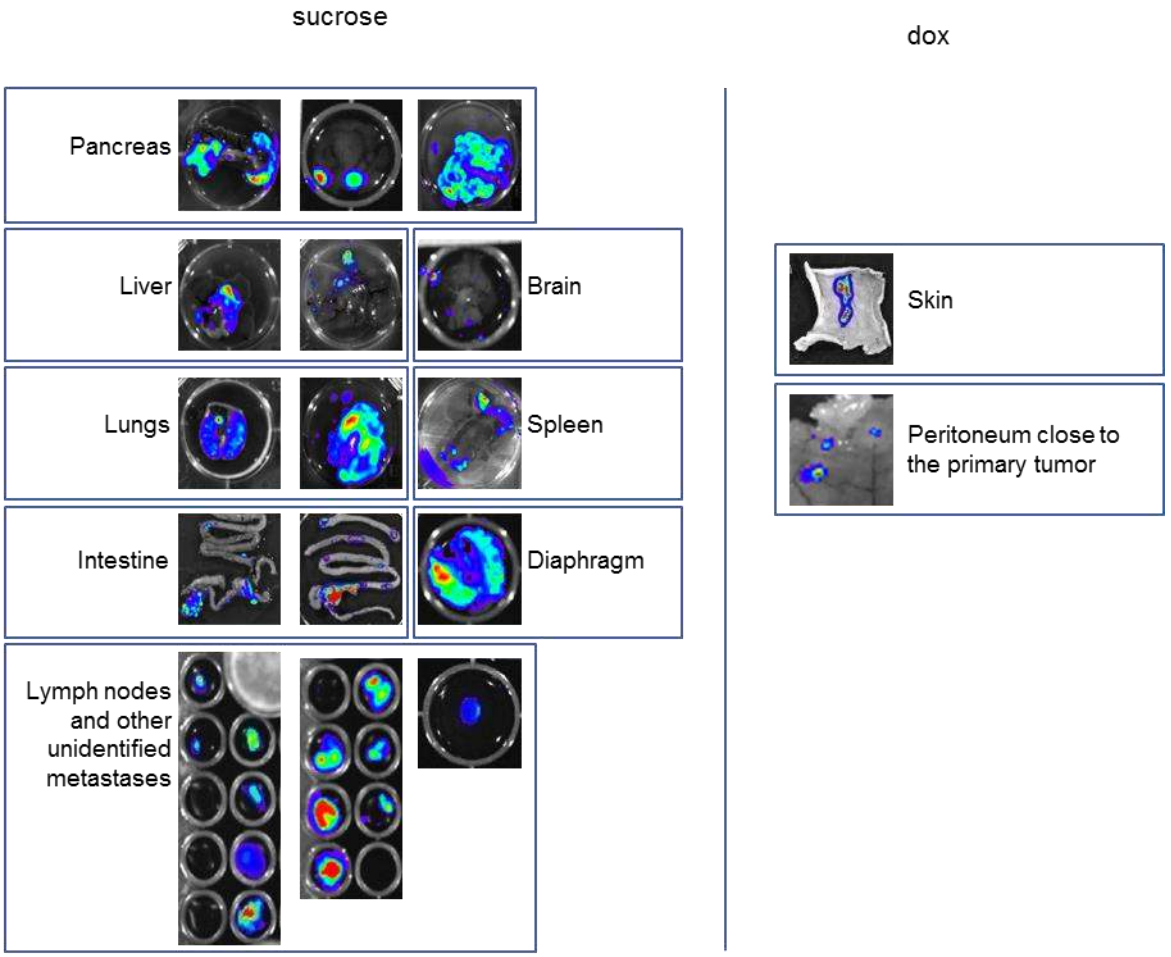

F

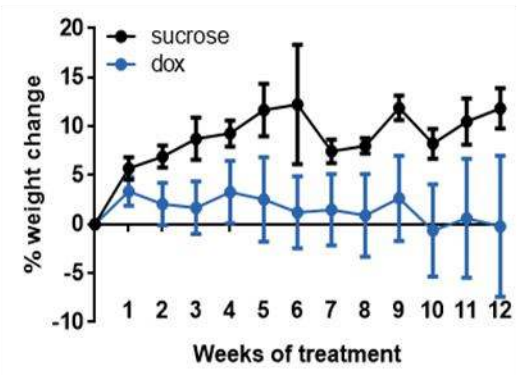

Figure 31. Omomyc expression induces metastasis regression in a cell-line derived model of breast cancer metastasis. LM2-4175 TGL pSLIK Omomyc c#11 cells were inoculated into BALB/c nude females. After 8-10 weeks, primary tumors were surgically resected and mice were treated with 5% sucrose (sucrose) or with 2 g/L doxycycline in 5% sucrose (dox) for 12 weeks.

A. Schematic representation of the mouse model.
B. Luciferase activity measured by IVIS imaging as bioluminescence (BLI) intensity in individual mice treated with sucrose (top panels, black lines) and doxycycline (bottom panels, blue lines).

C. Luminescence images representative of a sucrose-treated and a doxycycline-treated mouse at onset and endpoint show metastatic growth and regression respectively.
D. Difference of bioluminescence (BLI) intensity between onset and endpoint in mice treated with sucrose or doxycycline shows metastatic growth and regression respectively. Statistical significance was determined via two-tailed unpaired T test (*, $P < 0.05$). Results shown represent mean + SD (sucrose) and mean - SD (dox).
E. Luminescence images of all metastases detected *ex vivo* in sucrose- and a doxycycline-treated mice.
F. Weekly weight change in sucrose- and doxycycline-treated mice. Results shown represent mean ± SEM.

	sucrose	dox
Required euthanasia	2/6 (33%)	0/6 (0%)
Presence of metastasis at endpoint	5/6 (83%)	2/6 (33%)
Sustained growth	4/6 (67%)	0/6 (0%)
Stabilization	1/6 (17%)	1/6 (17%)
Regression	1/6 (17%)	5/6 (83%)
Average metastases/mouse	4.3	0.3

Table 4. Summary of differences observed between metastasis-bearing mice treated with 5% sucrose (sucrose) or 2g/L doxycycline in 5% sucrose (dox) for 12 weeks.

2.8 Generation and characterization of a transgenic mouse model of metastatic breast cancer with inducible expression of Omomyc

Given the role of Myc in regulating the tumor microenvironment and components of the immune system, we thought that the effect of Omomyc should also be evaluated in an immune competent mouse model. For this reason we generated a genetically engineered mouse model of metastatic breast cancer with inducible expression of Omomyc. To do so, the well characterized *TRE-Omomyc;CMV-rtTA* mouse, in which Omomyc is expressed in most tissues upon addition of doxycycline (Soucek et al. 2008; Soucek et al. 2013; Annibali et al. 2014), was crossed with the *MMTV-PyMT* mouse model of metastatic breast cancer (Guy et al. 1992). In these mice, PyMT expression in carrier females leads to the appearance of palpable mammary tumors as early as 5 weeks of age, and pulmonary metastases are found in almost all females by 13 weeks. *TRE-Omomyc;CMV-rtTA* mice were shipped from the University of California San Francisco (UCSF) and rederived through embryonic transference into pathogen-free foster mothers to comply with the Vall d'Hebron Research Institute

(VHIR) housing requirements. Since *TRE-Omomyc;CMV-rtTA* mice were generated in a mixed C57BL/6-FVB/N background and the *MMTV-PyMT* mice were generated in a pure FVB/N background, *MMTV-PyMT;TRE-Omomyc;CMV-rtTA* mice were backcrossed with pure FVB/N mice. After four generations, primary tumor growth and lung metastasis appearance of these new mice (n = 20) was compared with the original *MMTV-PyMT* mice (n = 14). Weekly measurements of primary tumor volumes showed no difference in tumor latency and growth (Figure 32A) and lung sections of 13 week old, tumor-bearing mice showed no difference in metastatic burden either (Figure 32B).

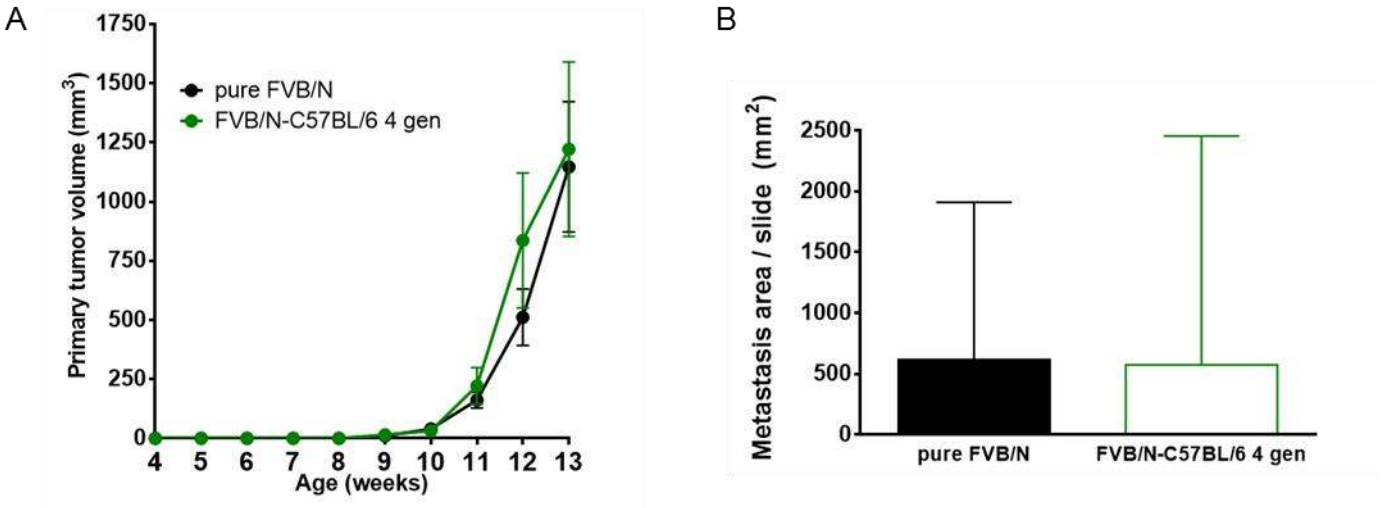

Figure 32. No differences in primary tumor and lung metastasis volumes are observed between *MMTV-PyMT* mice (pure FVB/N) and *MMTV-PyMT* mice backcrossed with *TRE-Omomyc;CMV-rtTA* mice for 4 generations (FVB/N-C57BL/6 4 gen).

A. Primary tumor volumes of 'pure FVB/N' and 'FVB/N-C57BL/6 4 gen' mice from 4 to 13 weeks of age shows no significant differences among groups. Statistical significance was determined via two-tailed Mann-Whitney test. Results shown represent mean ± SEM.
B. Total metastasis area in lung sections of 13 week old of 'pure FVB/N' and 'FVB/N-C57BL/6 4 gen' mice shows no significant differences among groups. Statistical significance was determined via two-tailed Mann-Whitney test. Results shown represent mean + SD.

In parallel, to make sure that the *CMVrtTA* would not be a limiting factor in the mammary tissue, we also imported another mouse model with doxycycline-inducible expression of Omomyc from Cambridge University. In this other model, the reverse tetracycline transactivator (*rtTA*) is under the control of the *beta-actin* (*βactin*) promoter (Soucek et al. 2008; Parker et al. 2017). Since the background of these *TRE-Omomyc;βactin-rtTA* mice was pure FVB/N and the health report complied with VHIR requirements, mice were imported directly and crossed with *MMTV-PyMT* mice.

To determine the levels of Omomyc expression in both models, *MMTV-PyMT;TRE-Omomyc;CMV-rtTA and MMTV-PyMT;TRE-Omomyc;βactin-rtTA* females were treated

with doxycycline in their drinking water for 1 week. As negative controls, *MMTV-PyMT;TRE-Omomyc* mice were treated with doxycycline for 1 week and *MMTV-PyMT;TRE-Omomyc;CMV-rtTA* and *MMTV-PyMT;TRE-Omomyc;βactin-rtTA* mice were treated with sucrose. Mammary fat pad and lung samples were collected for detection of Omomyc by immunofluorescence (IF). Since pancreas was the tissue reported to express the highest levels of Omomyc ((Soucek et al. 2008) and Figure 33), pancreas was also collected for the analysis and samples from the original doxycycline-treated UCSF mice were used as positive controls.

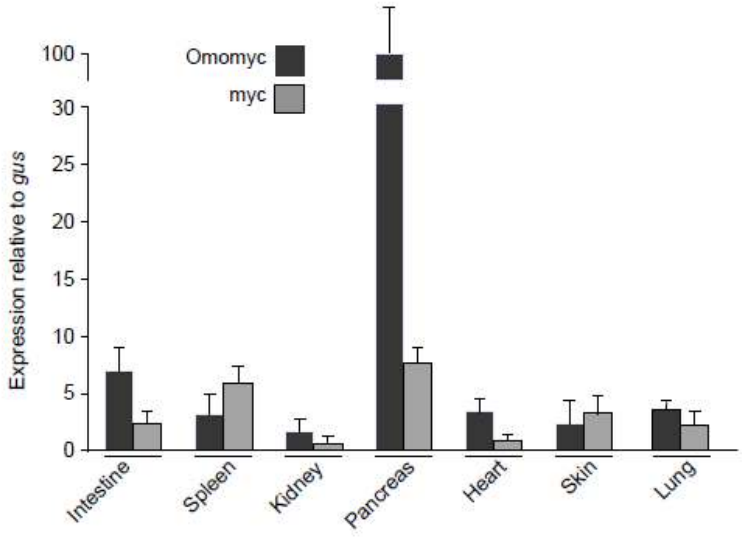

Figure 33 (Soucek et al. 2008)**.** Real-time PCR of Omomyc and c-Myc expression relative to GUS in various tissues of *TRE-Omomyc;CMV-rtTA* mice from UCSF treated with 2 g/L doxycycline in 5% sucrose.

TRE-Omomyc;CMV-rtTA mice from UCSF treated with doxycycline showed clear Omomyc positivity in the pancreas. *MMTV-PyMT;TRE-Omomyc* mice treated with doxycycline and *MMTV-PyMT:TRE-Omomyc;CMV-rtTA* mice treated with sucrose were negative for Omomyc in all tissues analyzed, as expected (Figure 34). In contrast, *MMTV-PyMT:TRE-Omomyc;CMV-rtTA* mice treated with doxycycline only showed Omomyc positivity in some cells of the pancreas, probably due to the fact that Omomyc in the mammary fat pad and the lungs is below the detection threshold of the IF. Surprisingly, *MMTV-PyMT;TRE-Omomyc;βactin-rtTA* mice treated with sucrose, showed Omomyc positivity in some cells of the mammary fat pad tumors, and in a few lung cells. In the pancreas, around 50% of the cells expressed high levels of Omomyc. Since *MMTV-PyMT;TREOmomyc* mice treated with doxycycline did not show any Omomyc positivity, the leaky expression observed is likely due to defects in the rtTA driven by the *βactin* promoter. Even so, *MMTV-PyMT;TRE-Omomyc;βactin-rtTA* mice

treated with doxycycline showed higher levels of Omomyc in the mammary fat pad, lungs, and pancreas. In the latter, almost 100% of the cells were positive for Omomyc expression.

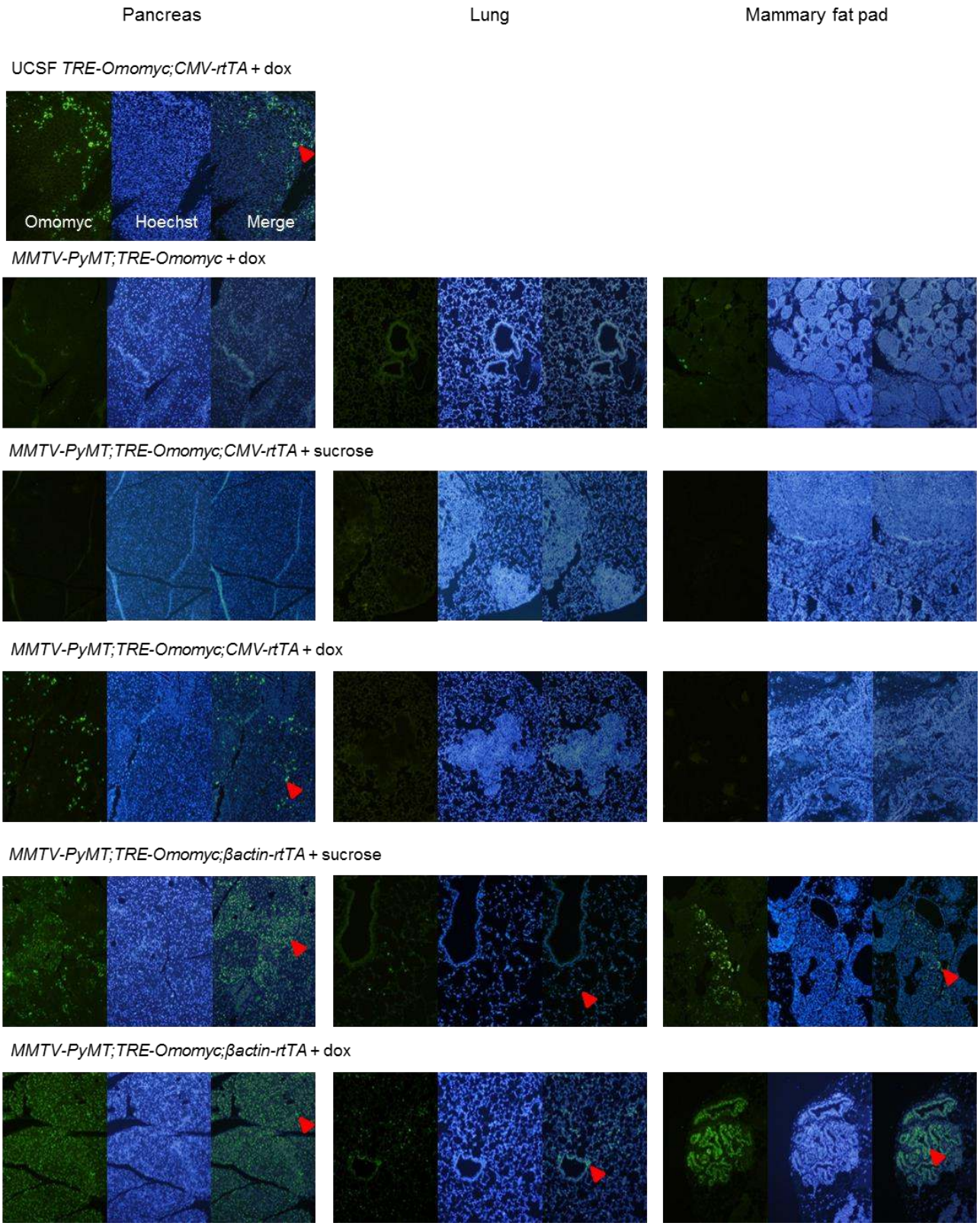

Figure 34. Omomyc immunofluorescence (IF) in pancreas, lung and mammary fat pad sections from *TRE-Omomyc;CMV-rtTA* mice from UCSF and *MMTV-PyMT;TRE-Omomyc*, *MMTV-PyMT;TRE-Omomyc;CMV-rtTA* and *MMTV-PyMT;TRE-Omomyc;βactin-rtTA* mice from VHIR treated with 5% sucrose (sucrose) or 2 g/L doxycycline in 5% sucrose (dox) for 1 week. Green staining shows Omomyc positivity and nuclei are shown in blue (Hoechst). Red arrowheads indicate positive cells in the merged image.

Intriguingly, besides the difference in the number of Omomyc-expressing cells observed among these models, it stood out that its subcellular localization was also different. While the Omomyc signal was clearly nuclear in the pancreas of *TRE-Omomyc;CMV-rtTA* mice from UCSF and *MMTV-PyMT;TRE-Omomyc;βactin-rtTA* mice, the signal in *MMTV-PyMT;TRE-Omomyc;CMV-rtTA* mice was nuclear and cytoplasmic, as seen by phase contrast and confocal microscopy (Figure 35A and B). In addition, the nuclear Omomyc levels in *TRE-Omomyc;CMV-rtTA* and *MMTV-PyMT;TRE-Omomyc;βactin-rtTA* mice were higher than in the *MMTV-PyMT;TRE-Omomyc;CMV-rtTA* mice (Figure 35B, intense green vs. turquoise). Given that Omomyc contains a nuclear localization signal (NLS) within its sequence, a possible explanation for the different subcellular localization could be that a mutation had occurred in this sequence. To test that hypothesis, DNA was extracted from tissue samples of *MMTV-PyMT;TRE-Omomyc;CMV-rtTA* and original *TRE-Omomyc;CMV-rtTA* mice from UCSF, and Omomyc was sequenced. The resulting sequences were aligned with the theoretical Omomyc sequence and no differences were found, discarding any mutation in the Omomyc sequence as the cause for the cytoplasmic localization and the lower nuclear levels observed in *MMTV-PyMT;TRE-Omomyc;CMV-rtTA* mice (Figure 35C). Of note, a silent mutation was found in the codon encoding Arginine 72 of Omomyc, which occurred in some samples from both *TRE-Omomyc;CMV-rtTA* from UCSF and *MMTV-PyMT;TRE-Omomyc;CMV-rtTA* mice (Figure 35D).

A

UCSF *TRE-Omomyc;CMV-rtTA*

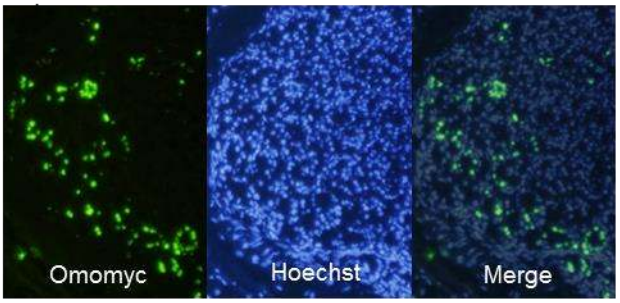

B

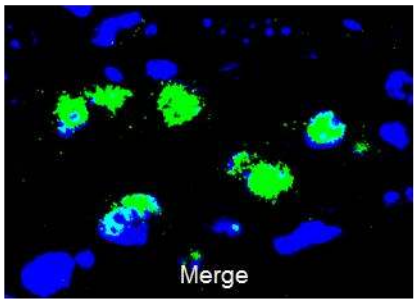

MMTV-PyMT;TRE-Omomyc;CMV-rtTA + dox

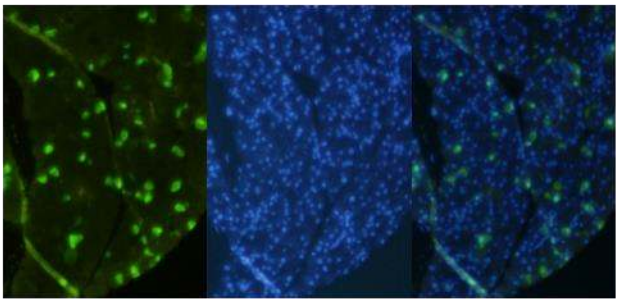

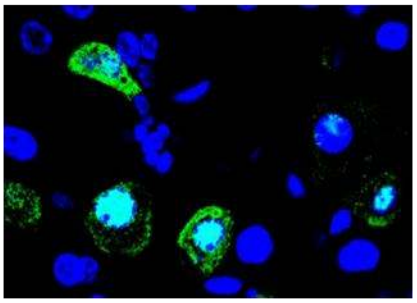

MMTV-PyMT;TRE-Omomyc;βactin-rtTA + dox

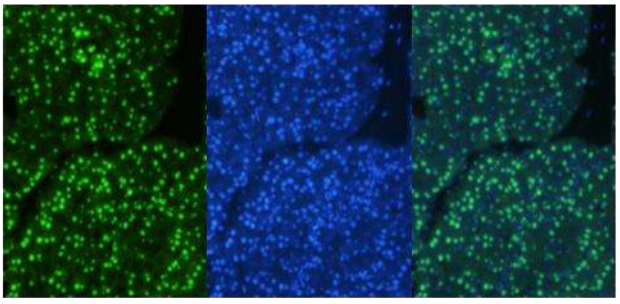

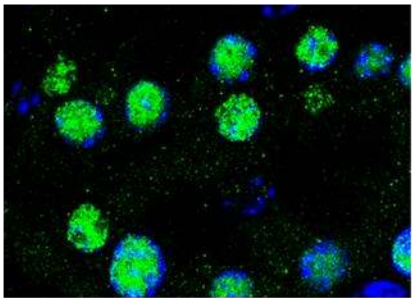

C

```
CLUSTAL multiple sequence alignment by MUSCLE (3.8)

Omomyc_sequence                ACCGAGGAGAATGTCAAGAGGCGAACACACAACGTCTTGGAGCGCCAGAGGAGGAACGAG
UCSF_TRE-Omomyc;CMV-rtTA       ACCGAGGAGAATGTCAAGAGGCGAACACACAACGTCTTGGAGCGCCAGAGGAGGAACGAG
MMTV-PyMT;TRE-Omomyc;CMV-rtTA  ACCGAGGAGAATGTCAAGAGGCGAACACACAACGTCTTGGAGCGCCAGAGGAGGAACGAG
                               ************************************************************

Omomyc_sequence                CTAAAACGGAGCTTTTTTGCCCTGCGTGACCAGATCCCGGAGTTGGAAAACAATGAAAAG
UCSF_TRE-Omomyc;CMV-rtTA       CTAAAACGGAGCTTTTTTGCCCTGCGTGACCAGATCCCGGAGTTGGAAAACAATGAAAAG
MMTV-PyMT;TRE-Omomyc;CMV-rtTA  CTAAAACGGAGCTTTTTTGCCCTGCGTGACCAGATCCCGGAGTTGGAAAACAATGAAAAG
                               ************************************************************

Omomyc_sequence                GCCCCCAAGGTAGTTATCCTTAAAAAAGCCACAGCATACATCCTGTCCGTCCAAGCAGAG
UCSF_TRE-Omomyc;CMV-rtTA       GCCCCCAAGGTAGTTATCCTTAAAAAAGCCACAGCATACATCCTGTCCGTCCAAGCAGAG
MMTV-PyMT;TRE-Omomyc;CMV-rtTA  GCCCCCAAGGTAGTTATCCTTAAAAAAGCCACAGCATACATCCTGTCCGTCCAAGCAGAG
                               ************************************************************

Omomyc_sequence                ACGCAAAAGCTCATTTCTGAAATCGACTTGTTGCGGAAACAAAACGAACAGTTGAAACAC
UCSF_TRE-Omomyc;CMV-rtTA       ACGCAAAAGCTCATTTCTGAAATCGACTTGTTGCGGAAACAAAACGAACAGTTGAAACAC
MMTV-PyMT;TRE-Omomyc;CMV-rtTA  ACGCAAAAGCTCATTTCTGAAATCGACTTGTTGCGGAAACAAAACGAACAGTTGAAACAC
                               ************************************************************

Omomyc_sequence                AAACTTGAACAGCTACGGAACTCTTGTGCGTAA
UCSF_TRE-Omomyc;CMV-rtTA       AAACTTGAACAGCTACGGAACTCTTGTGCGTAA
MMTV-PyMT;TRE-Omomyc;CMV-rtTA  AAACTTGAACAGCTACGGAACTCTTGTGCGTAA
                               ********************************
```

D

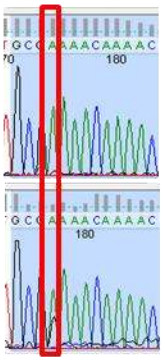

G>A

G>A/G

R72: CGG > CGA
Arg > Arg

Figure 35.Omomyc expression levels and subcellular localization in pancreatic cells is different among UCSF *TRE-Omomyc;CMV-rtTA*, *MMTV-PyMT;TRE-Omomyc;CMV-rtTA* and *MMTV-PyMT;TRE-Omomyc;βactin-rtTA* mice.

A. Fluorescence microscopy images of Omomyc detected by immunofluorescence (IF) in pancreas sections of UCSF *TRE-Omomyc;CMV-rtTA*, *MMTV-PyMT;TRE-Omomyc;CMV-rtTA* and *MMTV-PyMT;TRE-Omomyc;βactin-rtTA* mice treated 2 g/L doxycycline in 5% sucrose (dox) for 1 week. Green staining shows Omomyc positivity and nuclei are shown in blue (Hoechst).
B. Confocal images of Omomyc IF in the same mice and conditions as in A.
C. Sequence alignment of Omomyc amplified from genomic DNA extracted from UCSF *TRE-Omomyc;CMV-rtTA* and *MMTV-PyMT;TRE-Omomyc;CMV-rtTA* mice, compared with the theoretical Omomyc sequence (in green).
D. Sequences showing the silent mutation found in the codon encoding arginine 72 of Omomyc in both UCSF *TRE-Omomyc;CMV-rtTA* and *MMTV-PyMT;TRE-Omomyc;CMV-rtTA* mice.

In summary, two models of metastatic breast cancer with Omomyc expression were generated. The *MMTV-PyMT;TRE-Omomyc;CMV-rtTA* model showed inducible expression of Omomyc upon doxycycline addition to the drinking water of the mice, but the levels were low and the subcellular localization was not solely nuclear. Furthermore, Omomyc was below detection levels in the mammary fat pad or lungs of the mice, the main tissues that needed to be targeted. In contrast, the *MMTV-PyMT;TRE-Omomyc;βactin-rtTA* mice presented higher levels of Omomyc that were detectable in almost all cells of the pancreas and in some cells in the mammary fat pad and lungs upon doxycycline addition. However, those mice presented clear leakiness of Omomyc. Low Omomyc expression was also detected in some cells of the mammary fat pad and the lungs of mice that received sucrose. Therefore, since neither of the models was optimal and each of them presented advantages and disadvantages, we performed the *in vivo* studies using both.

2.9 Omomyc expression impairs primary tumor growth and metastasis formation in the *MMTV-PyMT* transgenic mouse model of breast cancer

In a prevention study, 5 week old *MMTV-PyMT;TRE-Omomyc;CMV-rtTA* female mice were treated with sucrose (n = 8) or doxycycline (n = 9) to induce expression of Omomyc before the appearance of primary tumors and lung metastases. Primary mammary tumors were palpable at 7-8 weeks of age and their diameter measurable by caliper at 10-11 weeks (Figure 36A). Consistent with the very low levels of Omomyc observed in this model, weekly tumor measures showed that, even though both groups

developed mammary tumors, the doxycycline-treated ones grew at a slower rate, but in a non-significant manner (Figure 36B). The treatment did not cause any toxicity and all mice gained weight (Figure 36C). Mice were euthanized at 13 weeks of age because some reached tumor sizes close to the ethical endpoint criteria. At the experimental endpoint, primary tumors from doxycycline-treated mice were smaller than the ones of sucrose-treated mice, but the difference was non-significant (Figure 36D).

Lungs were collected and metastases were quantified in serial cuts stained with hematoxylin and eosin (H&E). No differences in metastatic burden were observed after 13 weeks of sucrose or doxycycline treatment. Once again, no statistical differences were found in the number and area of metastases per mouse (Figure 36E and F), which translated into no statistical differences in total metastasis area / slide between control and treated animals (Figure 36G).

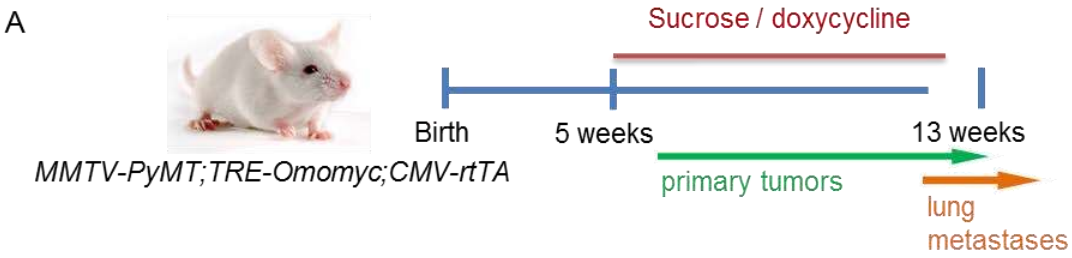

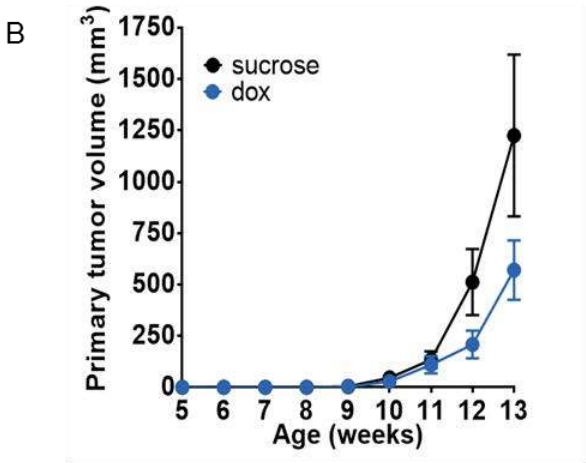

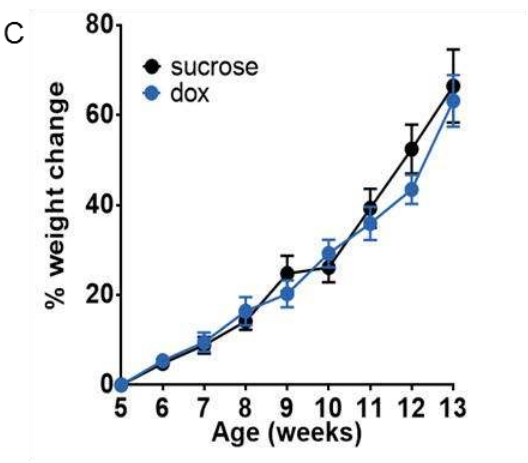

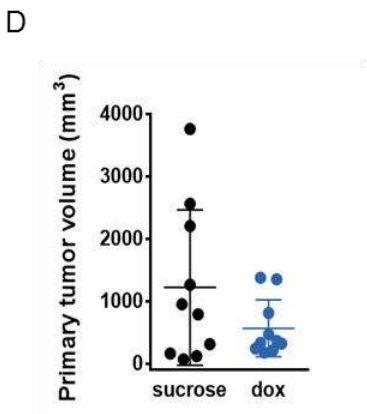

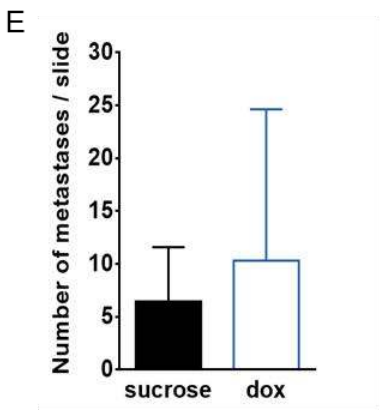

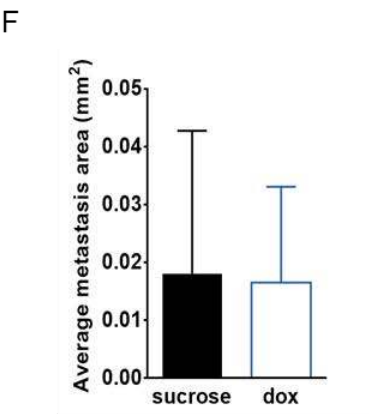

G

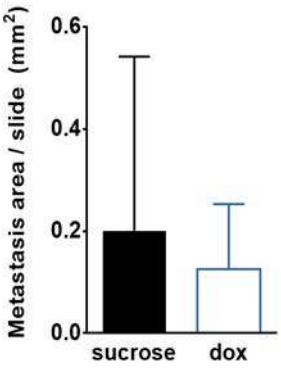

Figure 36. *MMTV-PyMT;TRE-Omomyc;CMV-rtTA* mice were treated with 5% sucrose (sucrose) or 2g/L doxycycline in 5% sucrose (dox) from 5 to 13 weeks of age and non-significant differences in primary tumor growth and lung metastasis appearance were detected.

A. Representation of the mouse model showing the age of appearance of primary tumors and lung metastases.
B. Primary tumor volumes of sucrose- and doxycycline-treated mice from treatment onset until endpoint.
C. Weekly weight change in sucrose- and doxycycline-treated mice. Results shown represent mean ± SEM.
D. Primary tumor volumes at endpoint. Statistical significance was determined via two-tailed Mann-Whitney test. Results shown represent mean ± SD.
E. Number of lung metastases/slide per mouse in sucrose- and doxycycline-treated groups after 8 weeks of treatment. Statistical significance was determined via two-tailed Mann-Whitney test. Results shown represent mean + SD.
F. Average area of individual lesions per mouse in sucrose- and doxycycline treated groups after 8 weeks of treatment. Statistical significance was determined via two-tailed Mann-Whitney test. Results shown represent mean + SD.
G. Total metastasis area/slide per mouse in sucrose- and doxycycline treated groups after 8 weeks of treatment. Statistical significance was determined via two-tailed Mann-Whitney test. Results shown represent mean + SD.

Hence, we conclude that either the low Omomyc levels or the change in subcellular localization observed in comparison with the original *TRE-Omomyc;CMV-rtTA* mice, or possibly a combination of both factors, account for the lack of response in doxycycline-treated *MMTV-PyMT;TRE-Omomyc;CMV-rtTA* mice. To solve this issue, we switched to the *MMTV-PyMT;TRE-Omomyc;βactin-rtTA* mouse model, in which mice express higher levels of nuclear Omomyc. Since we had observed that *MMTV-PyMT;TRE-Omomyc;βactin-rtTA* mice that did not receive doxycycline already expressed some Omomyc (Figure 34), they could not be used as controls. We used instead *MMTV-PyMT;TRE-Omomyc* littermates treated with doxycycline (n=19) and we compared them with *MMTV-PyMT;TRE-Omomyc;βactin-rtTA* treated with doxycycline (n=15) to

determine the effect of Omomyc on primary tumors and metastases. Some *MMTV-PyMT;TRE-Omomyc* (n=7) and *MMTV-PyMT;TRE-Omomyc;βactin-rtTA* (n=5) mice treated with sucrose were also added to the experiment. Treatment onset was established at 5 weeks of age and mice were euthanized at 13 weeks (Figure 37A).

While primary tumors in *MMTV-PyMT;TRE-Omomyc* mice treated with either sucrose or doxycycline developed normally, mice expressing Omomyc showed a dramatic impairment of tumor growth (Figure 37B, C, D and E). Expression of Omomyc in *MMTV-PyMT;TRE-Omomyc;βactin-rtTA* mice treated with doxycycline prevented tumor development almost completely. Consistently with the leakiness that we had observed by IF, the same mice treated with sucrose also showed a remarkable impairment in primary tumor formation, presenting tumors measurable by caliper only at 13 weeks of age (Figure 37B and C). Mammary fat pads were weighed at the experimental endpoint showing the same results: fat pads of *MMTV-PyMT;TRE-Omomyc* mice treated with sucrose or doxycycyline were bigger and twice as heavy as tumors from *MMTV-PyMT;TRE-Omomyc;βactin-rtTA* mice treated with sucrose or doxycycline (Figure 37D and E). Statistical differences were only observed between *MMTV-PyMT;TRE-Omomyc* and *MMTV-PyMT;TRE-Omomyc;βactin-rtTA* mice treated with doxycycline. No toxicity induced by Omomyc expression was observed, and differences in mice weight was likely accounted for by differences in tumor burden (Figure 37F).

A

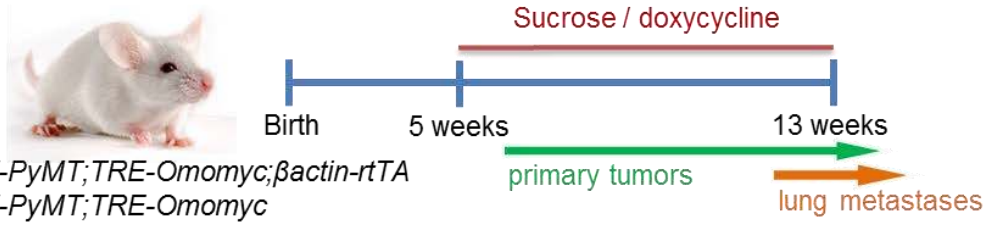

B

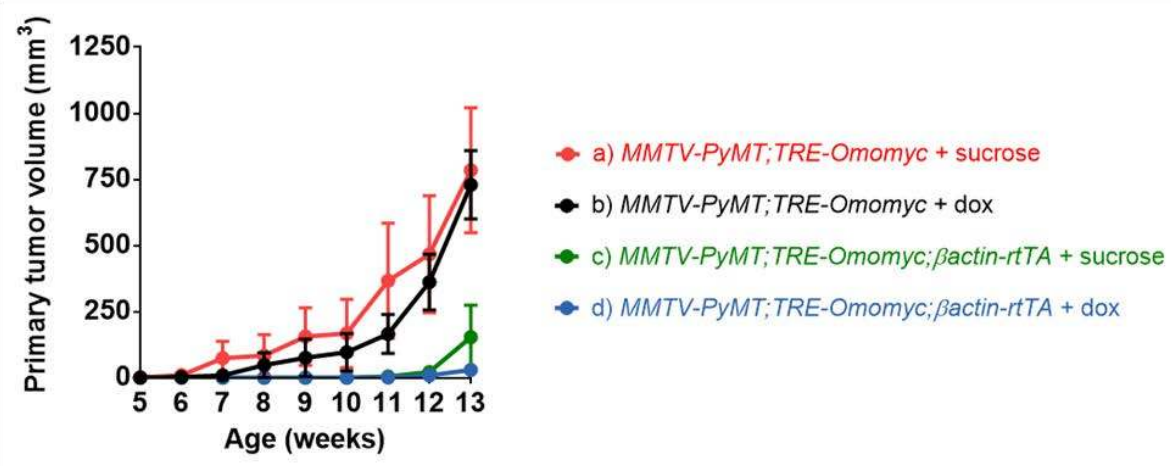

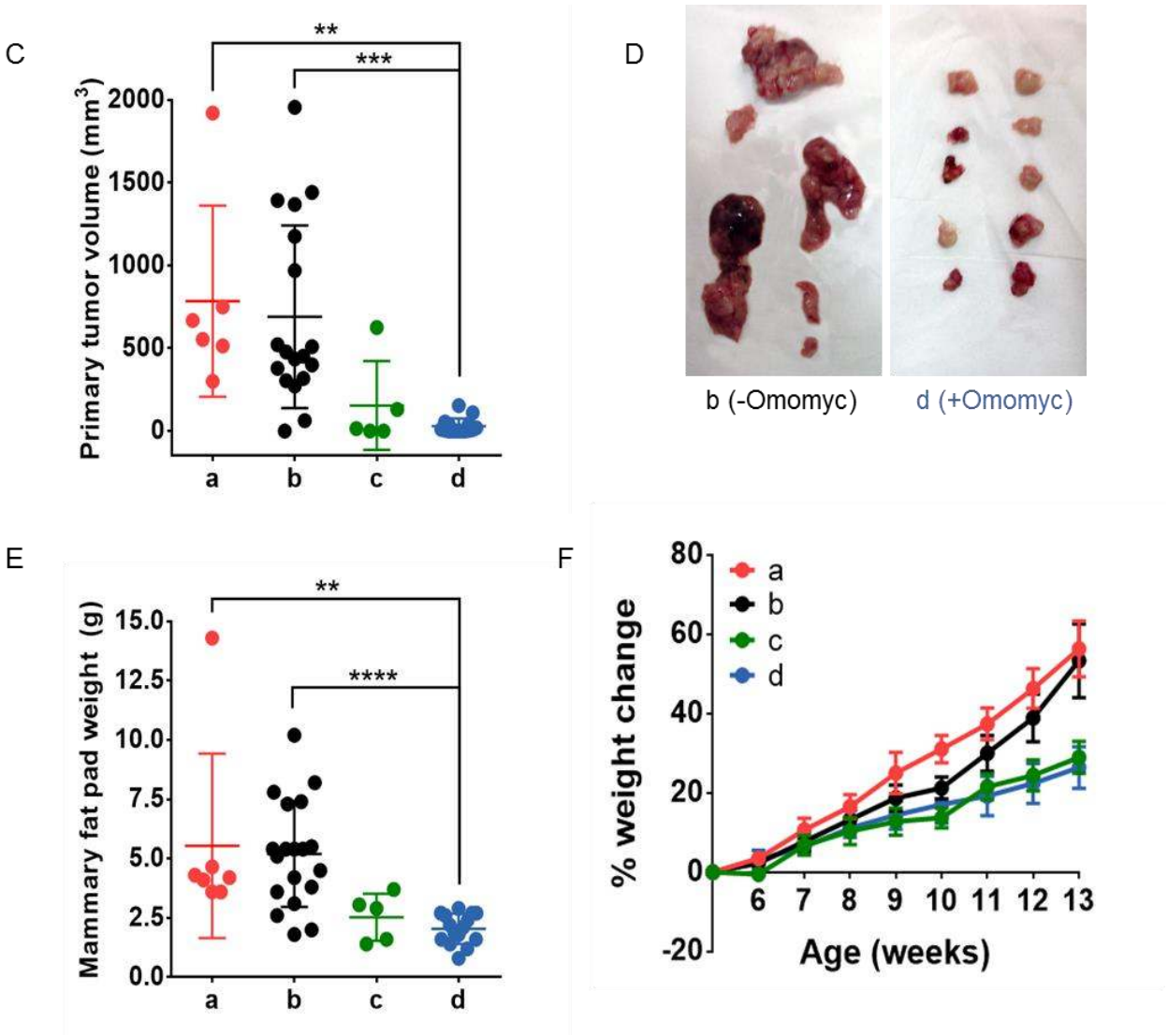

Figure 37. Primary tumor growth is dramatically impaired in *MMTV-PyMT;TRE-Omomyc;βactin-rtTA* mice. *MMTV-PyMT;TRE-Omomyc* and *MMTV-PyMT;TRE-Omomyc;βactin-rtTA* mice were treated with 5% sucrose (sucrose) or 2g/L doxycycline in 5% sucrose (dox) from 5 to 13 weeks of age.

A. Representation of the mouse model showing the age of appearance of primary tumors and lung metastases.

B. Primary tumor volumes of sucrose- and doxycycline-treated *MMTV-PyMT;TRE-Omomyc* and *MMTV-PyMT;TRE-Omomyc;βactin-rtTA* mice from treatment onset until endpoint.

C. Primary tumor volumes at endpoint. a=*MMTV-PyMT;TRE-Omomyc* + sucrose. b=*MMTV-PyMT;TRE-Omomyc* + dox. c=*MMTV-PyMT;TRE-Omomyc;βactin-rtTA* + sucrose. d=*MMTV-PyMT;TRE-Omomyc;βactin-rtTA* + dox. Kruskal-Wallis test was used for the analysis of variance, and the statistical difference between groups was determined via Dunn's multiple comparisons test (**, $P < 0.01$; ***, $P < 0.001$). Results shown represent mean ± SD.

D. Images of the mammary fat pads from a representative 13 week old, doxycycline-treated *MMTV-PyMT;TRE-Omomyc* mouse (b (-Omomyc)) and a *MMTV-PyMT;TRE-Omomyc;βactin-rtTA* mouse (d (+Omomyc)).

E. Mammary fat pad weight at endpoint a=*MMTV-PyMT;TRE-Omomyc* + sucrose. b=*MMTV-PyMT;TRE-Omomyc* + dox. c=*MMTV-PyMT;TRE-Omomyc;βactin-rtTA* + sucrose. d=*MMTV-PyMT;TRE-Omomyc;βactin-rtTA* + dox. Kruskal-Wallis test was used for the analysis of variance,

and the statistical difference between groups was determined via Dunn's multiple comparisons test (**, P < 0.01; ****, P < 0.0001). Results shown represent mean ± SD.

F. Weekly weight change in the four groups. a=*MMTV-PyMT;TRE-Omomyc* + sucrose. b=*MMTV-PyMT;TRE-Omomyc* + dox. c=*MMTV-PyMT;TRE-Omomyc;βactin-rtTA* + sucrose. d=*MMTV-PyMT;TRE-Omomyc;βactin-rtTA* + dox. Results shown represent mean ± SEM.

Metastatic burden was also measured in serial lung sections of doxycycline-treated *MMTV-PyMT;TRE-Omomyc* (no Omomyc expression) and *MMTV-PyMT;TRE-Omomyc;βactin-rtTA* mice (highest Omomyc expression) stained with H&E. In this preventive setting, metastasis appearance was heavily impaired by the expression of Omomyc (Figure 38A). In fact, the number of metastases per mouse was dramatically reduced (Figure 38B), with most Omomyc-expressing mice being metastasis free, and the few metastases present in these mice being significantly smaller (Figure 38C). The overall lung area occupied by metastases was consequently reduced very significantly in mice expressing Omomyc (Figure 38D). So, even though this system presents issues related to leakiness, it still shows a clear therapeutic impact of Omomyc on both primary tumors and metastasis.

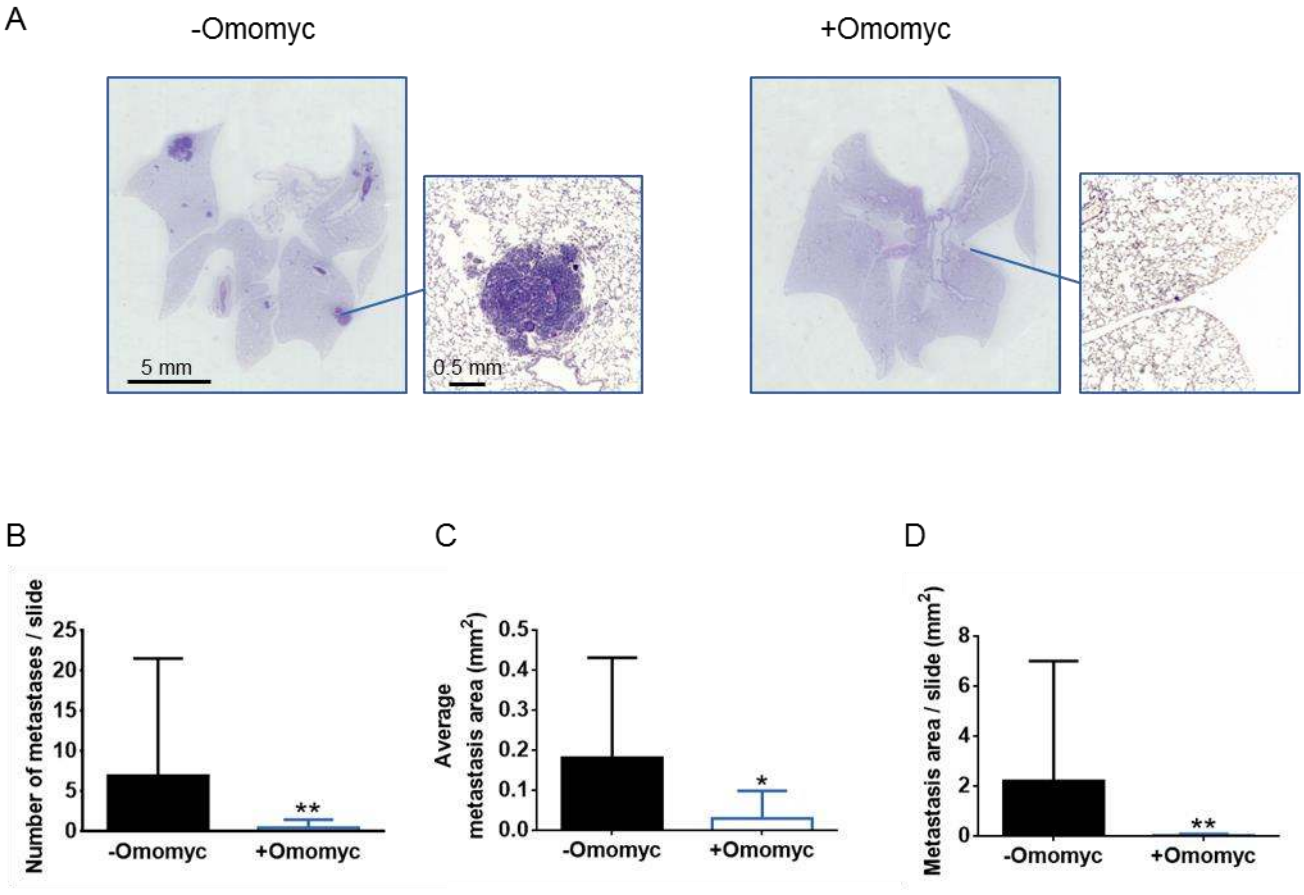

Figure 38. Lung metastasis appearance is dramatically impaired in *MMTV-PyMT;TRE-Omomyc;βactin-rtTA mice*. *MMTV-PyMT;TRE-Omomyc* and *MMTV-PyMT;TRE-Omomyc;βactin-rtTA* mice were treated with 2g/L doxycycline in 5% sucrose from 5 to 13 weeks of age.

A. H&E staining of a representative lung section from doxycycline-treated *MMTV-PyMT;TRE-Omomyc* (-Omomyc) and *PyMT;TRE-Omomyc;βactin-rtTA* (+Omomyc) mice, A higher magnification of one of each sections is shown.
B. Number of lung metastases/slide per mouse in doxycycline-treated *MMTV-PyMT;TRE-Omomyc* (-Omomyc) and *PyMT;TRE-Omomyc;βactin-rtTA* (+Omomyc) mice after 8 weeks. Statistical significance was determined via two-tailed Mann-Whitney test. Results shown represent mean + SD.
C. Average area of individual lesions per mouse in in doxycycline-treated *MMTV-PyMT;TRE-Omomyc* (-Omomyc) and *PyMT;TRE-Omomyc;βactin-rtTA* (+Omomyc) mice after 8 weeks. Statistical significance was determined via two-tailed Mann-Whitney test. Results shown represent mean + SD.
D. Total metastasis area per mouse in doxycycline-treated *MMTV-PyMT;TRE-Omomyc* (-Omomyc) and *PyMT;TRE-Omomyc;βactin-rtTA* (+Omomyc) mice after 8 weeks. Statistical significance was determined via two-tailed Mann-Whitney test. Results shown represent mean + SD.

2.10 The Omomyc polypeptide: a potential pharmacological approach to inhibit Myc in breast cancer

This thesis extensively describes the potential therapeutic impact of Omomyc expression against metastatic breast cancer. However, until very recently, Omomyc has only been considered a genetic proof of principle of the feasibility and potential of Myc inhibition, but with no further hope to be translated into a clinically viable drug (von Eyss and Eilers 2011; Montagne et al. 2012). Nevertheless, very recently we showed that the Omomyc polypeptide (11 kDa) displays cell-penetrating properties and can spontaneously penetrate into non-small cell lung cancer (NSCLC) cells and localize in their nuclei, where it interferes with Myc-driven transcription and impairs cell proliferation *in vitro* and *in vivo* (Beaulieu et al, under review). With these properties in mind, we hypothesized that the Omomyc cell-penetrating peptide (Omomyc^{CPP}) could also be employed as a drug against metastatic breast cancer.

First, to validate our hypothesis, we treated MDA-MB-231 cells with 20 μM of Omomyc^{CPP} labeled with FITC and, after only 15 minutes, we verified that the peptide localized in their nuclei (Figure 39A), demonstrating the cell-penetrating capacity of Omomyc in breast cancer. To determine whether cell entry was dose dependent, Omomyc^{CPP} was labeled with AlexaFluor 488 (A488) and MDA-MB-231 cells were treated with increasing concentrations of the labeled peptide for 15 minutes,

demonstrating that it is internalized inside the cells in a dose-dependent manner (Figure 39B).

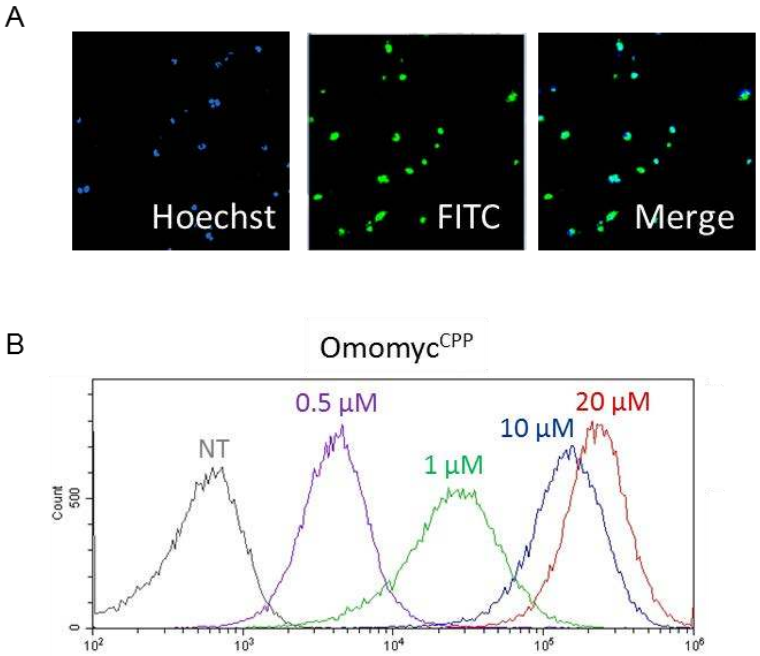

Figure 39. The Omomyc peptide can spontaneously penetrate into MDA-MB-2321 cells in a dose-dependent manner.

A. Fluorescent Image of Omomyc^{CPP}-FITC localized inside MDA-MB-231 nuclei stained with Hoechst 15 minutes after addition to the culture media.
B. Flow cytometry analysis non-treated MDA-MB-231 cells (NT) or treated with Omomyc^{CPP}–A488 at 0.5 µM, 1 µM, 10 µM and 20 µM for 15 minutes.

Then, in an attempt to further improve Omomyc^{CPP} activity and targeting of metastasis *in vivo*, the original Omomyc peptide was fused with TMTP1, a 5-amino acid cell-penetrating peptide (NVVRQ) with the capacity to bind specifically to highly metastatic cells, where it induces apoptosis, but with no binding capacity to poorly- or non-metastatic cells (Yang et al. 2008; Li et al. 2015; Li et al. 2016).

To characterize the effects on cell proliferation exerted by these peptides and compare with that induced by lentiviral expression of Omomyc, MDA-MB-231 cells were incubated with 20 µM Omomyc^{CPP}, TMTP1-Omomyc or an equivalent volume of vehicle (PBS) for 3 days and the cell cycle analyzed by BrdU incorporation and PI staining. The cell cycle profile was similar to the one previously shown by lentivirally-expressed Omomyc (Figure 23E, F and G), with a reduction of DNA incorporation during the S phase in cells treated with either peptide (Figure 40A and B), and an increase in the percentage of cells in G0/G1 (Figure 40A and C).

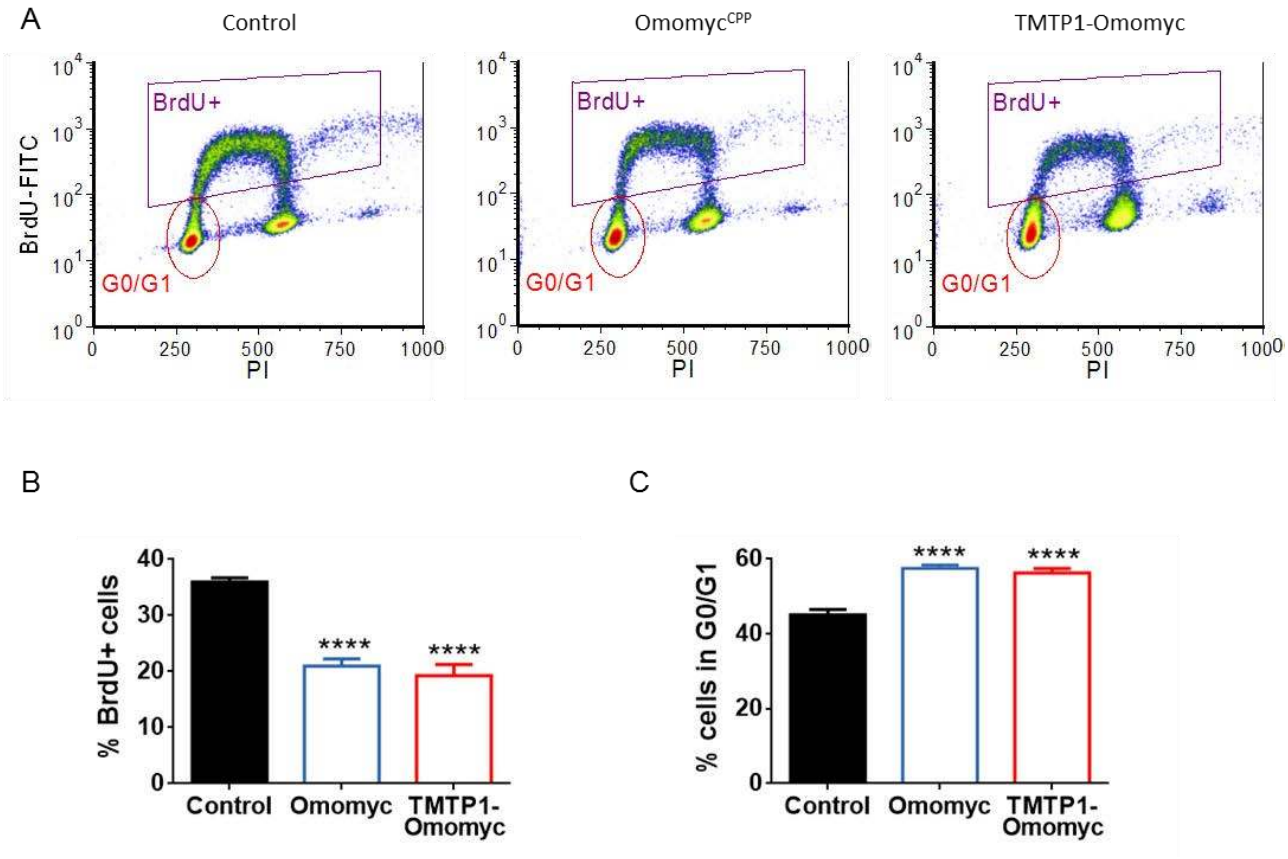

Figure 40. Omomyc^{CPP} and TMTP1-Omomyc reduce DNA synthesis during the S phase of the cell cycle and induce an arrest in G0/G1 in MDA-MB-231 cells.

A. Representative density plots of MDA-MB-231 cells treated with PBS (control), 20 μM Omomyc^{CPP} and 20 μM TMTP1-Omomyc for 3 days measured by flow cytomerty. BrdU-FITC: Bromodeoxyuridine-Fluorescein isothiocyanate. PI: Propidium idodide.
B. % of BrdU-positive MDA-MB-231 cells treated with PBS (control), 20 μM Omomyc^{CPP} and 20 μM TMTP1-Omomyc. One-way ANOVA was used for the analysis of variance, and the statistical difference between groups was determined via Dunnett's multiple comparisons test (****, P<0.0001). Results shown represent mean + SD.
C. % of MDA-MB-231 cells treated with PBS (control), 20 μM Omomyc^{CPP} and 20 μM TMTP1-Omomyc in G0/G1 measured by flow cytometry. One-way ANOVA was used for the analysis of variance, and the statistical difference between groups was determined via Dunnett's multiple comparisons test (****, P<0.0001). Results shown represent mean + SD.

Having demonstrated that both peptides acted similarly to lentivirally-expressed Omomyc, we wondered whether TMTP1-Omomyc was internalized into metastatic breast cancer cells more efficiently than Omomyc^{CPP}. To this end, we labelled both peptides with A488 and MDA-MB-231 cells were treated with 0.5 μM Omomyc^{CPP}-A488 and TMTP1-Omomyc-A488 for 15 minutes. In this case, TMTP1-Omomyc appeared to enter cells more efficiently than the original Omomyc^{CPP} (Figure 41A).

To determine whether this difference translated into an enhanced therapeutic effect, Omomyc^{CPP} and TMTP1-Omomyc were added to the medium of MDA-MB-231 cells at 2 different concentrations (5 μM and 20 μM) 3 times a week for 2 weeks. Surprisingly, even if both peptides interfere similarly with BrdU incorporation rates in MDA-MB-231 cells (Figure 40), here we observed that TMTP1 is much more effective, totally preventing cell expansion when administered at 20 μM (Figure 41B). Therefore we evaluated the extent of cell death induced by the peptides by treating MDA-MB-231 cells with a single dose of 20 μM of Omomyc^{CPP} or TMTP1-Omomyc and counting trypan blue-positive cells after 6 days. We found that, indeed, while Omomyc^{CPP} induced negligible death, TMTP1-Omomyc caused abundant cell death (Figure 41C). To calculate the IC50 of both peptides, a single dose of increasing concentrations of Omomyc^{CPP} or TMTP1-Omomyc was added to the medium of MDA-MB-231 cells and cell number analyzed after 6 days. The IC50s obtained were 16.98 μM for Omomyc^{CPP} and 8.99 μM for TMTP1-Omomyc (Figure 41D), indicating once again the superiority of TMTP1-Omomyc compared to Omomyc^{CPP}, hence we decided to proceed with TMTP1-Omomyc for the following *in vivo* studies.

A

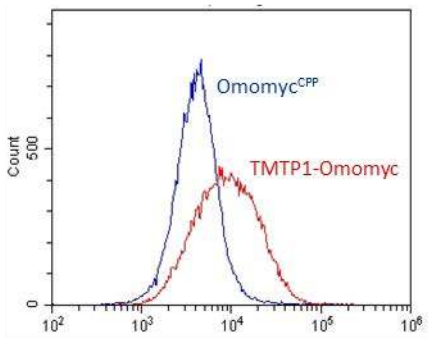

B

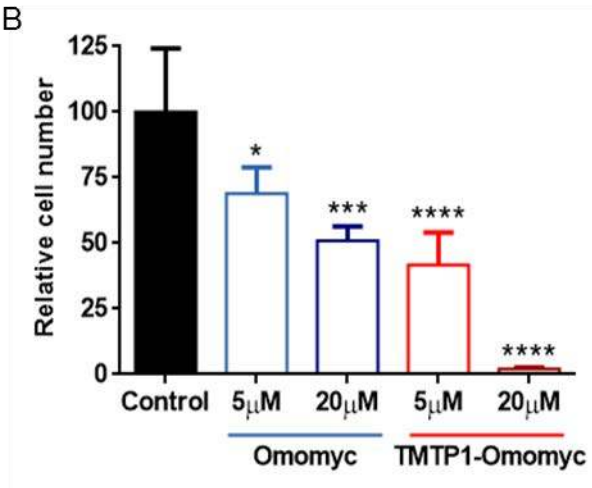

C

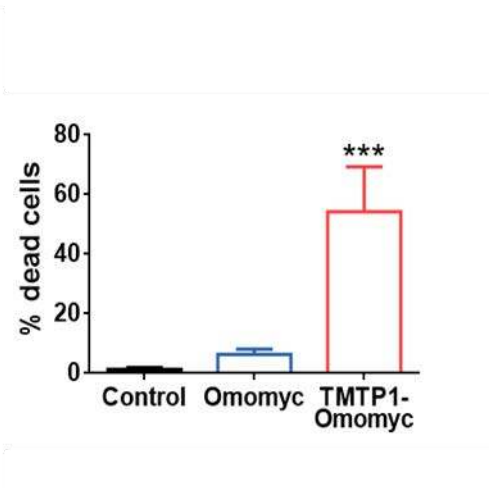

D

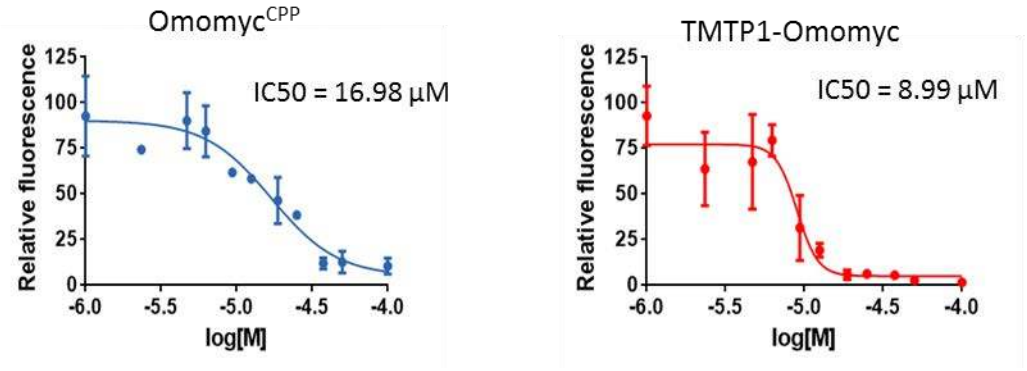

Figure 41. TMTP1-Omomyc penetrates into MDA-MB-231 cells more efficiently than Omomyc^{CPP}, reduces proliferation more efficiently and induces cell death.

A. Flow cytometry analysis of MDA-MB-231 cells treated with 0.5 µM Omomyc^{CPP}–A488 or 0.5 µM TMTP1-Omomyc-A488.

B. Counts of MDA-MB-231 cells treated with 5 µM and 20 µM Omomyc^{CPP} or TMTP1-Omomyc for 2 weeks. One-way ANOVA was used for the analysis of variance, and the statistical difference between groups was determined via Dunnett's multiple comparisons test. Results shown represent mean + SD.

C. % of trypan-blue positive MDA-MB-231 cells treated with 20 µM Omomyc^{CPP} or 20 µM TMTP1-Omomyc for 1 week. One-way ANOVA was used for the analysis of variance, and the statistical difference between groups was determined via Dunnett's multiple comparisons test. Results shown represent mean + SD.

D. IC50s of Omomyc^{CPP} and TMTP1-Omomyc obtained from treating MDA-MB-231 cells with one single dose of each peptide at increasing concentrations ranging from 2.34 µM to 100 µM for 6 days. Results shown represent mean ± SD.

2.11 Treatment with the TMTP1-Omomyc peptide reduces primary tumor growth in a cell line-derived orthotopic model

To test the therapeutic impact of TMTP1-Omomyc *in vivo*, the MDA-MB-231-derived LM2-4175 TGL cells were inoculated orthotopically in the mammary fat pad of 22 BALB/c nude mice and, when tumors reached 100 mm^3, mice were randomized into 2 groups and treated with intratumoral injections of TMTP1-Omomyc (n = 11) or vehicle (50 mM NaAc 150 mM NaCl pH 6.15) (n = 11) 3 times a week for 4 weeks (Figure 42A). Tumors receiving TMTP1-Omomyc showed a slower growth rate that translated into a significant difference in tumor volume starting 7 days after treatment onset (Figure 42B), a difference that was maintained until the experimental endpoint (Figure 42B and C). Tumor weight also reflected the difference in tumor size at the endpoint, with significant differences between groups (Figure 42D). Importantly, injections of TMTP1-Omomyc did not show any visible sign of toxicity in the mice, which did not lose

weight throughout the experiment. Small differences in weight starting from 9 days after treatment onset are probably due to differences in tumor size (Figure 42E).

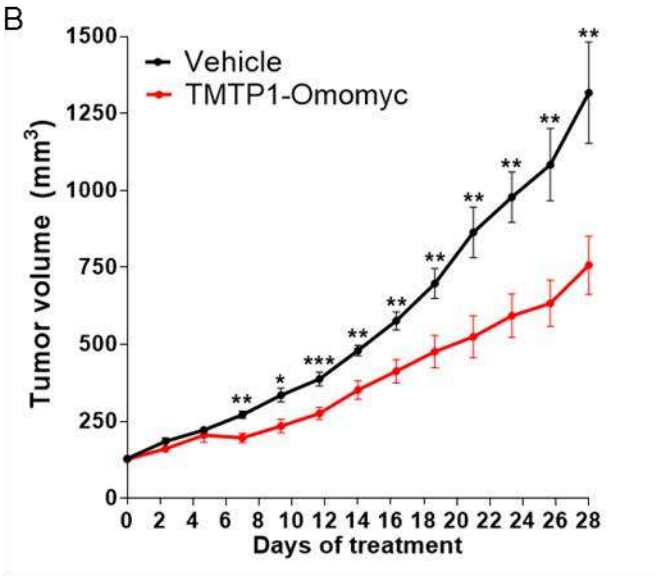

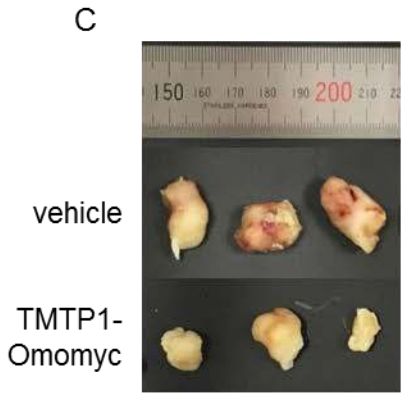

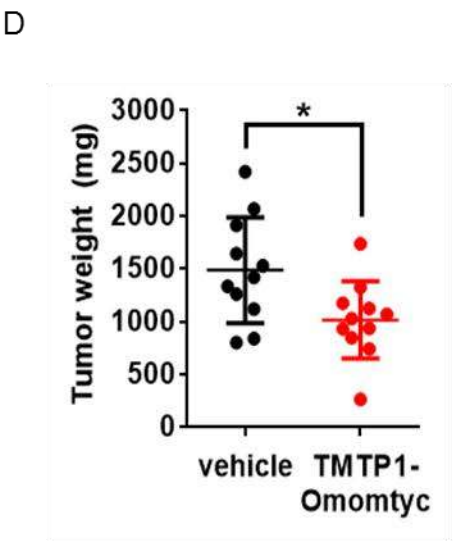

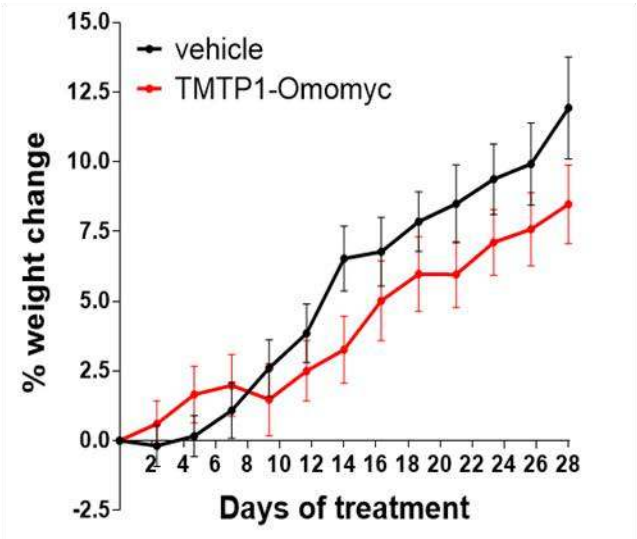

Figure 42. Intratumoral injections of TMTP1-Omomyc reduce primary tumor growth in a cell-line derived orthotopic model. LM2-4175 TGL pSLIK Omomyc c#11 cells were inoculated into BALB/c nude female mice. When tumors reached 100 mm^3, mice were treated with intratumoral injections of vehicle (50 mM NaAc 150 mM NaCl pH 6.15) and with TMTP1-Omomyc for 4 weeks.

A. Schematic representation of the mouse model.
B. Tumor volume of vehicle- and TMTP1-Omomyc-treated tumors for 4 weeks shows a significant difference among them. Statistical significance was determined via two-tailed Mann-Whitney test (*, $P < 0.05$; **, $P < 0.01$; ***, $P < 0.001$). Results shown represent mean ± SEM.
C. Image of 3 representative tumors from vehicle- and TMTP1-Omomyc-treated mice.
D. *Ex vivo* tumor weight shows a significant difference among groups. Statistical significance was determined via two-tailed unpaired T test (*, $P < 0.05$). Results shown represent mean ± SD.
E. Weight change in sucrose- and doxycycline-treated mice. Results shown represent mean ± SEM.

2.12 Treatment with the TMTP1-Omomyc peptide reduces tumor growth in a lung colonization model

In order to validate the Omomyc-based drug as a method to efficiently target breast cancer metastasis, we decided to combine the treatment of primary tumors with the treatment of the metastatic sites. The encouraging efficacy data obtained from intratumoral injections of TMTP1-Omomyc in primary breast tumors, combined with the observation that intranasal administration of $Omomyc^{CPP}$ reduced tumor burden in a transgenic mouse model of NSCLC (Beaulieu et al, under review), suggested that intranasal administration of TMTP1-Omomyc could be effective against lung metastases. To test this hypothesis, we used the mouse model of lung colonization described previously (Results 2.6). In addition, since the standard of care therapy for TNBC patients is still chemotherapy, we decided to test the efficacy of TMTP1-Omomyc alone or in combination with the chemotherapeutic agent paclitaxel.

More in detail, LM2-4175 TGL cells were injected into the bloodstream through the lateral tail vein of 41 BALB/C nude mice, tumor growth was followed weekly by IVIS imaging and lung tumors were allowed to establish and grow for 3 weeks. At this point, mice were randomized into 4 groups and treated with vehicle (n = 10), paclitaxel intraperitoneally (i.p.) (n = 10), TMTP1-Omomyc intranasally (i.n.) (n = 11), and the combination of TMTP1-Omomyc and paclitaxel (n = 10) for 4 weeks (Figure 43A). None of the treatments was toxic for the mice at the doses administered, and all the animals gained weight (Figure 43B). As expected, IVIS imaging revealed that paclitaxel seemed effective in reducing tumor growth. TMTP1-Omomyc had a similar effect, and the combination appeared slightly more effective (Figure 43C and D). However, due to the high degree of variability in bioluminescence intensity in the control group (mean ±

SD = $1.5 \cdot 10^8$ ± $3.1 \cdot 10^8$), no statistical differences were found among groups. µCT images were acquired at the experimental endpoint, but high tumor burden in some of the mice made it impossible to discriminate between individual tumors. In an attempt to rescue the µCT data and provide some quantification, personnel at VHIR's imaging platform designed an indirect method for tumor burden quantification: briefly, the volume occupied by healthy lung tissue of each mouse was measured, as well as the volume of the thoracic cavity. A ratio lung/thorax was calculated, and the highest values correlated with the mice that presented less tumor burden by eye. Ratios of mice treated with paclitaxel, TMTP1-Omomyc or the combination were higher than those from the control group, agreeing with the data from bioluminescent imaging that suggested a reduced tumor burden in treated animals (Figure 43D). Encouragingly, with this method, statistically significant differences were observed between control mice and those treated with TMTP1-Omomyc as a monotherapy, although a trend was visible for all the treated groups (Figure 43E).

A

B

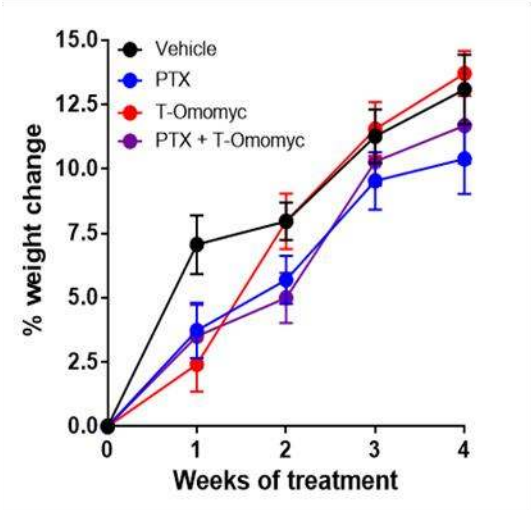

C

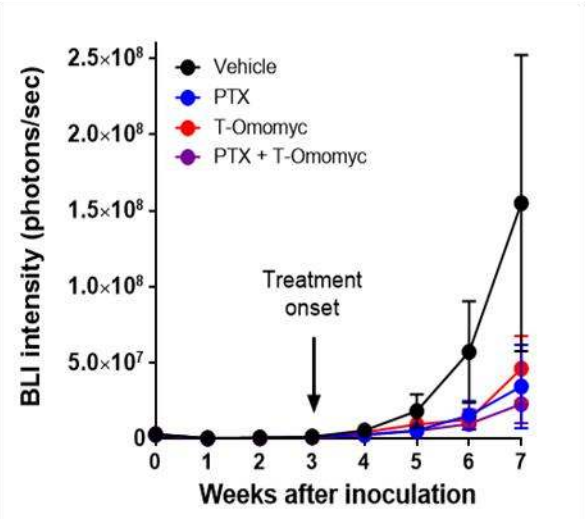

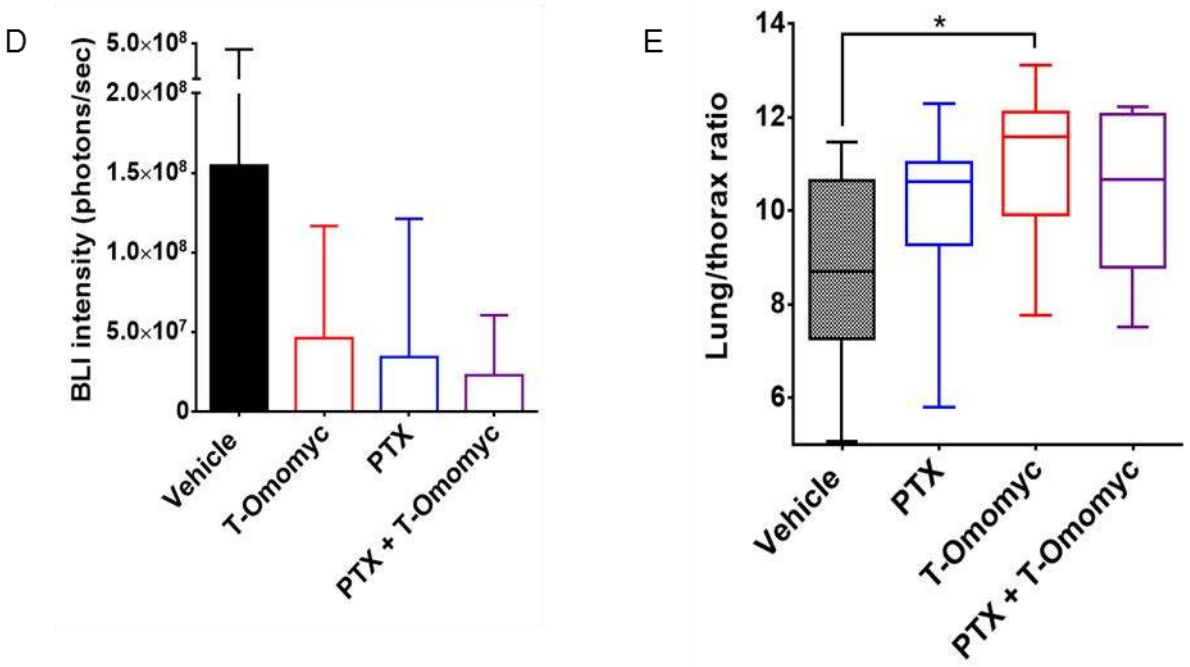

Figure 43. TMTP1-Omomyc, paclitaxel, and their combination reduce lung tumor growth in a cell-line derived model of lung colonization.

LM2-4175 TGL pSLIK Omomyc c#11 cells were inoculated through the lateral tail vein into BALB/c nude females. 3 weeks later, they were treated with TMTP1-Omomyc (T-Omomyc) i.n., with paclitaxel (PTX) i.p., with TMTP1-Omomyc and paclitaxel (PTX + T-Omomyc), or with vehicle (50 mM NaAc 150 mM NaCl pH 6.15 i.n, PBS i.p).

A. Schematic representation of the mouse model.
B. Weekly weight change in all groups. Results shown represent mean ± SEM.
C. Luciferase activity measured weekly by IVIS imaging as bioluminescence (BLI) intensity, showing a delay in tumor growth of all treated groups compared to vehicle-treated mice.
D. Luciferase activity at experimental endpoint measured by IVIS imaging as bioluminescence (BLI) intensity shows a non-significant reduction in all treated groups. Kruskal-Wallis test was used for the analysis of variance, and the statistical difference between groups was determined via Dunn's multiple comparisons test. Results shown represent mean + SD.
E. Lung/thorax ratio at experimental endpoint calculated from μCT images shows a significant increase in TMTP1-Omomyc treated mice and a non-significant increase in PTX and PTX + TMTP1-Omomyc mice compared with the vehicle-treated controls. Kruskal-Wallis test was used for the analysis of variance, and the statistical difference between groups was determined via Dunn's multiple comparisons test. Results shown represent mean ± SD.

DISCUSSION

1 PART 1

In the first part of this thesis, we sought to validate the therapeutic utility of inhibiting mast cell function in PDAC by employing the BTK inhibitor ibrutinib. The role of mast cells in cancer is still controversial, and seems to be either tumor-promoting or tumor-suppressive depending on the context (Galinsky and Nechushtan 2008; Ribatti and Crivellato 2009). While high mast cell numbers are a good prognostic factor in ovarian cancer (Chan et al. 2005), NSCLC (Welsh et al. 2005), squamous cell carcinoma (Attramadal et al. 2016) and breast cancer (Rajput et al. 2008), its presence is correlated with poor outcome in prostate cancer (Johansson et al. 2010), lymphoma (Rabenhorst et al. 2012) and melanoma (Grimbaldeston et al. 2004). In PDAC, even though one report defines mast cells as dispensable for tumor formation in a mouse model (Schonhuber et al. 2014), they have been associated with poor prognosis in patients (Strouch et al. 2010; Cai et al. 2011) and other studies confirm their vital importance in tumor development and maintenance (Chang et al. 2011; Ma et al. 2013). For these reasons, we hypothesized that treatment with ibrutinib would be effective against PDAC models *in vivo*.

In line with what was previously reported in our mouse model of Myc-driven insulinoma (Soucek et al. 2011), we showed that treatment with ibrutinib efficiently blocked mast cell degranulation also in transgenic *p53$^{ER/ER}$;LSLKras^{G12D};Pdx1-Cre* mice and PDXs obtained by inoculation of human tumors into NOD/SCID mice (Masso-Valles et al. 2015). Mast cell stabilization was accompanied by a decrease in cell proliferation, leukocytic infiltration in the tumor microenvironment (CD11b positive cells and F4/80 positive macrophages) and increased survival. The decrease in the leukocytic component after treatment with ibrutinib could be explained by the fact that several chemokines produced by mast cells, such as IL-6, are known to be potent stimulants for monocytic cell migration and macrophage activation (Clahsen and Schaper 2008), so that inhibiting mast cells could prevent their recruitment.

Unexpectedly, ibrutinib also caused a potent antifibrotic effect in tumors from both the transgenic and PDX models (Masso-Valles et al. 2015), a discovery that led to a patent filing ('Methods for Treating Fibrosis', WIPO Patent Application WO/2016/090021. Inventors: Laura Soucek, Daniel Massó-Vallés and Toni Jauset). This was consistent with data showing that ibrutinib specifically inhibits the release of IL-8, MCP-1 and TNFα from mast cells (Chang et al. 2011). All these factors have a known role in

fibrosis: IL-8 is elevated in the serum of idiopathic pulmonary fibrosis patients (Ziegenhagen et al. 1998) and correlates with the degree of fibrosis in infants with chronic liver disease (Nobili et al. 2004); MCP-1 is a key determinant in the development of skin fibrosis, it could influence collagen fiber formation in mice (Ferreira et al. 2006) and is involved in the development of interstitial fibrosis in a mouse model of crescentic nephritis (Lloyd et al. 1997); finally, TNFα, which has a controversial role in fibrotic disease (Distler et al. 2008), promotes survival of activated hepatic stellate cells *in vitro* and *in vivo*, increases liver fibrosis in mice (Pradere et al. 2013), mediates the transition from pulmonary inflammation to fibrosis (Oikonomou et al. 2006) and its inhibition reduces fibrosis in a mouse model of autoimmune thyroiditis (Chen et al. 2007). NOD/SCID mice have a reduced number and function of granulocytes, which could explain why, even though we detected degranulating mast cells in their tumor microenvironment which were efficiently stabilized by ibrutinib, treatment caused a significant but less potent antifibrotic effect when compared to the one exerted in *p53$^{ER/ER}$;LSLKras^{G12D};Pdx1-Cre* mice.

Notably, ibrutinib has been found to inhibit other tyrosine kinases besides BTK, namely EGFR, HER2, HER3, HER4, Tec, ITK, JAK3, Blk, Fgr, Hck, Lck, Yes/YES1, Bmx/Etk and Txk. Owing to this feature, ibrutinib showed promising *in vitro* efficacy against EGFR-mutated non-small cell lung cancer (NSCLC) (Gao et al. 2014) and HER2 positive breast cancer (Chen et al. 2016). However, epidermal growth factor receptor (EGFR) mutation and human epidermal growth factor receptor 2 (HER2) overexpression are not frequent events in PDAC and none of our experimental systems presented EGFR or HER2 alterations. To make sure that the effects of ibrutinib were non-cell autonomous and due to mast cell interference (as opposed to being caused by direct targeting of cancer cells), we treated PDAC cell lines *in vitro* with increasing concentrations of ibrutinib. As a positive control, we treated two EGFR-driven NSCLC cell lines previously reported to respond to the drug (Gao et al. 2014). As expected, cell number was reduced in a dose-dependent manner upon treatment with ibrutinib only in these NSCLC cell lines, while PDAC cells were unaffected. Thus, we discarded any direct effect of this kinase inhibitor on cancer cell growth or survival, suggesting that the phenotypic changes observed in the tumor were solely dependent on BTK inhibition in the stroma.

It should be noted that ibrutinib is a well-known inhibitor of B cell-signaling and macrophage function, so there is a possibility that some of the phenotypes that we observed are not only mast cell dependent. Recently, it was reported that BTK

expression in B cells and macrophages drives pancreatic cancer by T cell suppression, and treatment of PDAC models with ibrutinib restores T-cell dependent anti-tumor responses (Gunderson et al. 2016). Importantly, though, NOD/SCID mice, which were used in some of our studies, are characterized by a severe immunodeficiency affecting B- and T-lymphocyte development and NK cell function. Thus, decreased fibrosis in our PDX model confirmed that, at least this effect of ibrutinib, is B- and T-cell independent. However, in order to definitively confirm whether the antifibrotic effect was really mast cell dependent, tumor-bearing *p53$^{ER/ER}$;LSLKras^{G12D};Pdx1-Cre* mice were treated with cromolyn, a mast cell stabilizer that phenocopied the decrease in collagen deposition induced by ibrutinib, as well as a slight decrease in F4/80+ macrophages and a significant decrease in CD11+ leukocytes. Hence, although cromolyn was also described to display some cytotoxic effect on pancreatic cancer cells (Arumugam et al. 2006), the overlapping effect of ibrutinib and cromolyn on collagen deposition strongly suggests that mast cell inhibition is the most likely explanation for this phenomenon.

Our findings are consistent with recently published work showing that mast cells could exacerbate the cellular and extracellular dynamics of the tumor microenvironment found in PDAC (Ma et al. 2013). Tumor cells have been found to promote mast cell migration, and both tumor cells and pancreatic stellate cells (PSC), also known as cancer-associated fibroblasts, stimulate mast cell activation. Conversely, mast cells stimulate PSC proliferation by secreting IL-13 and tryptase. PSCs are the principal source of tumor fibrosis and interact with cancer cells to promote tumorigenesis and metastasis (Phillips 2012). Hence, it is likely that ibrutinib regulates PSCs through inhibition of mast cells, so assessing the activation state of PSCs before and after treatment (i.e. by alpha smooth muscle actin (αSMA) immunohistochemistry) would shed light on its mechanism of action.

Importantly, all our experimental models combined point to mast cells as crucial players in stromal sustainment, in line with previously published data in non-cancer models which showed that cell tryptase might sustain liver fibrosis by promoting stellate cell proliferation and collagen synthesis (Gaca et al. 2002) and with the concept that mast cells could be the culprit in various fibrotic diseases (Overed-Sayer et al. 2013; Hugle 2014). Therefore, in addition to its beneficial role in reducing tumor fibrosis, the use of ibrutinib could potentially be extended to the treatment of various fibrotic diseases, such as liver fibrosis (Bataller and Brenner 2005) or chronic pancreatitis (Homma et al. 1997).

In the context of fibrosis, many studies have highlighted that the characteristically dense desmoplastic reaction found in PDAC impairs drug delivery and promotes chemoresistance (Whatcott et al. 2012; Schober et al. 2014). Therefore, we hypothesized that treatment with ibrutinib could enhance chemotherapeutic delivery by reducing desmoplasia, improving cytotoxic activity against cancer cells. Indeed, we found that treatment of PDAC-bearing *p53$^{ER/ER}$;LSLKras^{G12D};Pdx1-Cre* mice with a combination of ibrutinib and gemcitabine increased survival significantly when compared to gemcitabine alone, supporting this hypothesis. Nevertheless, pharmacokinetic studies will need to be performed in order to characterize the biodistribution of chemotherapeutic agents in combination with ibrutinib and confirm this hypothetical improved delivery. Unfortunately, in our hands, gemcitabine turned out to be extremely toxic in NOD/SCID mice, which prevented us from confirming these results in our PDX model.

In order to prove that the presence of a desmoplastic stroma is a requirement for the synergy between ibrutinib and gemcitabine, we utilized a mouse model of PDAC which completely lacks fibrosis in the tumor microenvironment: we inoculated MIA PaCa-2 cells orthotopically into BALB/c nude mice, which tolerate gemcitabine and have no impairment in mast cell numbers nor function (Wlodarski et al. 1982). As expected, tumors that arose in these mice were not able to recapitulate the characteristic PDAC stroma of our other two *in vivo* systems, resulting in a complete absence of collagen fibers. Consistent with this observation, treatment with gemcitabine was very effective in reducing tumor growth, but neither synergy nor an additive effect with ibrutinib was observed, confirming the role of ibrutinib in reducing desmoplasia as its main mechanism to promote survival. Even though no impairment in mast cell numbers has been reported in BALB/c nude mice, we observed significantly less infiltration in the pancreas of PDAC-bearing BALB/c nude mice when compared to *p53$^{ER/ER}$;LSLKras^{G12D};Pdx1-Cre* mice. Also, we observed no significant increase in mast cell infiltration between normal pancreas and PDAC in BALB/c nude mice, but a significant increase between normal pancreas and PDAC in C57BL/6-FVB/N transgenic mice, which correlated with the presence of fibrotic tumors. A likely explanation could be that human MIA PaCa-2 cells are not able to attract mouse mast cells (and possibly other components of the tumor microenvironment) to the tumor stroma, impeding the desmoplastic reaction that occurs in immune competent animals. Therefore, the lack of synergy between gemcitabine and ibrutinib in the orthotropic model could be due to the absence of fibrosis, but also to the low number of degranulating mast cells, which are ibrutinib's main target in our model.

Metastasis is the main cause of death in patients suffering from PDAC. Unfortunately, none of our fibrotic *in vivo* models is highly metastatic, so we could not investigate the effect of ibrutinib in the metastatic spread or the treatment of established metastases. Therefore, further studies in metastatic, fibrotic models treated with ibrutinib and chemotherapy would be extremely informative for the prediction of how patients with advanced PDAC would respond to the combination treatment. Encouragingly, it has been recently reported that metastatic lesions of PDAC recapitulate the fibrosis of primary tumors and that the extent of fibrosis is associated with poor survival (Whatcott et al. 2015), which suggests that ibrutinib could be as effective in metastatic lesions as it is against primary tumors.

Notably, BTK expression is not restricted to B-lymphocytes, macrophages and mast cells. In fact, it is expressed in all hematopoietic lineages with the exception of T-lymphocytes. For example, myeloid-derived suppressor cells (MDSCs) express BTK and are present in the stroma of many different tumors, causing immunosuppression and evasion of anti-tumor immune responses. Consistently, treatment of breast cancer and melanoma mouse models with ibrutinib reduced the number of MDSCs in the spleen and the tumor, and combination therapy with the immune checkpoint inhibitor anti-Programmed Death-Ligand 1 (PD-L1) resulted in reduced mammary tumor growth (Stiff et al. 2016). For this reason, it remains possible that additional anti-inflammatory effects of ibrutinib might contribute to its therapeutic impact by modulation of other inflammatory components, even though we have demonstrated that such signaling is not required for decreased fibrosis. Further study of the effect of ibrutinib on other members of the complex PDAC stroma, especially MDSCs, will be required to fully characterize its precise mechanism of action, and the contribution of BTK-related responses versus inhibition of other kinases, either in tumor cells themselves or in the tumor stroma.

To summarize, this work provides pre-clinical evidence for the use of ibrutinib – which is already approved for clinical use – in the treatment of PDAC, based on the observed systemic mast cell inhibitory effects of ibrutinib as a potentially new and potent anti-fibrotic drug. In fact, our results have contributed to the initiation of two clinical trials with the objective of validating the addition of ibrutinb to the standard of care as a new therapeutic option for patients with metastatic PDAC. An open label phase 1/2 clinical trial for the assessment of the safety, Immunopharmacodynamics and anti-tumor activity of ibrutinib in combination with gemcitabine and nab-paclitaxel is already

underway (NCT02562898), and a randomized, multicenter, double-blind, phase 2/3 clinical trial is currently evaluating this triple combination as first line treatment for patients with advanced PDAC (RESOLVE study, NCT02436668).

2 PART 2

In the second part of this thesis we sought to establish the therapeutic utility of inhibiting Myc in metastatic breast cancer models *in vitro* and *in vivo* by making use of our well characterized Myc dominant negative Omomyc. By interfering with Myc transactivation, Omomyc has shown extraordinary efficacy against primary tumors in multiple mouse models of cancer, regardless of the tumor type or driving oncogenic lesions (Soucek et al. 2004; Soucek et al. 2008; Sodir et al. 2011; Soucek et al. 2013; Annibali et al. 2014). Hence, we demonstrated that many, perhaps all, primary tumors are addicted to Myc, even after becoming established. Given that metastatic disease, though, is the primary cause of cancer-related deaths, we asked whether Myc dependency is still conserved in metastases. We hypothesized that targeting Myc, a non-redundant node in cancer, would be effective against metastatic disease for various reasons. On the one hand, metastases are genetically unstable, meaning that information from a patient's primary tumor may not accurately reflect the metastasis, and one metastasis may vary from another, hindering the benefits of targeted therapies (Marino et al. 2013), and our data suggest that Myc inhibition would be effective independently of the mutational profile of the tumor. On the other hand, Myc promotes EMT and dedifferentiation, two key aspects of metastasis (Wolfer and Ramaswamy 2011), suggesting that inhibiting it could revert these features. Nevertheless, we can find contradictory reports on the impact of Myc inhibition in the context of metastasis, since it has been reported to both inhibit and enhance it. For instance, repression of integrin expression by MYC in breast cancer cells has been linked to suppression of cell migration and metastasis (Liu et al. 2012), but another report suggests that Skp2 cooperates with Myc to induce RhoA transcription by recruiting Miz1 and p300 to the RhoA promoter, thereby promoting metastasis (Chan et al. 2010). These are only two examples out of several publications in which Myc has been associated with metastasis in breast and other cancers, sometimes as a repressor (Elkon et al. 2015; Lee et al. 2015; Cichon et al. 2016), and most of the times as an inducer (Rapp et al. 2009; Wolfer et al. 2010; Yeh et al. 2011; Li et al. 2013; Andrews et al. 2017; Lin et al. 2017; Talamillo et al. 2017).

With all this contradictory data in mind, we first treated a panel of breast cancer cell lines that represent all the intrinsic molecular subtypes of breast cancer and present different levels of invasiveness. Omomyc was able to reduce the proliferation and clonogenic capacity in all of them independently of their subtype or metastatic capacity.

Actually, the degree of response, which differed significantly among cell lines, positively correlated with the levels of Omomyc expressed. For instance, metastatic MDA-MB-231 and non-metastatic MCF7 cells, which belong to the triple negative and luminal A subtypes respectively, showed the highest levels of Omomyc expression and their response was strong and comparable. On the other hand, the least responsive cells, MDA-MB-453 and T47D, showed either undetectable or extremely low levels of Omomyc. These observations suggest that all breast cancer cell lines tested are equally sensitive to the expression of Omomyc, in line with previous observations in other types of cancer and with our assumption that Myc is indispensable for the proliferation of all cancer cells.

To then challenge Omomyc with the worst case scenario, we used the triple negative, aggressive, metastatic, p53-, Kras-, Braf- and CDKN2A-mutated MDA-MB-231 cell line to characterize the phenotypic changes induced by Omomyc expression *in vitro* and *in vivo*. In this context, we showed that Omomyc reduces the levels of RNA polymerase III and induces its antiproliferative effect by arresting cells in the G0/G1 phase of the cell cycle and by reducing DNA incorporation during S phase, two observations that demonstrate a clear perturbation of Myc's functions. In fact, Myc is has been found to control the expression of RNA polymerases I, II and III (Oskarsson and Trumpp 2005), and is a master regulator of the cell cycle by controlling Cdks, cyclins and E2F transcription factors and antagonizing cell cycle inhibitors p21 and p27 (Bretones et al. 2015).

Then, in order to study Omomyc's impact on the metastatic phenotype *in vitro*, we focused on direct migration and invasion of tumor cells, as well as promotion of vasculogenesis. Regarding the latter, conditioned medium from cells expressing Omomyc heavily impaired tube formation in endothelial cells, consistent with Myc's role in promoting vasuculogenesis and angiogenesis through regulation of angiogenic factors such as VEGF, thrombospondin-1 and angiopoietin-1 (Baudino et al. 2002; Shchors et al. 2006). Three subsequent experiments demonstrated that Myc inhibition by Omomyc caused a profound reduction in directional migration of MDA-MB-231 cells (wound healing assay), which was more pronounced in the presence of chemoattractants (Boyden chamber assay), and even more strikingly in the presence of an extracellular matrix (ECM) (Matrigel-coated Boyden chamber assay). This implies that Myc is able to promote cell motility itself, as well as directional movement in a gradient of chemoattractant factors, and that these features can be blocked by the expression of Omomyc. More importantly, Myc inhibition is even more effective when an ECM is present, mimicking the environment that tumor cells find *in vivo*, suggesting that Myc might be implicated, for example, in the release of proteases needed for the

degradation of ECM in breast cancer (Duffy 1992). It has also been shown that, in NSCLC, c-Myc regulates BCYRN1, a long non-coding RNA that in turn controls the expression of metastasis-promoting matrix metalloproteinases MMP9 and MMP13 (Hu and Lu 2015), while in neuroblastoma N-Myc cooperates with Bcl-2 to increase the expression, secretion and activation of MMP2 (Noujaim et al. 2002). Furthermore, in epithelial cells, it is known that Myc inhibits the expression of E-cadherin and controls the expression of many other epithelial-to-mesenchymal (EMT) regulators including N-cadherin and Snail (Smith et al. 2009; Cho et al. 2010). Consistently, Omomyc expression in lung epithelial cells transformed with a knock down of p53, mutant $Kras^{G12V}$ and Myc was found to suppress EMT, decreasing expression of the metastasis-promoting ZEB1 gene at the RNA level, combined with an increase in CDH1, the gene encoding E-cadherin (Larsen et al. 2016). In addition, in colon carcinoma cell lines, Omomyc downregulates GLI1, a transcription factor responsible of inducing metastatic and stem-like phenotypes (Varnat et al. 2010).

Here we show that *in vivo* Omomyc behaved similarly. When challenged against fast-growing primary tumors, Omomyc reduced tumor expansion very significantly in the LM2-4175-derived orthotopic model and prevented tumor formation in the *MMTV-PyMT;TRE-Omomyc;βactin-rtTA* transgenic model almost completely, in line with recent data in the MMTV-Wnt1 mouse model of breast cancer, where expression of Omomyc induced a strong decrease in proliferation (von Eyss et al. 2015). Therefore, we have demonstrated the *in vivo* efficacy of Myc inhibition by Omomyc in two well-characterized breast cancer models, albeit with some differences in efficacy. Such differences could be due to several reasons, including intrinsic differences between the two models, not only in the nature of the models *per se*, but also in the experimental conditions used. First, in the cell-line derived model at treatment onset, tumors were already established and growing, while in genetically engineered mice tumors had not formed yet. This suggests that Omomyc could be more effective during the initial steps of tumorigenesis, which seems reasonable if inhibition of proliferation is one of its main mechanisms of action. Furthermore, *MMTV-PyMT;TRE-Omomyc;βactin-rtTA* mice present transgene leakiness and express Omomyc even in the absence of doxycycline, meaning that, although the levels are lower than after induction, Omomyc is potentially active since mice are born, or even during embryogenesis. We know that Omomyc expression impairs embryonic development, meaning that low “leaky” levels are not enough to interfere with embryogenesis but can impede tumor formation. Second, unlike BALB/c nude mice, transgenic mice possess a functional immune system and it has been shown that Myc deregulation in cancer cells promotes tumorigenesis not only

in a cell-autonomous manner, but also acting on the immune cells and other components of the tumor microenvironment (Sodir et al. 2011; Casey et al. 2017). Third, expression of Omomyc is restricted to cancer cells in LM2-4175 tumors, while *MMTV-PyMT;TRE-Omomyc;βactin-rtTA* mice might express Omomyc in other cellular components including endothelial cells, fibroblasts and immune cells. Therefore, just as Myc inhibition in cancer cells modulates the tumor microenvironment, Myc inhibition in the tumor microenvironment could affect tumor maintenance through inhibition of angiogenesis, fibrosis or immune escape. Finally, the LM2-4175-derived models clearly represent the triple negative subtype of breast cancer, while the *MMTV-PyMT* model, despite not representing a defined human type of breast cancer, shows a near significant association with the human luminal gene expression profile and is significantly anti-correlated with the human basal-like (triple negative) subtype (Herschkowitz et al. 2007), proving that both models present substantial differences in terms of gene expression.

Despite these variables, though, the overarching goal of this part of the thesis was to demonstrate the utility of inhibiting Myc in the metastatic setting *in vivo*. To this aim, we made use of three different metastatic models. In our lung-colonization model, we designed an experiment to assess the capacity of Omomyc to prevent the establishment of lung lesions after breast cancer cells had colonized the lung. In this model, LM2-4175 cells inoculated trough intravenous injection localize in the lungs within minutes. However, many cells fail to survive and the luciferase signal decreases over a period of one week. At that point, we treated the mice with doxycycline to induce the expression of Omomyc in order to see if the cells that had survived retained the capacity to still grow and thrive, with the objective of mimicking incipient metastases found in breast cancer patients. Unlike normal LM2-4175 cells, which grew exponentially, Omomyc-expressing cells showed a dramatic decrease in proliferation similar to that exerted in LM2-4175 primary tumors, demonstrating that Omomyc was able to control the disease, without eradicating it, in immunocompromised hosts. In the second model we treated established metastases after resection of the primary tumors. In this case, Omomyc unveiled its full potential by making established lesions shrink and, in some cases, eradicating them completely. These data are extremely encouraging since, in this model, metastases had established through the natural process of escaping the primary tumor and colonizing a secondary organ, recapitulating what occurs in patients.

As previously mentioned, however, some reports claim that Myc, while promoting primary tumor growth, impairs metastasis, suggesting that Myc inhibition reduces primary tumor growth but enhances invasiveness (Liu et al. 2012). Although we have demonstrated that Omomyc is able to reduce the metastatic features of breast cancer cells *in vitro*, the two *in vivo* models described so far do not definitely contradict this observation, since treated lesions were already present at the time of Omomyc activation and we did not directly assess migration of Omomyc-expressing cancer cells to secondary organs *in vivo*. To clarify this point, we decided to make use of our immunocompetent *MMTV-PyMT;TRE-Omomyc;βactin-rtTA* mouse model to study the invasion process. Given the impossibility of turning off the expression of Omomyc completely, we could not perform an intervention study in established metastases. Instead, we were able to analyze the capacity of Omomyc to prevent the escape of tumor cells from incipient tumors and form lung metastases, and proved that metastatic formation was prevented almost completely in the presence of Omomyc, recapitulating our findings *in vitro*.

Although Omomyc has proven efficacious against multiple mouse models of cancer, and we have shown here that it could also be employed against metastasis, it has been simply considered a valid proof of principle for Myc inhibition, but with no possibility of becoming a viable pharmacological approach. That was until very recently, when Dr. Marie-Eve Beaulieu, a postdoc in Dr. Soucek's laboratory, showed that the purified Omomyc peptide, Omomyc^{CPP}, displayed cell-penetrating properties and had the innate capacity to enter into NSCLC cells both *in vitro* and *in vivo*, localize in their nuclei and interfere with Myc transactivation, causing a therapeutic impact in mouse models of lung cancer (Beaulieu et al, under review). Here we have shown that these features are recapitulated in mouse models of triple negative breast cancer as well. More in detail, *in vitro*, we have demonstrated that Omomyc^{CPP} penetrates into MDA-MB-231 cells in a dose-dependent manner, interfering with cell proliferation, phenocopying the effects of lentivirally-expressed Omomyc. Fusion with the metastasis targeting, cell-penetrating peptide TMTP1 enhanced Omomyc's penetration, conserved its anti-proliferative effect and in addition, promoted cell death in MDA-MB-231 cells. This was consistent with previous characterization of this 5 amino acid sequence, in which TMTP1 was found to bind specifically to malignant hematopoietic cells, causing apoptosis by itself, but not to normal umbilical cord blood mononuclear cells (Xiao et al. 2011). Importantly, the TMTP1 sequence was previously used as a carrier of therapeutic peptides that successfully inhibited cell proliferation of highly metastatic breast, prostate and gastric cancer cells *in vitro* and *in vivo* (Liu et al. 2012; Ma et al. 2012; Ma et al. 2013; Liu et al.

2014). For these reasons, we decided to test our fusion peptide TMTP1-Omomyc *in vivo* as the first Omomyc-based drug against metastatic breast cancer. TMTP1-Omomyc was able to slow down the growth of LM2-4175-derived primary tumors and lung metastases by intratumoral injection and intranasal instillation respectively, without causing weight loss or any noticeable side effect. To mimic the treatment of breast cancer patients harboring metastases, we made use of our lung colonization model, treating the mice 3 weeks after inoculation, when lung tumors were already established and growing exponentially. In this setting, TMTP1-Omomyc behaved similarly to paclitaxel, the standard of care for TNBC. However, no evident additive effect or synergy was observed when both drugs were combined, although it is important to notice that this experimental model showed high levels of variability in terms of luciferase activity at treatment onset, which masked the effects of the treatment when analyzing statistical differences among groups. In spite of this drawback, IVIS and μCT data clearly show the potential of this new anti-Myc compound against metastatic TNBC, in line with previous reports showing that indirect inhibition of Myc is extremely effective in the treatment of TNBC models (Horiuchi et al. 2016).

In conclusion, this work demonstrates that Myc inhibition by Omomyc is a safe and effective therapy against breast cancer by impairing cell proliferation, angiogenesis, migration and invasion *in vitro*, dramatically reducing primary tumor and metastatic growth in immunocompromised mice, even eradicating established metastases, and preventing primary tumor and metastatic growth almost completely in immunocompetent mice. Thus, we have demonstrated for the first time the applicability of Omomyc against metastasis, challenging the pre-established notion that Myc inhibition could potentiate, rather than inhibit, invasion. Finally, we have validated TMTP1-Omomyc as the first directly-deliverable Omomyc-based drug for the treatment of metastatic TNBC, providing a new therapeutic opportunity for patients suffering from this dreadful and incurable disease.

CONCLUSIONS

1 PART 1

- Ibrutinib blocks mast cell degranulation in PDAC-bearing mice.
- Ibrutinib induces a remarkable reduction in proliferation, infiltration of inflammatory cells and collagen deposition in the tumor stroma.
- Ibrutinib extends the survival of mice bearing PDAC, as monotherapy and in combination with gemcitabine, and is therefore a promising therapeutic approach.
- The therapeutic activity of ibrutinib is dependent on the tumor stroma.
- This work provides pre-clinical evidence for the use of ibrutinib – which is already approved for clinical use – in the treatment of PDAC, and potentially other fibrotic diseases.

2 PART 2

- Myc inhibition induces a decrease in proliferation of cell lines from all molecular subtypes of breast cancer. This decrease is caused by an arrest in G0/G1 and a reduction in DNA synthesis during the S phase of the cell cycle.
- Myc inhibition by Omomyc decreases the cells' capacity to migrate, invade and induce angiogenesis *in vitro*.
- Omomyc expression delays growth of primary tumors in an orthotopic mouse model of breast cancer and causes regression of established metastases after primary tumor resection.
- Omomyc expression prevents expansion of lung lesions in a lung colonization mouse model of breast cancer.
- Omomyc expression prevents the appearance of mammary tumors and lung metastases in the *MMTV-PyMT* transgenic mouse model.
- The Omomyc peptide has the ability to penetrate into breast cancer cells in a dose dependent manner and localize in their nuclei, recapitulating the effects of the Omomyc transgene in cell cycle blockade and proliferation arrest.
- Fusion of Omomyc^{CPP} with the metastasis-targeting peptide TMTP1 enhances its cell-penetrating capacity in metastatic cells and delays primary tumor and metastatic growth *in vivo*, constituting a new therapeutic opportunity for TNBC patients.

BIBLIOGRAPHY

Abramson, V. G., B. D. Lehmann, et al. (2015). "Subtyping of triple-negative breast cancer: implications for therapy." Cancer **121**(1): 8-16.

Alexakis, N., C. Halloran, et al. (2004). "Current standards of surgery for pancreatic cancer." Br J Surg **91**(11): 1410-1427.

Alves Rde, C., R. T. Meurer, et al. (2014). "MYC amplification is associated with poor survival in small cell lung cancer: a chromogenic in situ hybridization study." J Cancer Res Clin Oncol **140**(12): 2021-2025.

Andrews, F. H., A. R. Singh, et al. (2017). "Dual-activity PI3K-BRD4 inhibitor for the orthogonal inhibition of MYC to block tumor growth and metastasis." Proc Natl Acad Sci U S A **114**(7): E1072-E1080.

Annibali, D., J. R. Whitfield, et al. (2014). "Myc inhibition is effective against glioma and reveals a role for Myc in proficient mitosis." Nat Commun **5**: 4632.

Arumugam, T., V. Ramachandran, et al. (2006). "Effect of cromolyn on S100P interactions with RAGE and pancreatic cancer growth and invasion in mouse models." J Natl Cancer Inst **98**(24): 1806-1818.

Attramadal, C. G., S. Kumar, et al. (2016). "Low Mast Cell Density Predicts Poor Prognosis in Oral Squamous Cell Carcinoma and Reduces Survival in Head and Neck Squamous Cell Carcinoma." Anticancer Res **36**(10): 5499-5506.

Aulmann, S., N. Adler, et al. (2006). "c-myc amplifications in primary breast carcinomas and their local recurrences." J Clin Pathol **59**(4): 424-428.

Bachmanov, A. A., D. R. Reed, et al. (2002). "Food intake, water intake, and drinking spout side preference of 28 mouse strains." Behav Genet **32**(6): 435-443.

Bataller, R. and D. A. Brenner (2005). "Liver fibrosis." J Clin Invest **115**(2): 209-218.

Baudino, T. A., C. McKay, et al. (2002). "c-Myc is essential for vasculogenesis and angiogenesis during development and tumor progression." Genes Dev **16**(19): 2530-2543.

Beaulieu, M. E., T. Jauset, et al. (2016). Mouse Models in Personalized Cancer Medicine. Cancer Genetics and Genomics for Personalized Medicine, CRC Press**:** 103-143.

Ben-Porath, I., M. W. Thomson, et al. (2008). "An embryonic stem cell-like gene expression signature in poorly differentiated aggressive human tumors." Nat Genet **40**(5): 499-507.

Borg, A., B. Baldetorp, et al. (1992). "c-myc amplification is an independent prognostic factor in postmenopausal breast cancer." Int J Cancer **51**(5): 687-691.

Bos, P. D., X. H. Zhang, et al. (2009). "Genes that mediate breast cancer metastasis to the brain." Nature **459**(7249): 1005-1009.

Bourhis, J., M. G. Le, et al. (1990). "Prognostic value of c-myc proto-oncogene overexpression in early invasive carcinoma of the cervix." J Clin Oncol **8**(11): 1789-1796.

Bretones, G., M. D. Delgado, et al. (2015). "Myc and cell cycle control." Biochim Biophys Acta **1849**(5): 506-516.

Burger, J. A., A. Tedeschi, et al. (2015). "Ibrutinib as Initial Therapy for Patients with Chronic Lymphocytic Leukemia." N Engl J Med **373**(25): 2425-2437.

Cai, S. W., S. Z. Yang, et al. (2011). "Prognostic significance of mast cell count following curative resection for pancreatic ductal adenocarcinoma." Surgery **149**(4): 576-584.

Cappellen, D., T. Schlange, et al. (2007). "Novel c-MYC target genes mediate differential effects on cell proliferation and migration." EMBO Rep **8**(1): 70-76.

Casey, S. C., V. Baylot, et al. (2017). "MYC: Master Regulator of Immune Privilege." Trends Immunol **38**(4): 298-305.

Cejalvo, J. M., E. Martinez de Duenas, et al. (2017). "Intrinsic subtypes and gene expression profiles in primary and metastatic breast cancer." Cancer Res.

Cichon, M. A., M. E. Moruzzi, et al. (2016). "MYC Is a Crucial Mediator of TGFbeta-Induced Invasion in Basal Breast Cancer." Cancer Res **76**(12): 3520-3530.

Clahsen, T. and F. Schaper (2008). "Interleukin-6 acts in the fashion of a classical chemokine on monocytic cells by inducing integrin activation, cell adhesion, actin polymerization, chemotaxis, and transmigration." J Leukoc Biol **84**(6): 1521-1529.

Corzo, C., J. M. Corominas, et al. (2006). "The MYC oncogene in breast cancer progression: from benign epithelium to invasive carcinoma." Cancer Genet Cytogenet **165**(2): 151-156.

Courtneidge, S. A. and A. E. Smith (1983). "Polyoma virus transforming protein associates with the product of the c-src cellular gene." Nature **303**(5916): 435-439.

Cowling, V. H. and M. D. Cole (2007). "E-cadherin repression contributes to c-Myc-induced epithelial cell transformation." Oncogene **26**(24): 3582-3586.

Chan, C. H., S. W. Lee, et al. (2010). "Deciphering the transcriptional complex critical for RhoA gene expression and cancer metastasis." Nat Cell Biol **12**(5): 457-467.

Chan, J. K., A. Magistris, et al. (2005). "Mast cell density, angiogenesis, blood clotting, and prognosis in women with advanced ovarian cancer." Gynecol Oncol **99**(1): 20-25.

Chang, B. Y., M. M. Huang, et al. (2011). "The Bruton tyrosine kinase inhibitor PCI-32765 ameliorates autoimmune arthritis by inhibition of multiple effector cells." Arthritis Res Ther **13**(4): R115.

Chang, D. Z., Y. Ma, et al. (2011). "Mast cells in tumor microenvironment promotes the in vivo growth of pancreatic ductal adenocarcinoma." Clin Cancer Res **17**(22): 7015-7023.

Chen, J., T. Kinoshita, et al. (2016). "Ibrutinib Inhibits ERBB Receptor Tyrosine Kinases and HER2-Amplified Breast Cancer Cell Growth." Mol Cancer Ther **15**(12): 2835-2844.

Chen, J., T. Willingham, et al. (1995). "Effects of the MYC oncogene antagonist, MAD, on proliferation, cell cycling and the malignant phenotype of human brain tumour cells." Nat Med **1**(7): 638-643.

Chen, K., Y. Wei, et al. (2007). "Decreasing TNF-alpha results in less fibrosis and earlier resolution of granulomatous experimental autoimmune thyroiditis." J Leukoc Biol **81**(1): 306-314.

Cheng, S. W., K. P. Davies, et al. (1999). "c-MYC interacts with INI1/hSNF5 and requires the SWI/SNF complex for transactivation function." Nat Genet **22**(1): 102-105.

Cho, K. B., M. K. Cho, et al. (2010). "Overexpression of c-myc induces epithelial mesenchymal transition in mammary epithelial cells." Cancer Lett **293**(2): 230-239.

Choi, S. Y., D. Lin, et al. (2014). "Lessons from patient-derived xenografts for better in vitro modeling of human cancer." Adv Drug Deliv Rev **79-80**: 222-237.

Christophorou, M. A., D. Martin-Zanca, et al. (2005). "Temporal dissection of p53 function in vitro and in vivo." Nat Genet **37**(7): 718-726.

Dang, C. V., K. A. O'Donnell, et al. (2006). "The c-Myc target gene network." Semin Cancer Biol **16**(4): 253-264.

DeRuiter, J., P. Holston, et al. (2014). "Review of Selected NMEs 2014." US Pharm **2014**(39(10)): HS2-HS14.

Dilworth, S. M. (2002). "Polyoma virus middle T antigen and its role in identifying cancer-related molecules." Nat Rev Cancer **2**(12): 951-956.

Distler, J. H., G. Schett, et al. (2008). "The controversial role of tumor necrosis factor alpha in fibrotic diseases." Arthritis Rheum **58**(8): 2228-2235.

Duffy, M. J. (1992). "The role of proteolytic enzymes in cancer invasion and metastasis." Clin Exp Metastasis **10**(3): 145-155.

Elkon, R., F. Loayza-Puch, et al. (2015). "Myc coordinates transcription and translation to enhance transformation and suppress invasiveness." EMBO Rep **16**(12): 1723-1736.

Evans, A. and E. Costello (2012). "The role of inflammatory cells in fostering pancreatic cancer cell growth and invasion." Front Physiol **3**: 270.

Ferlay J, S. I., Ervik M, Dikshit R, Eser S, Mathers C, Rebelo M, Parkin DM, Forman D, and Bray F (2013). "GLOBOCAN 2012 v1.0, Cancer Incidence and Mortality Worldwide: IARC CancerBase No. 11 [Internet]. Lyon, France." International Agency for Research on Cancer(Available from http://globocan.iarc.fr).

Ferreira, A. M., S. Takagawa, et al. (2006). "Diminished induction of skin fibrosis in mice with MCP-1 deficiency." J Invest Dermatol **126**(8): 1900-1908.

Fiorentino, F. P., E. Tokgun, et al. (2016). "Growth suppression by MYC inhibition in small cell lung cancer cells with TP53 and RB1 inactivation." Oncotarget **7**(21): 31014-31028.

Gaca, M. D., X. Zhou, et al. (2002). "Regulation of hepatic stellate cell proliferation and collagen synthesis by proteinase-activated receptors." J Hepatol **36**(3): 362-369.

Galardi, S., M. Savino, et al. (2016). "Resetting cancer stem cell regulatory nodes upon MYC inhibition." EMBO Rep **17**(12): 1872-1889.

Galinsky, D. S. and H. Nechushtan (2008). "Mast cells and cancer--no longer just basic science." Crit Rev Oncol Hematol **68**(2): 115-130.

Gao, W., M. Wang, et al. (2014). "Selective antitumor activity of ibrutinib in EGFR-mutant non-small cell lung cancer cells." J Natl Cancer Inst **106**(9).

Gilfillan, A. M. and C. Tkaczyk (2006). "Integrated signalling pathways for mast-cell activation." Nat Rev Immunol **6**(3): 218-230.

Gnanaprakasam, J. N. and R. Wang (2017). "MYC in Regulating Immunity: Metabolism and Beyond." Genes (Basel) **8**(3).

Gogas, H., V. Kotoula, et al. (2016). "MYC copy gain, chromosomal instability and PI3K activation as potential markers of unfavourable outcome in trastuzumab-treated patients with metastatic breast cancer." J Transl Med **14**(1): 136.

Goldhirsch, A., E. P. Winer, et al. (2013). "Personalizing the treatment of women with early breast cancer: highlights of the St Gallen International Expert Consensus on the Primary Therapy of Early Breast Cancer 2013." Ann Oncol **24**(9): 2206-2223.

Goldhirsch, A., W. C. Wood, et al. (2011). "Strategies for subtypes--dealing with the diversity of breast cancer: highlights of the St. Gallen International Expert Consensus on the Primary Therapy of Early Breast Cancer 2011." Ann Oncol **22**(8): 1736-1747.

Gomez-Roman, N., C. Grandori, et al. (2003). "Direct activation of RNA polymerase III transcription by c-Myc." Nature **421**(6920): 290-294.

Green, A. R., M. A. Aleskandarany, et al. (2016). "MYC functions are specific in biological subtypes of breast cancer and confers resistance to endocrine therapy in luminal tumours." Br J Cancer **114**(8): 917-928.

Grimbaldeston, M. A., A. L. Pearce, et al. (2004). "Association between melanoma and dermal mast cell prevalence in sun-unexposed skin." Br J Dermatol **150**(5): 895-903.

Gunderson, A. J., M. M. Kaneda, et al. (2016). "Bruton Tyrosine Kinase-Dependent Immune Cell Cross-talk Drives Pancreas Cancer." Cancer Discov **6**(3): 270-285.

Guy, C. T., R. D. Cardiff, et al. (1992). "Induction of mammary tumors by expression of polyomavirus middle T oncogene: a transgenic mouse model for metastatic disease." Mol Cell Biol **12**(3): 954-961.

Guzman, C., M. Bagga, et al. (2014). "ColonyArea: an ImageJ plugin to automatically quantify colony formation in clonogenic assays." PLoS One **9**(3): e92444.

Hamilton, S. R. and L. A. Aaltonen (2000). Pathology and genetics of tumours of the digestive system. World Health Organization Classification of Tumours. Lyon, IARC Press.

Hanahan, D. and R. A. Weinberg (2011). "Hallmarks of cancer: the next generation." Cell **144**(5): 646-674.

Hariharan, D., A. Saied, et al. (2008). "Analysis of mortality rates for pancreatic cancer across the world." HPB (Oxford) **10**(1): 58-62.

He, C., H. Jiang, et al. (2014). "Expression and prognostic value of c-Myc and Fas (CD95/APO1) in patients with pancreatic cancer." Int J Clin Exp Pathol **7**(2): 742-750.

Herreros-Villanueva, M., E. Hijona, et al. (2012). "Mouse models of pancreatic cancer." World J Gastroenterol **18**(12): 1286-1294.

Herschkowitz, J. I., K. Simin, et al. (2007). "Identification of conserved gene expression features between murine mammary carcinoma models and human breast tumors." Genome Biol **8**(5): R76.

Hingorani, S. R., E. F. Petricoin, et al. (2003). "Preinvasive and invasive ductal pancreatic cancer and its early detection in the mouse." Cancer Cell **4**(6): 437-450.

Hingorani, S. R., L. Wang, et al. (2005). "Trp53R172H and KrasG12D cooperate to promote chromosomal instability and widely metastatic pancreatic ductal adenocarcinoma in mice." Cancer Cell **7**(5): 469-483.

Homma, T., H. Harada, et al. (1997). "Diagnostic criteria for chronic pancreatitis by the Japan Pancreas Society." Pancreas **15**(1): 14-15.

Honigberg, L. A., A. M. Smith, et al. (2010). "The Bruton tyrosine kinase inhibitor PCI-32765 blocks B-cell activation and is efficacious in models of autoimmune disease and B-cell malignancy." Proc Natl Acad Sci U S A **107**(29): 13075-13080.

Horiuchi, D., R. Camarda, et al. (2016). "PIM1 kinase inhibition as a targeted therapy against triple-negative breast tumors with elevated MYC expression." Nat Med **22**(11): 1321-1329.

Horiuchi, D., L. Kusdra, et al. (2012). "MYC pathway activation in triple-negative breast cancer is synthetic lethal with CDK inhibition." J Exp Med **209**(4): 679-696.

Hotz, H. G., H. A. Reber, et al. (2003). "An orthotopic nude mouse model for evaluating pathophysiology and therapy of pancreatic cancer." Pancreas **26**(4): e89-98.

Hsieh, A. L. and C. V. Dang (2016). "MYC, Metabolic Synthetic Lethality, and Cancer." Recent Results Cancer Res **207**: 73-91.

Hu, T. and Y. R. Lu (2015). "BCYRN1, a c-MYC-activated long non-coding RNA, regulates cell metastasis of non-small-cell lung cancer." Cancer Cell Int **15**: 36.

Hugle, T. (2014). "Beyond allergy: the role of mast cells in fibrosis." Swiss Med Wkly **144**: w13999.

Hutchinson, J. N. and W. J. Muller (2000). "Transgenic mouse models of human breast cancer." Oncogene **19**(53): 6130-6137.

Iorns, E., K. Drews-Elger, et al. (2012). "A new mouse model for the study of human breast cancer metastasis." PLoS One **7**(10): e47995.

Iwaki, S., C. Tkaczyk, et al. (2005). "Btk plays a crucial role in the amplification of Fc epsilonRI-mediated mast cell activation by kit." J Biol Chem **280**(48): 40261-40270.

Jackson, E. L., N. Willis, et al. (2001). "Analysis of lung tumor initiation and progression using conditional expression of oncogenic K-ras." Genes Dev **15**(24): 3243-3248.

Jensen, B. M., M. A. Beaven, et al. (2008). "Concurrent inhibition of kit- and FcepsilonRI-mediated signaling: coordinated suppression of mast cell activation." J Pharmacol Exp Ther **324**(1): 128-138.

Johansson, A., S. Rudolfsson, et al. (2010). "Mast cells are novel independent prognostic markers in prostate cancer and represent a target for therapy." Am J Pathol **177**(2): 1031-1041.

Joosse, S. A., T. M. Gorges, et al. (2015). "Biology, detection, and clinical implications of circulating tumor cells." EMBO Mol Med **7**(1): 1-11.

Joyce, J. A. and J. W. Pollard (2009). "Microenvironmental regulation of metastasis." Nat Rev Cancer **9**(4): 239-252.

Jung, L. A., A. Gebhardt, et al. (2017). "OmoMYC blunts promoter invasion by oncogenic MYC to inhibit gene expression characteristic of MYC-dependent tumors." Oncogene **36**(14): 1911-1924.

Kanazawa, S., L. Soucek, et al. (2003). "c-Myc recruits P-TEFb for transcription, cellular proliferation and apoptosis." Oncogene **22**(36): 5707-5711.

Kang, Y., P. M. Siegel, et al. (2003). "A multigenic program mediating breast cancer metastasis to bone." Cancer Cell **3**(6): 537-549.

Kim, I. S. and S. H. Baek (2010). "Mouse models for breast cancer metastasis." Biochem Biophys Res Commun **394**(3): 443-447.

Kleeff, J., M. Korc, et al. (2016). "Pancreatic cancer." Nat Rev Dis Primers **2**: 16022.

Kohl, N. E., N. Kanda, et al. (1983). "Transposition and amplification of oncogene-related sequences in human neuroblastomas." Cell **35**(2 Pt 1): 359-367.

Kong, L. M., C. G. Liao, et al. (2014). "A regulatory loop involving miR-22, Sp1, and c-Myc modulates CD147 expression in breast cancer invasion and metastasis." Cancer Res **74**(14): 3764-3778.

Koong, A. C., V. K. Mehta, et al. (2000). "Pancreatic tumors show high levels of hypoxia." Int J Radiat Oncol Biol Phys **48**(4): 919-922.

Kozma, L., I. Kiss, et al. (1994). "Investigation of c-myc oncogene amplification in colorectal cancer." Cancer Lett **81**(2): 165-169.

Langley, R. R. and I. J. Fidler (2011). "The seed and soil hypothesis revisited--the role of tumor-stroma interactions in metastasis to different organs." Int J Cancer **128**(11): 2527-2535.

Larsen, J. E., V. Nathan, et al. (2016). "ZEB1 drives epithelial-to-mesenchymal transition in lung cancer." J Clin Invest **126**(9): 3219-3235.

Lee, E., S. J. Lee, et al. (2014). "Inhibition of breast cancer growth and metastasis by a biomimetic peptide." Sci Rep **4**: 7139.

Lee, M., S. M. Beggs, et al. (2015). "Necdin is a breast cancer metastasis suppressor that regulates the transcription of c-Myc." Oncotarget **6**(31): 31557-31568.

Li, F., T. Cheng, et al. (2015). "Evaluation of (99m)Tc-HYNIC-TMTP1 as a tumor-homing imaging agent targeting metastasis with SPECT." Nucl Med Biol **42**(3): 256-262.

Li, X., X. Liu, et al. (2013). "c-MYC-regulated miR-23a/24-2/27a cluster promotes mammary carcinoma cell invasion and hepatic metastasis by targeting Sprouty2." J Biol Chem **288**(25): 18121-18133.

Li, Y., D. Zhang, et al. (2016). "Syntheses and preliminary evaluation of [(18) F]AlF-NOTA-G-TMTP1 for PET imaging of high aggressive hepatocellular carcinoma." Contrast Media Mol Imaging **11**(4): 262-271.

Lin, X., R. Sun, et al. (2017). "C-myc overexpression drives melanoma metastasis by promoting vasculogenic mimicry via c-myc/snail/Bax signaling." J Mol Med (Berl) **95**(1): 53-67.

Liu, H., D. C. Radisky, et al. (2012). "MYC suppresses cancer metastasis by direct transcriptional silencing of alphav and beta3 integrin subunits." Nat Cell Biol **14**(6): 567-574.

Liu, R., X. Ma, et al. (2014). "The novel fusion protein sTRAIL-TMTP1 exhibits a targeted inhibition of primary tumors and metastases." J Mol Med (Berl) **92**(2): 165-175.

Liu, R., L. Xi, et al. (2012). "Enhanced targeted anticancer effects and inhibition of tumor metastasis by the TMTP1 compound peptide TMTP1-TAT-NBD." J Control Release **161**(3): 893-902.

Lu, J., P. S. Steeg, et al. (2009). "Breast cancer metastasis: challenges and opportunities." Cancer Res **69**(12): 4951-4953.

Lloyd, C. M., M. E. Dorf, et al. (1997). "Role of MCP-1 and RANTES in inflammation and progression to fibrosis during murine crescentic nephritis." J Leukoc Biol **62**(5): 676-680.

Ma, X., P. Lv, et al. (2013). "DT390-triTMTP1, a novel fusion protein of diphtheria toxin with tandem repeat TMTP1 peptide, preferentially targets metastatic tumors." Mol Pharm **10**(1): 115-126.

Ma, X., L. Xi, et al. (2012). "Anti-tumor effects of the peptide TMTP1-GG-D(KLAKLAK)(2) on highly metastatic cancers." PLoS One **7**(9): e42685.

Ma, Y., R. F. Hwang, et al. (2013). "Dynamic mast cell-stromal cell interactions promote growth of pancreatic cancer." Cancer Res **73**(13): 3927-3937.

Mahadevan, D. and D. D. Von Hoff (2007). "Tumor-stroma interactions in pancreatic ductal adenocarcinoma." Mol Cancer Ther **6**(4): 1186-1197.

Malvezzi, M., G. Carioli, et al. (2017). "European cancer mortality predictions for the year 2017, with focus on lung cancer." Ann Oncol.

Marino, N., S. Woditschka, et al. (2013). "Breast cancer metastasis: issues for the personalization of its prevention and treatment." Am J Pathol **183**(4): 1084-1095.

Masso-Valles, D., T. Jauset, et al. (2015). "Ibrutinib exerts potent antifibrotic and antitumor activities in mouse models of pancreatic adenocarcinoma." Cancer Res **75**(8): 1675-1681.

Masso-Valles, D., T. Jauset, et al. (2016). "Ibrutinib repurposing: from B-cell malignancies to solid tumors." Oncoscience **3**(5-6): 147-148.

McMahon, S. B., M. A. Wood, et al. (2000). "The essential cofactor TRRAP recruits the histone acetyltransferase hGCN5 to c-Myc." Mol Cell Biol **20**(2): 556-562.

Mellon, P., A. Pawson, et al. (1978). "Specific RNA sequences and gene products of MC29 avian acute leukemia virus." Proc Natl Acad Sci U S A **75**(12): 5874-5878.

Metz, D. C. and R. T. Jensen (2008). "Gastrointestinal neuroendocrine tumors: pancreatic endocrine tumors." Gastroenterology **135**(5): 1469-1492.

Meyer, N. and L. Z. Penn (2008). "Reflecting on 25 years with MYC." Nat Rev Cancer **8**(12): 976-990.

Minn, A. J., G. P. Gupta, et al. (2005). "Genes that mediate breast cancer metastasis to lung." Nature **436**(7050): 518-524.

Montagne, M., N. Beaudoin, et al. (2012). "The Max b-HLH-LZ can transduce into cells and inhibit c-Myc transcriptional activities." PLoS One **7**(2): e32172.

Murphy, D. J., M. R. Junttila, et al. (2008). "Distinct thresholds govern Myc's biological output in vivo." Cancer Cell **14**(6): 447-457.

Nair, R., D. L. Roden, et al. (2014). "c-Myc and Her2 cooperate to drive a stem-like phenotype with poor prognosis in breast cancer." Oncogene **33**(30): 3992-4002.

Nair, S. K. and S. K. Burley (2003). "X-ray structures of Myc-Max and Mad-Max recognizing DNA. Molecular bases of regulation by proto-oncogenic transcription factors." Cell **112**(2): 193-205.

Nau, M. M., B. J. Brooks, et al. (1985). "L-myc, a new myc-related gene amplified and expressed in human small cell lung cancer." Nature **318**(6041): 69-73.

Nobili, V., M. Marcellini, et al. (2004). "Association of serum interleukin-8 levels with the degree of fibrosis in infants with chronic liver disease." J Pediatr Gastroenterol Nutr **39**(5): 540-544.

Noujaim, D., C. M. van Golen, et al. (2002). "N-Myc and Bcl-2 coexpression induces MMP-2 secretion and activation in human neuroblastoma cells." Oncogene **21**(29): 4549-4557.

Oberg, K. and B. Eriksson (2005). "Endocrine tumours of the pancreas." Best Pract Res Clin Gastroenterol **19**(5): 753-781.

Oikonomou, N., V. Harokopos, et al. (2006). "Soluble TNF mediates the transition from pulmonary inflammation to fibrosis." PLoS One **1**: e108.

Ooe, A., S. Takahara, et al. (2012). "Relationship between intrinsic subtypes and tumor responses to neoadjuvant chemotherapy in patients with locally advanced breast cancer." Breast Dis **34**(1): 9-17.
Oskarsson, T. and A. Trumpp (2005). "The Myc trilogy: lord of RNA polymerases." Nat Cell Biol **7**(3): 215-217.
Overed-Sayer, C., L. Rapley, et al. (2013). "Are mast cells instrumental for fibrotic diseases?" Front Pharmacol **4**: 174.
Paget, S. (1989). "The distribution of secondary growths in cancer of the breast. 1889." Cancer Metastasis Rev **8**(2): 98-101.
Park, S., J. S. Koo, et al. (2012). "Characteristics and outcomes according to molecular subtypes of breast cancer as classified by a panel of four biomarkers using immunohistochemistry." Breast **21**(1): 50-57.
Parker, A., O. J. Maclaren, et al. (2017). "Cell proliferation within small intestinal crypts is the principal driving force for cell migration on villi." FASEB J **31**(2): 636-649.
Patel, J. H., A. P. Loboda, et al. (2004). "Analysis of genomic targets reveals complex functions of MYC." Nat Rev Cancer **4**(7): 562-568.
Pelengaris, S., M. Khan, et al. (2002). "Suppression of Myc-induced apoptosis in beta cells exposes multiple oncogenic properties of Myc and triggers carcinogenic progression." Cell **109**(3): 321-334.
Pereira, C. B., M. F. Leal, et al. (2013). "Prognostic and predictive significance of MYC and KRAS alterations in breast cancer from women treated with neoadjuvant chemotherapy." PLoS One **8**(3): e60576.
Peukert, K., P. Staller, et al. (1997). "An alternative pathway for gene regulation by Myc." EMBO J **16**(18): 5672-5686.
Phillips, P. (2012). Pancreatic stellate cells and fibrosis. Pancreatic Cancer and Tumor Microenvironment. P. J. Grippo and H. G. Munshi. Trivandrum (India).
Podsypanina, K., K. Politi, et al. (2008). "Oncogene cooperation in tumor maintenance and tumor recurrence in mouse mammary tumors induced by Myc and mutant Kras." Proc Natl Acad Sci U S A **105**(13): 5242-5247.
Ponomarev, V., M. Doubrovin, et al. (2004). "A novel triple-modality reporter gene for whole-body fluorescent, bioluminescent, and nuclear noninvasive imaging." Eur J Nucl Med Mol Imaging **31**(5): 740-751.
Posternak, V. and M. D. Cole (2016). "Strategically targeting MYC in cancer." F1000Res **5**.
Pradere, J. P., J. Kluwe, et al. (2013). "Hepatic macrophages but not dendritic cells contribute to liver fibrosis by promoting the survival of activated hepatic stellate cells in mice." Hepatology **58**(4): 1461-1473.
Prat, A., M. J. Ellis, et al. (2011). "Practical implications of gene-expression-based assays for breast oncologists." Nat Rev Clin Oncol **9**(1): 48-57.
Prat, A. and C. M. Perou (2011). "Deconstructing the molecular portraits of breast cancer." Mol Oncol **5**(1): 5-23.
Prochownik, E. V. and P. K. Vogt (2010). "Therapeutic Targeting of Myc." Genes Cancer **1**(6): 650-659.
Psaila, B., R. N. Kaplan, et al. (2006). "Priming the 'soil' for breast cancer metastasis: the pre-metastatic niche." Breast Dis **26**: 65-74.
Qiu, W. and G. H. Su (2013). "Development of orthotopic pancreatic tumor mouse models." Methods Mol Biol **980**: 215-223.
Rabenhorst, A., M. Schlaak, et al. (2012). "Mast cells play a protumorigenic role in primary cutaneous lymphoma." Blood **120**(10): 2042-2054.
Rahl, P. B., C. Y. Lin, et al. (2010). "c-Myc regulates transcriptional pause release." Cell **141**(3): 432-445.
Rajput, A. B., D. A. Turbin, et al. (2008). "Stromal mast cells in invasive breast cancer are a marker of favourable prognosis: a study of 4,444 cases." Breast Cancer Res Treat **107**(2): 249-257.

Rapp, U. R., C. Korn, et al. (2009). "MYC is a metastasis gene for non-small-cell lung cancer." PLoS One **4**(6): e6029.

Ren, J., F. Jin, et al. (2013). "MYC overexpression and poor prognosis in sporadic breast cancer with BRCA1 deficiency." Tumour Biol **34**(6): 3945-3958.

Ribatti, D. and E. Crivellato (2009). "The controversial role of mast cells in tumor growth." Int Rev Cell Mol Biol **275**: 89-131.

Robanus-Maandag, E. C., C. A. Bosch, et al. (2003). "Association of C-MYC amplification with progression from the in situ to the invasive stage in C-MYC-amplified breast carcinomas." J Pathol **201**(1): 75-82.

Rottmann, S. and B. Luscher (2006). "The Mad side of the Max network: antagonizing the function of Myc and more." Curr Top Microbiol Immunol **302**: 63-122.

Rubio-Viqueira, B. and M. Hidalgo (2009). "Direct in vivo xenograft tumor model for predicting chemotherapeutic drug response in cancer patients." Clin Pharmacol Ther **85**(2): 217-221.

Russo, J., H. J. Han, et al. (2008). "New advances in breast cancer metastasis." Womens Health (Lond) **4**(6): 547-549.

Sabo, A., T. R. Kress, et al. (2014). "Selective transcriptional regulation by Myc in cellular growth control and lymphomagenesis." Nature **511**(7510): 488-492.

Savino, M., D. Annibali, et al. (2011). "The action mechanism of the Myc inhibitor termed Omomyc may give clues on how to target Myc for cancer therapy." PLoS One **6**(7): e22284.

Schindelin, J., I. Arganda-Carreras, et al. (2012). "Fiji: an open-source platform for biological-image analysis." Nat Methods **9**(7): 676-682.

Schneider, C. A., W. S. Rasband, et al. (2012). "NIH Image to ImageJ: 25 years of image analysis." Nat Methods **9**(7): 671-675.

Schober, M., R. Jesenofsky, et al. (2014). "Desmoplasia and chemoresistance in pancreatic cancer." Cancers (Basel) **6**(4): 2137-2154.

Schonhuber, N., B. Seidler, et al. (2014). "A next-generation dual-recombinase system for time- and host-specific targeting of pancreatic cancer." Nat Med **20**(11): 1340-1347.

Schwab, M., K. Alitalo, et al. (1983). "Amplified DNA with limited homology to myc cellular oncogene is shared by human neuroblastoma cell lines and a neuroblastoma tumour." Nature **305**(5931): 245-248.

Sears, R. C. (2004). "The life cycle of C-myc: from synthesis to degradation." Cell Cycle **3**(9): 1133-1137.

Setoguchi, R., T. Kinashi, et al. (1998). "Defective degranulation and calcium mobilization of bone-marrow derived mast cells from Xid and Btk-deficient mice." Immunol Lett **64**(2-3): 109-118.

Shalaby, T. and M. A. Grotzer (2016). "MYC as Therapeutic Target for Embryonal Tumors: Potential and Challenges." Curr Cancer Drug Targets **16**(1): 2-21.

Shchors, K., E. Shchors, et al. (2006). "The Myc-dependent angiogenic switch in tumors is mediated by interleukin 1beta." Genes Dev **20**(18): 2527-2538.

Sheiness, D., L. Fanshier, et al. (1978). "Identification of nucleotide sequences which may encode the oncogenic capacity of avian retrovirus MC29." J Virol **28**(2): 600-610.

Singhi, A. D., A. Cimino-Mathews, et al. (2012). "MYC gene amplification is often acquired in lethal distant breast cancer metastases of unamplified primary tumors." Mod Pathol **25**(3): 378-387.

Smith, A. P., A. Verrecchia, et al. (2009). "A positive role for Myc in TGFbeta-induced Snail transcription and epithelial-to-mesenchymal transition." Oncogene **28**(3): 422-430.

Sodir, N. M., L. B. Swigart, et al. (2011). "Endogenous Myc maintains the tumor microenvironment." Genes Dev **25**(9): 907-916.

Soucek, L., J. J. Buggy, et al. (2011). "Modeling pharmacological inhibition of mast cell degranulation as a therapy for insulinoma." Neoplasia **13**(11): 1093-1100.

Soucek, L., M. Helmer-Citterich, et al. (1998). "Design and properties of a Myc derivative that efficiently homodimerizes." Oncogene **17**(19): 2463-2472.
Soucek, L., R. Jucker, et al. (2002). "Omomyc, a potential Myc dominant negative, enhances Myc-induced apoptosis." Cancer Res **62**(12): 3507-3510.
Soucek, L., E. R. Lawlor, et al. (2007). "Mast cells are required for angiogenesis and macroscopic expansion of Myc-induced pancreatic islet tumors." Nat Med **13**(10): 1211-1218.
Soucek, L., S. Nasi, et al. (2004). "Omomyc expression in skin prevents Myc-induced papillomatosis." Cell Death Differ **11**(9): 1038-1045.
Soucek, L., J. Whitfield, et al. (2008). "Modelling Myc inhibition as a cancer therapy." Nature **455**(7213): 679-683.
Soucek, L., J. R. Whitfield, et al. (2013). "Inhibition of Myc family proteins eradicates KRas-driven lung cancer in mice." Genes Dev **27**(5): 504-513.
Staller, P., K. Peukert, et al. (2001). "Repression of p15INK4b expression by Myc through association with Miz-1." Nat Cell Biol **3**(4): 392-399.
Stiff, A., P. Trikha, et al. (2016). "Myeloid-Derived Suppressor Cells Express Bruton's Tyrosine Kinase and Can Be Depleted in Tumor-Bearing Hosts by Ibrutinib Treatment." Cancer Res **76**(8): 2125-2136.
Strouch, M. J., E. C. Cheon, et al. (2010). "Crosstalk between mast cells and pancreatic cancer cells contributes to pancreatic tumor progression." Clin Cancer Res **16**(8): 2257-2265.
Talamillo, A., L. Grande, et al. (2017). "ODZ1 allows glioblastoma to sustain invasiveness through a Myc-dependent transcriptional upregulation of RhoA." Oncogene **36**(12): 1733-1744.
Tansey, W. P. (2014). "Mammalian MYC Proteins and Cancer." New Journal of Science **2014**: 27.
Tentler, J. J., A. C. Tan, et al. (2012). "Patient-derived tumour xenografts as models for oncology drug development." Nat Rev Clin Oncol **9**(6): 338-350.
Thompson, P. J., J. M. Hanson, et al. (1983). "Asthma, mast cells, and sodium cromoglycate." Lancet **2**(8354): 848-849.
Treon, S. P., C. K. Tripsas, et al. (2015). "Ibrutinib in previously treated Waldenstrom's macroglobulinemia." N Engl J Med **372**(15): 1430-1440.
Vargo-Gogola, T. and J. M. Rosen (2007). "Modelling breast cancer: one size does not fit all." Nat Rev Cancer **7**(9): 659-672.
Varnat, F., I. Siegl-Cachedenier, et al. (2010). "Loss of WNT-TCF addiction and enhancement of HH-GLI1 signalling define the metastatic transition of human colon carcinomas." EMBO Mol Med **2**(11): 440-457.
Vennstrom, B., D. Sheiness, et al. (1982). "Isolation and characterization of c-myc, a cellular homolog of the oncogene (v-myc) of avian myelocytomatosis virus strain 29." J Virol **42**(3): 773-779.
Vita, M. and M. Henriksson (2006). "The Myc oncoprotein as a therapeutic target for human cancer." Semin Cancer Biol **16**(4): 318-330.
von Eyss, B. and M. Eilers (2011). "Addicted to Myc--but why?" Genes Dev **25**(9): 895-897.
von Eyss, B., L. A. Jaenicke, et al. (2015). "A MYC-Driven Change in Mitochondrial Dynamics Limits YAP/TAZ Function in Mammary Epithelial Cells and Breast Cancer." Cancer Cell **28**(6): 743-757.
Von Hoff, D. D., T. Ervin, et al. (2013). "Increased survival in pancreatic cancer with nab-paclitaxel plus gemcitabine." N Engl J Med **369**(18): 1691-1703.
Walz, S., F. Lorenzin, et al. (2014). "Activation and repression by oncogenic MYC shape tumour-specific gene expression profiles." Nature **511**(7510): 483-487.
Wang, M. L., S. Rule, et al. (2013). "Targeting BTK with ibrutinib in relapsed or refractory mantle-cell lymphoma." N Engl J Med **369**(6): 507-516.
Weigelt, B. and J. S. Reis-Filho (2009). "Histological and molecular types of breast cancer: is there a unifying taxonomy?" Nat Rev Clin Oncol **6**(12): 718-730.

Welcker, M., A. Orian, et al. (2004). "The Fbw7 tumor suppressor regulates glycogen synthase kinase 3 phosphorylation-dependent c-Myc protein degradation." Proc Natl Acad Sci U S A **101**(24): 9085-9090.

Welsh, T. J., R. H. Green, et al. (2005). "Macrophage and mast-cell invasion of tumor cell islets confers a marked survival advantage in non-small-cell lung cancer." J Clin Oncol **23**(35): 8959-8967.

Whatcott, C. J., C. H. Diep, et al. (2015). "Desmoplasia in Primary Tumors and Metastatic Lesions of Pancreatic Cancer." Clin Cancer Res **21**(15): 3561-3568.

Whatcott, C. J., R. G. Posner, et al. (2012). Desmoplasia and chemoresistance in pancreatic cancer. Pancreatic Cancer and Tumor Microenvironment. P. J. Grippo and H. G. Munshi. Trivandrum (India).

Whitfield, J. R., M. E. Beaulieu, et al. (2017). "Strategies to Inhibit Myc and Their Clinical Applicability." Front Cell Dev Biol **5**: 10.

Whitfield, J. R. and L. Soucek (2012). "Tumor microenvironment: becoming sick of Myc." Cell Mol Life Sci **69**(6): 931-934.

Wlodarski, K., K. Morrison, et al. (1982). "Effects of nu gene on the numbers of mast cells in lymph nodes." Scand J Immunol **15**(1): 105-108.

Wolfer, A. and S. Ramaswamy (2011). "MYC and metastasis." Cancer Res **71**(6): 2034-2037.

Wolfer, A., B. S. Wittner, et al. (2010). "MYC regulation of a "poor-prognosis" metastatic cancer cell state." Proc Natl Acad Sci U S A **107**(8): 3698-3703.

Xiao, M., Z. Hong, et al. (2011). "TMTP1, a novel tumor-homing peptide, specifically targets hematological malignancies and their metastases." J Huazhong Univ Sci Technolog Med Sci **31**(5): 608-613.

Xu, J., Y. Chen, et al. (2010). "MYC and Breast Cancer." Genes Cancer **1**(6): 629-640.

Yang, S., J. J. Zhang, et al. (2012). "Mouse models for tumor metastasis." Methods Mol Biol **928**: 221-228.

Yang, W., D. Luo, et al. (2008). "TMTP1, a novel tumor-homing peptide specifically targeting metastasis." Clin Cancer Res **14**(17): 5494-5502.

Yeh, P. Y., Y. S. Lu, et al. (2011). "IkappaB kinases increase Myc protein stability and enhance progression of breast cancer cells." Mol Cancer **10**: 53.

Ziegenhagen, M. W., P. Zabel, et al. (1998). "Serum level of interleukin 8 is elevated in idiopathic pulmonary fibrosis and indicates disease activity." Am J Respir Crit Care Med **157**(3 Pt 1): 762-768.

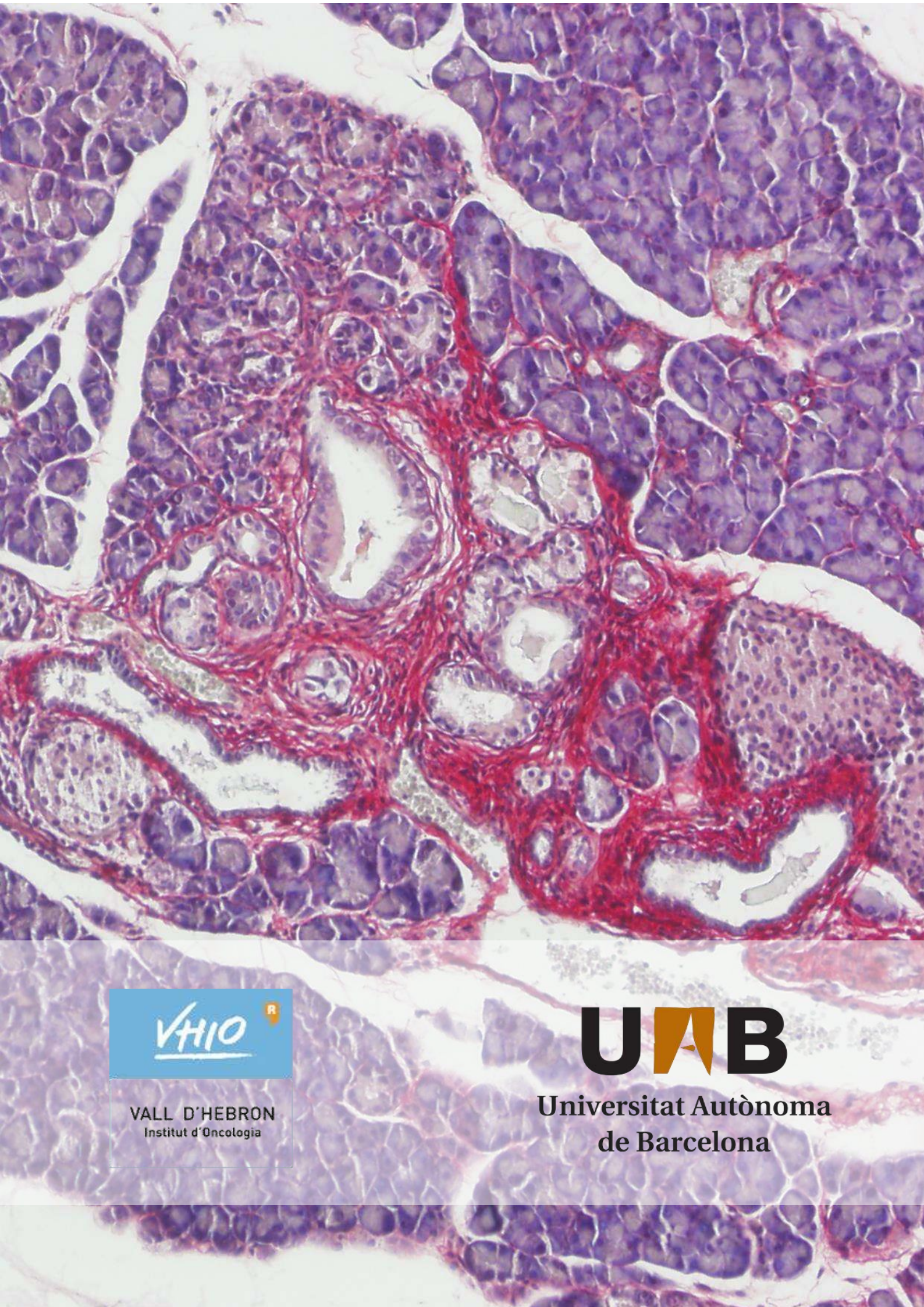

VHIO

VALL D'HEBRON
Institut d'Oncologia

UAB
Universitat Autònoma
de Barcelona